Contributions to fast and accurate antenna characterization

Nicolas Mézières

▶ **To cite this version:**

Nicolas Mézières. Contributions to fast and accurate antenna characterization. Electronics. Université Rennes 1, 2021. English. NNT : 2021REN1S039 . tel-03434344

HAL Id: tel-03434344
https://theses.hal.science/tel-03434344

Submitted on 18 Nov 2021

THESE DE DOCTORAT DE

L'UNIVERSITE DE RENNES 1

ECOLE DOCTORALE N° 601
*Mathématiques et Sciences et Technologies
de l'Information et de la Communication*
Spécialité : *Électronique*

Par

Nicolas MÉZIÈRES

Contributions to Fast and Accurate Antenna Characterization

**Soutenance à Rennes, le 25/08/2021
Unité de recherche : IETR UMR CNRS 6164**

Rapporteurs avant soutenance :

Geneviève Mazé-Merceur   Directrice de recherche, CEA CESTA, Le Barp, France
Olav Breinbjerg   Professeur, DTU, Lyngby, Danemark

Composition du Jury :

Examinateurs : Geneviève Mazé-Merceur   Directrice de recherche, CEA CESTA, Le Barp, France
                Olav Breinbjerg   Professeur, DTU, Lyngby, Danemark
                Thomas Eibert   Professeur, TUM, Munich, Allemagne
                Gwenn Le Fur   Ingénieur-chercheur, CNES, Toulouse, France
                Jean-Marie Lerat   Responsable département, LNE, Trappes, France
Dir. de thèse : Benjamin Fuchs   Chargé de recherche CNRS, IETR, Rennes, France

Invité(s)

                Laurent Le Coq   Ingénieur de recherche, IETR, Rennes, France (encadrant de thèse)
                Michael Mattes   Professeur associé, DTU, Lyngby, Danemark
                Alexandre Chabory   Professeur associé, ENAC, Toulouse, France
                Lars Jacob Foged   Directeur scientifique de MVG, Pomezia, Italie

Contents

Remerciements

To begin, a small word in english to thank all the people involved in the thesis, from the ones introducing me to the subject to the members of the committee for the examination. I am very happy and grateful for the opportunity I have been given and I will definitely keep a very good memory of these 3 years.

J'ai eu la chance de bénéficier, lors de cette période toujours marquante de la thèse, d'un encadrement extrêmement bienveillant, présent, pertinent et compétent. Je suis infiniment reconnaissant envers Benjamin pour tout cela et sa régularité dans ses qualités malgré les péripéties qu'il a pu connaître. Laurent, qui au-delà de ses conseils précieux en matière scientifique (et diplomatique), m'a impliqué et m'implique dans les perspectives de développement de l'IETR. Michael, pour sa gentilesse, ses remarques scientifiques avisées et son aide de grande qualité. Je remercie la confiance placée en moi par Gwenn et Romain, et de façon plus générale également le service antenne du CNES pour les visites ponctuelles à Toulouse. Jean-Marie pour sa contribution à la mise en place de cette thèse et à son bon déroulement. Je remercie les personnes du laboratoire IETR que j'ai eu la joie de rencontrer, pour les nombreuses discussions, expériences musicales, conseils et soutien moral passées et à venir : Noëlle, Franck, Maxime, Stéphane, Paul, Christophe, Xavier, Nathalie, Hervé ... Je salue également mes collègues doctorants ou aujourd'hui docteurs et leur souhaite le meilleur pour la suite : Seydouba, Nicolas, David, Gaëtan, Guillaume, Léonin, Gabriel, Ray, Rosa, Yann, ...

Merci à ma famille qui m'a toujours entouré avec un amour, et une patience, extrêmes. Mes parents, Jean-François et Marie-Laure et mon frère, Pierre ; à qui je dois ce que je suis. Mes oncles et tantes, Joël, Martine, Nadine, Serge ; pour leur présence rassurante et leur confiance inconditionnelle. Mes cousins pour tous les souvenirs ; Benjamin, Chloé, Julie, Samuel, Théo, et à la nouvelle généation qui arrive. Ma grand-mère, André. Mes autres grands-parents qui continuent de me donner du courage et de la motivation, où qu'ils soient, Louis, Roger et Odette. Laura, qui m'accompagne et me supporte au quotidien, me pousse toujours à aller de l'avant et m'a donné confiance en moi plus que quiconque. Je salue aussi sa famille qui m'a accueilli et avec qui je ne compte plus les bons moments, Cathie, Olivia, Lydie, Anna, Pierre, Louise, Elisa et Jean-Marie, que je n'oublierai pas.

Résumé de la thèse

Contexte et motivations

Les systèmes de communication et de transmission sans fil connaissent un essor important depuis de nombreuses années. Cette sollicitation croissante des systèmes antennaires émerge de la multiplication des applications qui leurs sont liées telles que les réseaux mobiles terrestres, internet par satellite ou la multiplication des objets connectés (*Internet of Things* - IoT) [1, 2]. Cette tendance générale conduit à des développements toujours plus nombreux, entraînant d'importants besoins en caractérisation des antennes. La mesure du rayonnement de ces structures est en effet une étape clé dans la conception et la validation des systèmes de communication sans fil.

En plus de cet essor, la tendance est à la conception d'antennes de taille (électrique) et de complexité toujours plus grandes, et ce afin de répondre aux contraintes exigeantes en termes de performances en rayonnement, de bandes de fréquences, de reconfigurabilité, ... Au-delà de l'augmentation de la demande en terme de caractérisation, ces structures sont également de plus en plus difficiles à mesurer, que ce soit en terme d'équipement ou de compétences. Ainsi, la caractérisation d'une antenne requiert souvent la mesure d'un ou plusieurs diagrammes de rayonnement en 3D (sur la sphère complète), et implique donc une mobilisation étendue dans le temps des équipements de mesure. La mesure 3D du rayonnement d'une antenne de taille maximale 10λ est environ de 10 heures dans les chambres anéchoïques de l'IETR[1].

Enfin, la caractérisation d'une antenne est souvent désirée dans un environnement qui soit le plus réaliste possible. Ainsi, l'antenne est typiquement montée sur l'appareil destiné à l'accueillir ou une maquette de celui-ci. La simulation numérique d'environnements réalistes complexes est une opération fortement coûteuse en terme de ressources de calcul, à laquelle s'ajoutent des difficultés liées à la modélisation et à la prise en compte des nombreux paramètres ayant un impact sur le rayonnement. La mesure est souvent le seul moyen de prévoir le comportement en condition de l'antenne de façon fiable et réaliste. L'implantation des antennes dans leur environnement pendant la caractérisation implique généralement des temps de mesure encore plus grands en raison de l'augmentation des dimensions. Des difficultés en terme de mécanique et de cinématique au sein des systèmes de mesure sont également fréquemment rencontrées.

L'objectif de ces travaux de thèse est de tirer le meilleur parti des installations de mesures, typiquement des chambres anéchoïques, afin d'accélérer la mesure tout en garantissant la précision des résultats sur les diagrammes de rayonnement obtenus.

Ces travaux se sont déroulés à l'Université de Rennes 1 au laboratoire IETR, en col-

---

[1]Institut d'Électronique et des Technologies du numéRique

laboration et avec le soutien financier du CNES[1] et du LNE [2]. Ces deux institutions sont impliquées, parmi leurs nombreuses autres activités, dans la caractérisation de structures rayonnantes et bénéficient donc directement des résultats de cette thèse. Une partie des travaux a également été réalisée en collaboration avec l'Université Technique du Danemark (DTU).

Parallèlement à cette thèse, une action Recherche et Technologie du CNES intitulée "Nouvelles stratégies d'échantillonnage du champ électromagnétique pour l'accélération du temps de mesure" d'une durée de 18 mois a été menée.

Objectifs et contributions

L'objectif de ce travail de thèse est de développer de nouvelles méthodes permettant une caractérisation plus rapide et/ou plus fiable de structures rayonnantes. Ainsi, plusieurs techniques ont été proposées afin d'optimiser l'exploitation des systèmes de mesure actuels. Ces méthodes contiennent des procédures de mesures liées à des traitement spécifiques afin d'améliorer la détermination des diagrammes de rayonnement.

Tout d'abord, la caractérisation du rayonnement 3D des antennes peut être accélérée de façon significative par la réduction du nombre d'échantillons de mesure. Deux approches ont été étudiées en ce sens.

La première approche est basée sur la décomposition en ondes sphériques du champ rayonné par l'antenne sous test. Elle nécessite uniquement la connaissance de la dimension électrique maximale de l'antenne. Une procédure de traitement automatique des données, contenant notamment une stratégie d'échantillonnage rapide, combinée à l'exploitation de la parcimonie de la décomposition en ondes sphériques a été proposée. L'accélération de la mesure liée à cette nouvelle technique a été démontrée et quantifiée expérimentalement en considérant des structures rayonnantes variées, que ce soit par leur type ou leur bande de fréquences.

La deuxième approche repose sur la construction d'un modèle d'ordre réduit adapté au problème de la caractérisation d'antennes. Les dimensions externes de l'antenne sous test et la connaissance de la surface de mesure permettent de construire une matrice de rayonnement liant les courants équivalents autour de l'antenne au champ rayonné. La méthode proposée est générale et peut être appliquée à n'importe quelle structure rayonnante et géométrie de la surface de mesure (sphérique, planaire, ...) en champ proche et lointain. Ce modèle de caractérisation d'antenne fournit non-seulement le nombre d'échantillons minimal requis mais permet également d'interpoler le champ rayonné par l'antenne sous test avec une précision contrôlée, choisie selon la dynamique de la mesure. Cette approche peut être interprétée comme une généralisation numérique des études analytiques menées sur le nombre de degrés de liberté du champ rayonné par une antenne donnée.

De plus, des procédures de post-traitement des données de mesure ont été développées afin d'optimiser le positionnement de l'antenne au sein du système de mesure, permettant ainsi d'améliorer la précision de la reconstruction du diagramme de rayonnement mesuré sans aucun coût supplémentaire. Ainsi, l'orientation et la position de l'antenne sous test sont optimisées afin de compresser la décomposition en ondes sphériques du champ rayonné, ce qui facilite sa reconstruction à partir d'un jeu de mesure donné. Ces techniques sont

---

[1]Centre National d'Études Spatiales
[2]Laboratoire National de métrologie et d'Essais

particulièrement adaptées aux cas de mesures d'antennes en environnement ou d'antennes de diagrammes de rayonnement reconfigurables.

En résumé, nous pensons que les principales contributions de ce travail de thèse sont :

1. La conception, l'implémentation et la validation de plusieurs méthodes de modélisation électromagnétique (décomposition en ondes sphériques, méthode des moments par intégration surfacique), d'outils mathématiques (translation et rotation des ondes sphériques), de codes basés sur des méthodes aux éléments finis (création de maillage, outils de visualisation) et de procédures d'optimisation (reconstruction parcimonieuse, processus Gaussiens, descente de gradient).

2. La validation expérimentale systématique de toutes les méthodes proposées sur des structures rayonnantes variées, opérant dans des bandes de fréquences diverses et caractérisées dans différents systèmes de mesure, incluant les chambres anéchoïques de l'IETR et un système de mesure commercial de chez MVG [3].

Afin d'illustrer les contributions de ce travail en terme de caractérisation rapide d'antenne, la figure suivante montre des estimations du temps d'acquisition du champ électrique dans les chambres anéchoïques de l'IETR en fonction de la dimension maximale de l'antenne. Le temps requis par la technique de mesure standard par ondes sphériques, dénotée *Standard* est comparé à celui des deux approches proposées : la décomposition parcimonieuse en ondes sphériques *Sparse SWE* pour *Spherical Wave Expansion* et la méthode utilisant un modèle d'ordre réduit, ici en entourant l'antenne par un cube, technique appelée ROM pour *Reduced-Order Model*.
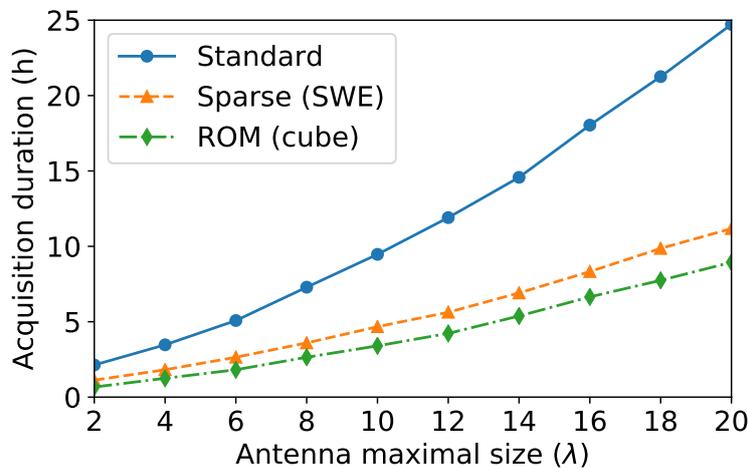

FIGURE 1 : Durée estimée du temps d'acquisition du champ rayonné dans les bases de mesure de l'IETR en utilisant la procédure de mesure standard et les 2 méthodes de mesure rapide proposées lors de cette thèse.

Contenu du mémoire

Ce mémoire de thèse comprend 4 chapitres dont les contenus sont résumés ici.

Chapitre 1

Le Chapitre 1 présente un tour d'horizon des techniques liées à la caractérisation des champs rayonnés par les antennes. Les quantités d'intérêts concernant la mesure des caractéristiques de rayonnement des antennes sont définies, du champ rayonné lui-même aux valeurs dites intégrées telles que la directivité, ou la polarisation [4,5]. Les configurations classiques de mesure d'antennes sont décrites. Elles sont habituellement séparées en deux grandes catégories, les techniques dites champ proche et champ lointain, déterminées par la distance électrique entre l'antenne mesurée et la sonde de mesure. Les dispositifs de mesure disponibles à l'IETR, qui ont permis de valider les procédures développées sur des données expérimentales, sont également détaillés [3,6,7].

Les diagrammes de rayonnement, résultats de la caractérisation d'une antenne, sont des fonctions continues (habituellement sur la sphère en champ lointain) qui représentent les caractéristiques de l'antenne en tant qu'élément rayonnant. La comparaison de ces diagrammes est donc un élément crucial dans la conception et la validation des techniques de mesure. Ainsi, des métriques de comparaison, notamment utilisées dans le cadre de campagne de comparaison de bases de mesure européennes [8] ou de techniques de mesure rapide [9,10], sont données et appliquées sur des exemples afin d'en montrer les propriétés respectives.

De façon générale, la précision des techniques de mesure est fortement liée au nombre d'échantillons du champ à disposition. Chaque configuration et/ou technique de post-traitement des données donne lieu à son propre nombre d'échantillons. Un compromis est néanmoins inévitable entre la précision de la mesure et le temps d'acquisition du champ. Ce dernier augmente avec le nombre d'échantillons de mesure, une estimation de ces temps en lien avec les techniques étudiées à l'IETR est alors donnée, ce qui permet de conclure de façon quantitative sur le gain effectif en temps d'acquisition du champ rayonné.

Chapitre 2

Le Chapitre 2 concerne la première méthode de caractérisation rapide d'antennes étudiée au cours de ce travail. Elle est basée sur la décomposition parcimonieuse du champ rayonné en ondes sphériques (*Spherical Waves*, SW [11]), aussi appelées harmoniques sphériques. La caractérisation du champ rayonné repose de façon générale sur la décomposition du signal mesuré dans une base de fonctions. La mesure du champ rayonné est une discrétisation du diagramme de rayonnement, la caractérisation 3D en est l'interpolation de ce champ sur la sphère. Les ondes sphériques sont en particulier une base des fonctions sur la sphère [12] tout en étant solution des équations de Maxwell. Ces deux propriétés, mathématique et physique, permettent de décomposer le champ rayonné par les antennes [11], tout en garantissant leur pertinence dans ce contexte. Après un rappel de l'origine et de la définition de ces fonctions, la décomposition du champ est considérée.

La méthode usuelle de caractérisation du champ rayonné par une antenne sur une sphère [11] peut être vue comme sur une généralisation de la notion de fréquence de Nyquist [13] au cas de la décomposition sur la sphère. Cette technique garantit une identification exacte des coefficients sous l'hypothèse que le champ rayonné possède une bande passante

limitée en termes de variations spatiales (de la même façon que le contenu fréquentiel d'un signal temporel sera exactement identifié si l'échantillonnage est suffisamment fin). Si l'importance et la précision de cette technique ne sont plus à démontrer [14,15], cela se fait au prix d'un grand nombre d'échantillons de mesure, et donc de temps d'acquisition du champ importants voire rédibhitoires dans certains cas.

Néanmoins, la décomposition du champ dans la base des ondes sphériques possède une propriété remarquable ; beaucoup de coefficients de pondération de ces ondes sphériques sont d'amplitudes négligeables. Cette particularité permet de reformuler la caractérisation d'antennes en un problème convexes de reconstruction parcimonieuse [16,17] et d'en utiliser les outils [18–20].

Ainsi, la détermination automatique du paramètre contrôlant l'attache aux données de mesures, un point crucial et récurrent pour la résolution de problèmes inverses avec régularisation, est discutée. Une approche, inspirée d'études menées pour des applications différentes [21,22] a été étendue avec succès à notre problèmes de caractérisation d'antennes.

Par ailleurs, le nombre minimal de points de mesure à utiliser pour cette technique de caractérisation rapide d'antennes avec une précision donnée, n'est pas connu à l'avance. Néanmoins, à l'aide d'hypothèses réalistes sur les spectres générés par la mesure antenne, un facteur de sous-échantillonnage global peut être obtenu grâce à l'utilisation de la théorie de la reconstruction parcimonieuse, et plus particulièrement les diagrammes de transition de phase [23]. Ces diagrammes ont été introduits à des fins théoriques radicalement différentes. Ils peuvent être étendus à la mesure d'antennes, comme notamment dans [24, 25]. Nos contributions sont validées sur des données expérimentales et une estimation des gains sur le temps des mesures d'antennes réalisée à l'IETR est donné en fonction de la dimension électrique maximale de l'antenne.

Chapitre 3

Le Chapitre 3 traite de l'amélioration de la reconstruction du diagramme de rayonnement par optimisation du positionnement de l'antenne en post-traitement en utilisant la décomposition en ondes sphériques. Nous avons montré dans le chapitre 2 que la précision des résultats est liée au nombre de points de mesure, que l'on utilise la technique standard basée sur un taux d'échantillonnage de Nyquist ou les techniques de mesure rapide. Néanmoins nous pouvons également favoriser l'extraction de l'information contenue dans un jeu de donnée de façon plus pertinente en utilisant les propriétés des ondes sphériques et de la reconstruction parcimonieuse, cette dernière étant très sensible aux variations et au nombre de coefficients significatifs impliqués dans la décomposition du champ.

En effet, le spectre en ondes sphériques d'une antenne, c'est à dire l'ensemble des coefficients de pondération, est une représentation du champ relativement à un système de coordonnées défini. Une modification de position ou d'orientation de ce système modifie ce spectre [26–28] et peut donc être mis à profit pour favoriser l'identification correcte des coefficients. Ce système de coordonnées peut-être modifié une fois la mesure du champ effectuée par les formules analytiques de translation et de rotation des ondes sphériques. L'exploitation de ces formules et des effets de ces transformations sur le spectre des coefficients permet d'obtenir une représentation encore plus compacte du rayonnement de l'antenne. La compacité de ce spectre est en relation directe avec l'identification précise des coefficients à partir d'un nombre restreint de données de mesure [23,25]. Une optimisation du positionnement de l'antenne (origine et orientation du système de coordonnées) a été

proposée afin d'améliorer la reconstruction du diagramme de rayonnement d'une antenne à partir du champ mesuré. Cette approche ne nécessite pas de mesures supplémentaires. Ses avantages sur la précision de la mesure rapide sont démontrés avec de nombreux exemples numériques et expérimentaux en champ proche sphérique et lointain.

Chapitre 4

Le Chapitre 4 s'intéresse à la construction d'un modèle d'ordre réduit pour la caractérisation d'antennes [29]. Ces travaux ont été réalisés en collaboration avec le Prof. M. Mattes de l'université technique du Danemark (DTU).

Le principe de surface équivalente ou de Huygens permet la représentation d'un ensemble de sources par des courants équivalents sur une surface qui les entoure [30]. Une formulation dite aux éléments finis de frontière peut alors être utilisée afin d'approcher ces courants équivalents par une pondération de fonction de bases connue de ces courants. Cela permet la construction d'une matrice de rayonnement. Cette approche a été proposée pour réaliser du diagnostic d'antennes dans [31–34].

La décomposition en valeurs singulières de cette matrice de rayonnement permet la construction d'une base des champs rayonnés par l'antenne. Cette base, construite numériquement, est parfaitement adaptée à notre problème de caractérisation d'antennes puisqu'elle prend en compte la géométrie de l'antenne ainsi que la surface de mesure. Elle est tronquée de façon appropriée afin de générer une représentation compacte des champs rayonnés par une antenne contenue dans la surface équivalente. Nous avons montré que le nombre minimal d'échantillons requis pour caractériser une antenne pour une précision donnée est lié à l'aire de cette surface équivalente. Ce résultat, obtenu numériquement et validé expérimentalement, généralise les travaux analytiques menées sur le nombre de degrés de liberté des champs rayonnés [35].

Conclusion

Cette thèse a contribué au développement de méthodes de mesure pour améliorer la caractérisation d'antennes et donc l'utilisation des bases de mesure. La réalisation de ces travaux a donné lieu à la conception et à la validation de plusieurs codes et méthodes en plus de l'utilisation de routines existantes. Ces développements contiennent notamment la décomposition en ondes sphériques et la méthode des moments par éléments finis aux frontières. Tous ces outils ont tous été validés par des études sur des données de simulation et de mesures réalisées à l'IETR.

Suite à ce travail, plusieurs pistes sont envisageables. Il serait ainsi intéressant de valider expérimentalement les techniques de mesure rapide d'antennes au champ proche. Par ailleurs, il semble prometteur d'adapter les approches de mesures rapides d'antennes aux mesures sans phase. En outre, l'interpolation, en plus de la dimension spatiale, de l'axe électrique / fréquentiel des mesures de champ électromagnétique est une piste qu'il convient de creuser. Enfin, les techniques de positionnement de l'antenne pourraient certainement être adaptées afin d'estimer leur centre de phase.

Bibliographie

[1] P. Jonsson et al. Ericsson mobility report. Technical report, Ericsson, 2020. Available at https://www.ericsson.com/4adc87/assets/local/mobility-report/documents/2020/november-2020-ericsson-mobility-report.pdf.

[2] Cisco annual internet report. Technical report, CISCO, 2020. Available at https://www.cisco.com/c/en/us/solutions/collateral/executive-perspectives/annual-internet-report/white-paper-c11-741490.pdf.

[3] Starlab 650MHz-18GHz. Technical report, MVG, 2020. Available at https://www.mvg-world.com/fr/products/antenna-measurement/multi-probe-systems/starlab.

[4] J. Mccormick, C. Parini, S. Gregson, and D. Janse Van Rensburg. *The Theory and Practice of Modern Antenna Test Range Measurements*. Jan 2014.

[5] IEEE standard for definitions of terms for antennas. *IEEE Std 145-2013 (Revision of IEEE Std 145-1993)*, pages 1–50, 2014.

[6] Plateforme M2ARS. Technical report, IETR-UR1, 2020. Available at https://www.ietr.fr/plateforme-m2ars-manufacturing-measurement-analysis-radiating-systems.

[7] Bases de mesure champ proche. Technical report, IETR-INSA, 2020. Available at https://www.ietr.fr/bases-de-mesure-champ-proche.

[8] A. Alexandridis, C. Sabatier, H. Eriksson, J. Zackrisson, L. Jacob Foged, L. Durand, M. Sierra Castener, M. Boettcher, S. Burgos, and S. Pivnenko. Recommendations and comparative investigations for near-field antenna measurement techniques and procedures. Technical Report Deliverable A1.2D2, Antenna Centre of Excellence, dec 2007.

[9] M. Salucci, M. D. Migliore, G. Oliveri, and A. Massa. Antenna measurements-by-design for antenna qualification. *IEEE Trans. on Antennas and Propag.*, 66(11) :6300–6312, Nov 2018.

[10] G. Giordanengo, M. Righero, F. Vipiana, M. Sabbadini, and G. Vecchi. Fast antenna testing with reduced near field sampling. *IEEE Trans. on Antennas and Propag.*, 62(5) :2501–2513, May 2014.

[11] J. Hald, J.E. Hansen, F. Jensen, and F.H. Larsen. *Spherical Near Field Antenna Measurements*. Peter Peregrinus, 1988.

[12] E.L. Hill. The Theory of Vector Spherical Harmonics. *American Journal of Physics*, 22 :211–214, April 1954.

[13] C. E. Shannon. Communication in the presence of noise. *Proceedings of the IRE*, 37(1) :10–21, 1949.

[14] IEEE recommended practice for near-field antenna measurements. *IEEE Std 1720-2012*, pages 1–102, 2012.

[15] O. Breinbjerg. Spherical near-field antenna measurements — the most accurate antenna measurement technique. In *2016 IEEE International Symposium on Antennas and Propagation (APSURSI)*, pages 1019–1020, June 2016.

[16] S. Foucart and H. Rauhut. *A Mathematical Introduction to Compressive Sensing.* Birkhauser, 2013.

[17] M. Elad. *Sparse and Redundant Representations - From Theory to Applications in Signal and Image Processing.* Springer, 2010.

[18] T. Blumensath and M. E. Davies. Iterative hard thresholding for compressed sensing. *CoRR*, abs/0805.0510, 2008.

[19] S. G. Mallat and Z. Zhang. Matching pursuits with time-frequency dictionaries. *IEEE Transactions on Signal Processing*, 41(12) :3397–3415, Dec 1993.

[20] G. Davis, S. Mallat, and Z. Zhang. *Adaptive Time-Frequency Approximations with Matching Pursuits*, volume 5. Elsevier B.V., 1994.

[21] P. C. Hansen. The L-curve and its use in the numerical treatment of inverse problems. In *Computational Inverse Problems in Electrocardiology*. WIT Press, 2000.

[22] A. Cultrera and L. Callegaro. A simple algorithm to find the l-curve corner in the regularization of inverse problems. *CoRR*, abs/1608.04571, 2016.

[23] D. L. Donoho and J. Tanner. Precise undersampling theorems. *Proceedings of the IEEE*, 98(6) :913–924, June 2010.

[24] B. Fuchs, L. Le Coq, S. Rondineau, and M.D. Migliore. Fast antenna far field characterization via sparse spherical harmonic expansion. *IEEE Trans. Antennas Propag.*, 65(10) :5503–5510, Oct. 2017.

[25] B. Hofmann, O. Neitz, and T. Eibert. On the minimum number of samples for sparse recovery in spherical antenna near-field measurements. *IEEE Trans. on Antennas and Propag.*, 67(12) :7597–7610, 2019.

[26] F. Jensen and A. Frandsen. On the number of modes in spherical wave expansions. In *AMTA 2004*, 10.

[27] D. Loschenbrand and C. Mecklenbrauker. Fast antenna characterization via a sparse spherical multipole expansion. Aachen, 2016. 4th International Workshop on Compressed Sensing Theory and its Applications to Radar, Sonar and Remote.

[28] R. Cornelius, D. Heberling, N. Koep, A. Behboodi, and R. Mathar. Compressed sensing applied to spherical near-field to far-field transformation. pages 1–4, Davos, 2016. Eur. Conf. Antennas Propag. (EuCAP).

[29] B. Fuchs and A.G. Polimeridis. Reduced-order models for fast antenna characterization. *IEEE Trans. Antennas Propag.*, 67(8) :5673–5677, Aug. 2019.

[30] Roger F. Harrington. *Time-Harmonic Electromagnetic Fields.* IEEE-Press, 2001.

[31] Y. Alvarez, F. Las-Heras, B. A. Dominguez-Casas, and C. Garcia. Antenna diagnostics using arbitrary-geometry field acquisition domains. *IEEE Antennas and Wireless Propagation Letters*, 8 :375–378, 2009.

[32] J. L. Araque Quijano and G. Vecchi. Improved-accuracy source reconstruction on arbitrary 3-d surfaces. *IEEE Antennas and Wireless Propagation Letters*, 8 :1046– 1049, 2009.

[33] L. J. Foged, F. Mioc, M. Sabbadini, J. L. A. Quijano, and G. Vecchi. Advanced antenna diagnostics based on equivalent currents. In *Proceedings of the Fourth European Conference on Antennas and Propagation*, pages 1–4, 2010.

[34] J. L. Araque Quijano and G. Vecchi. Field and source equivalence in source reconstruction on 3d surfaces. *Progress In Electromagnetics Research*, 103 :67 − 100, 2010.

[35] O. M. Bucci, C. Gennarelli, and C. Savarese. Representation of electromagnetic fields over arbitrary surfaces by a finite and nonredundant number of samples. *IEEE Trans. Antennas Propag.*, 46(3) :351–359, March 1998.

Introduction

Framework and motivations

There is a massive growth in the development of wireless devices that is driven by the constant increase of mobile data communications and the arising of new applications, such as Internet of Things, smart cities and Car2X communications to name just a few [1,2]. The performance of these wireless devices is obviously tightly linked to their transmitting and receiving component: the antenna. There is therefore a growing demand in testing ubiquitous antennas to make sure that the radiating performances of the wireless devices comply to the expected specifications. Antenna characterization is indeed an unavoidable step to validate the development and production of any wireless system.

In addition, the current trend is to design radiating structures of larger electrical dimension, with increased complexity in terms of specifications or environment. This is in answer to always more demanding needs in terms of performances, frequency band and functionalities (reconfigurability, multiple beam patterns, various operating modes). Consequently, the characterization of antennas has become more and more cumbersome and costly. The measurement of one or several 3D (full sphere) radiation patterns is often required to properly characterize the antenna under test, often leading to time consuming procedures. As a representative example, the 3D radiation pattern measurement of an antenna of maximum dimension equal to 10 wavelengths takes about 10 hours in the anechoic chamber of IETR[1] at the time of this manuscript.

Besides, the characterization of antennas in a realistic environment, typically embedded in a structure, is nowadays a frequently encountered requirement. It is indeed computationally costly to simulate numerically an accurate model of such embedded antennas so as to predict their radiation pattern as faithfully as possible. The measurement is often the only resort to get realistic and reliable predictions of the radiation characteristics of such systems. The large electrical dimensions of these structures render their characterization time consuming and impose some mechanical constraints on their positioning in the measurement facilities. Both specifications deserve to be properly addressed.

In this context, the main goal of this work is to improve the characterization of antennas by using and exploiting more efficiently measurement facilities, typically anechoic chambers. More specifically, contributions, including measurement procedures and processing, are proposed to speed up and/or improve the accuracy of the measurement of antenna radiation patterns.

This PhD thesis has been carried out at the UR1[2] in the IETR laboratory in collabor-

---

[1] *Institut d'Électronique et des Technologies du numéRique*
[2] *Université de Rennes 1*

INTRODUCTION

ation and with the financial support of the CNES[1] and the LNE[2]. Among their numerous activities, these two institutions are involved in the characterization of radiating structures and can therefore directly benefit from the results of this thesis. Besides, the last part of this thesis (use of reduced order model for a fast antenna characterization) has been done in collaboration with Prof. M. Mattes from the DTU[3] in Denmark.

In parallel to the present work, a *Recherche and Technologie* CNES action entitled *Nouvelles stratégies d'échantillonnage du champ électromagnétique pour l'accélération du temps de mesure* (New electromagnetic field sampling strategies for antenna measurement acceleration) of 18 months duration has been carried out.

Objectives and contributions

The goal of the PhD thesis is to develop methods that enable a faster and/or more accurate characterization of radiating structures. Thus, several techniques are proposed to improve the use of existing antenna measurement systems. They encompass measurement procedures associated to a specific processing of the produced data in order to increase the efficiency of antenna radiation pattern measurements.

The measurement of the radiation pattern of an antenna can be divided into four main phases: logistics, calibrations, the field acquisition and the post-processing of the measurement data to produce the final results and evaluate the quantities of interest. First, the measurement system must be chosen according to the antenna size and operating frequency. The weight and outer dimensions of the whole radiating structure are also constraints to be taken into account. A proper interface between the radiating structure and the positioning system has to be designed, takin into account the cinematic constraints. The probe has to be appropriately chosen, specific protections to minimize interaction between the AUT and the measurement system like absorbers are set and numerous other practical aspects must be considered. Then, a careful calibration of the system has to be performed, which contains non-exhaustively [3]: channel-balance, amplitude and phase drifts corrections, alignment procedures, sanity checks. This calibration step often implies some feedback loop to the logistic step. These two steps are driven by well-defined procedures, following measurement standards. While their impact over the total measurement time is very significant, these procedures cannot easily be shortened as it would inevitably impact the accuracy of the measurement. The next phase is the acquisition of the near or far field radiated by the AUT. The probe measures the radiated field according to a pre-defined sampling. This acquisition phase duration is also significant, as illustrated in Fig. 2. It can be reduced by decreasing the number of field samples. Because of its practical relevance, many efforts have been led in this direction. In this thesis, we propose two approaches to speed up the antenna characterization by reducing the number of radiated field samples.

The first one is based on the spherical wave expansion of the field radiated by the antenna under test and only calls for the knowledge of its maximum electrical dimension. By harnessing the sparse expansion of the radiated field, an automatic procedure including an efficient field sampling strategy has been proposed. This approach has been shown experimentally to lead to faster pattern characterizations for a wide range of radiating structures operating in diverse frequency bands.

---

[1] *Centre National d'Études Spatiales*
[2] *Laboratoire National de métrologie et d'Essais*
[3] Technical University of Denmark
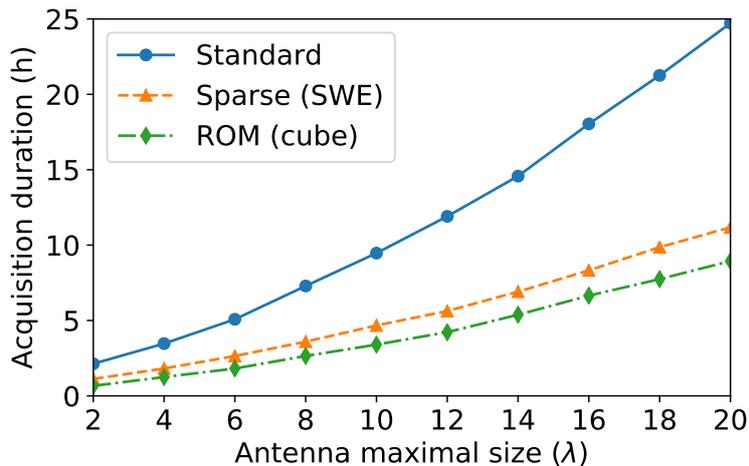
Figure 2: Estimated field acquisition durations at IETR using the standard approach and the proposed fast antenna characterization procedures.

In addition, several post-processing strategies based have been developed to optimize the positioning of the antenna under test within the measurement system. By doing so, it is possible to improve the quality of the radiation pattern measurement without any additional cost. Thus, both the rotation and the translation of the antenna can be optimized so as to further compress the antenna pattern representation and consequently ease its interpolation from a given field dataset. This approach finds a great relevance in many frequently encountered scenarios including the case where antennas are mounted on structures that also contributes to the radiation pattern.

The second approach, to speed up antenna measurements, relies on the construction of a reduced order model for the antenna characterization problem. It exploits the outer dimensions of the antenna under test and the geometry of the measurement surface so as to build the radiation matrix that maps the equivalent currents representing the antenna to the radiated field. The proposed methodology is general, it can be applied to any radiating structures and field measurement scans in either near or far field. This reduced antenna characterization model provides not only the minimum number of field samples to properly characterize antennas, but also the way to interpolate the field radiated by the antenna under test with a controlled accuracy. This approach can be seen as a numerical generalization of the analytical works on the number of degrees of freedom of the fields radiated by antennas [4].

In summary, we believe that the main contributions of this work are:

1. The development, implementation and validation of several electromagnetic modelling methods (spherical wave expansion of the field, surface integral equation method of moment), mathematical tools (translation and rotation of the spherical waves), finite element tools (meshing, current visualizations) and optimization solvers (sparse recovery methods, Gaussian processes, gradient descent) for a better antenna characterization.

2. The systematic experimental validations of all proposed procedures on various radiating structures operating in different frequency bands and characterized in different

measurement facilities including several laboratory anechoic chambers and a commercial measurement system.

To illustrate our contribution in terms of fast antenna characterization, the following figure plots an estimation of the field acquisition duration in our anechoic chambers as a function of the antenna maximal dimension. It compares the standard approach (often called Nyquist) using Spherical Wave Expansion (SWE) to our two proposed methods: the sparse SWE and the Reduced Order Model (ROM) using a cube.

Content of the manuscript

This PhD work is organized in four chapters.

The Chapter I gives an overview on antenna measurement techniques and tools related to radiation pattern characterization. The quantities of interest for the present work and the measurement configurations are presented. The antenna measurement facilities of our laboratories, used to validate our work, are described. Various metrics to assess the quality of the antenna pattern measurement are proposed and discussed and the way to estimate the antenna field acquisition duration, a key point of our work, is also provided.

The Chapter II addresses our first fast antenna characterization approach based on the sparse spherical wave expansion. The definition of the SW is first recalled and their exploitation in a context of a coarse antenna pattern sampling is then detailed. The proposed procedure enables to properly characterize antenna patterns from a number of field samples smaller than standard approaches, as shown in Fig. 2. The corresponding gain in field acquisition durations are estimated.

The Chapter III deals with the improvement of the antenna pattern reconstruction by optimizing the antenna position and orientation *a posteriori* from the measurement of its radiation pattern. To this end, the analytical formulas for translation and rotation of the spherical waves are given and the effects over the spherical coefficients are shown and discussed. The positioning of the antenna under test can be optimized in order to make the SW spectrum more compact and therefore easier to retrieve. This approach enables the reconstruction of the antenna radiation pattern from a given measurement dataset with a better accuracy, as validated using numerous numerical and experimental dataset.

The Chapter IV proposes our second fast antenna characterization approach that relies on the construction of a reduced order model of the antenna characterization problem. Using the Huygens' equivalent principle, the radiation matrix that links the electromagnetic sources to the radiated field is built. The truncated singular value decomposition of this matrix provides a compressed representation of the antenna characterization problem. The minimum number of field samples to characterize an antenna with a controlled accuracy is derived and checked both numerically and experimentally. This number is linked to the area of the equivalent surface as confirmed for various antenna shapes. This result is in agreement and extends existing analytical works.

Finally, the conclusions of this work are drawn and ideas for future investigations are given.

Bibliography

[1] P. Jonsson et al. Ericsson mobility report. Technical report, Ericsson, 2020. Available at https://www.ericsson.com/4adc87/assets/local/mobility-report/documents/2020/november-2020-ericsson-mobility-report.pdf.

[2] Cisco annual internet report. Technical report, CISCO, 2020. Available at https://www.cisco.com/c/en/us/solutions/collateral/executive-perspectives/annual-internet-report/white-paper-c11-741490.pdf.

[3] J. Mccormick, C. Parini, S. Gregson, and D. Janse Van Rensburg. *The Theory and Practice of Modern Antenna Test Range Measurements*. Jan 2014.

[4] O. M. Bucci, C. Gennarelli, and C. Savarese. Representation of electromagnetic fields over arbitrary surfaces by a finite and nonredundant number of samples. *IEEE Trans. Antennas Propag.*, 46(3):351–359, March 1998.

Chapter I

Antenna radiation pattern characterization

I.1 Introduction

The measurement of antennas is a necessary step to determine their electrical properties and more specifically their radiation characteristics. The full wave electromagnetic software combined to the increasing computational power are efficient and accurate tools to predict faithfully the radiation characteristics. However, measurements remain inevitable to provide the ground truth of the manufactured antenna.

The behaviour of antennas are described by various parameters. In this work, we focus on the radiation performances of antennas and the relevant parameters to be characterized to this end are detailed. The radiation parameters of antennas are usually measured in a controlled (interference free) environment so as to be able to characterize only the Antenna Under Test (AUT) or Device Under Test (DUT) itself. In the sequel, we will refer to DUT when the antenna is not alone but mounted on a structure for instance. Among antenna measurement facilities, we can distinguish outdoor and indoors ranges, such as anechoic chambers, which are designed to isolate the tested device as much as possible from unwanted electromagnetic radiations. There are various types and sizes of anechoic chambers, they are topically covered with absorbing elements, as the one shown in Fig. I.1.

There are various measurement techniques to characterize the radiation pattern of antennas. These techniques can be discriminated by the electrical distance between the AUT and the measurement probe (near or far field) and the geometry of the field measurement scan (typically planar, cylindrical or spherical). These various measurement ranges and their characteristics are reviewed. The systems available in our laboratory and used to validate our antenna characterization procedures are described.

The variety of antenna measurement techniques and the use of dedicated processing call for the assessment of the characterization results. To this end, several complementary metrics are proposed in order to compare two antenna radiation patterns. These metrics are essential to assess the quality of the proposed antenna characterization strategies.

The accuracy of AUT measurements highly depends on the measurement sampling. Any antenna pattern measurement, no matter the configuration (near and far field, geometry of the measurement scan), requires to fulfil a sampling criterion to ensure a proper characterization. The standard field sampling criterion is recalled. One of the goal of this
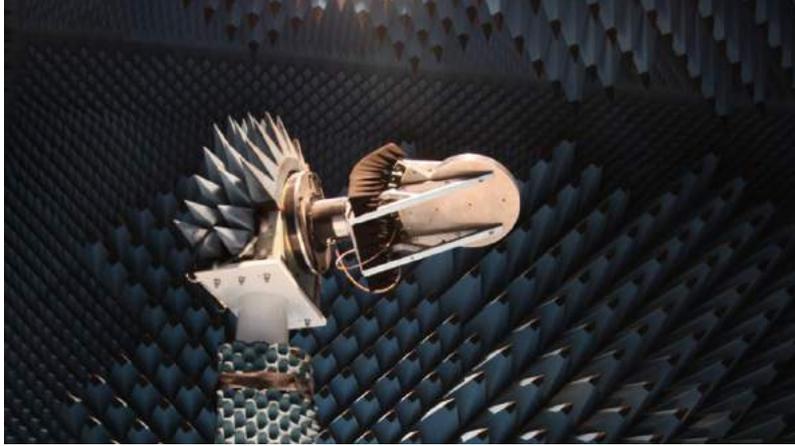
Figure I.1: A Luneburg lens antenna on the positioning system of the CACENDRA, anechoic chamber of IETR-UR1 for centimetric wavelength antennas.

work is precisely to go beyond this standard sampling. To achieve this so-called undersampling, we leverage *a priori* information about the field radiated by antennas or about the AUT geometry.

Indeed, the field sampling directly impacts the duration of the field acquisition and therefore the whole antenna pattern measurement. A procedure to estimate the duration of this field acquisition phase in our anechoic chamber is provided. Such an estimation is important in order to assess the two fast antenna characterization approaches proposed in this thesis.

I.2 Measurement techniques

I.2.a Antenna parameters

The antenna parameters commonly refer to the electrical properties of the radiating system. We provide a non-comprehensive list of these parameters, with a focus on the radiation properties. The quoted definitions comes from the IEEE standard definition document of terms for antennas [1].

Radiation pattern

The radiation pattern is "the spatial distribution of a quantity that characterizes the electromagnetic field generated by an antenna". In spherical coordinates (θ, φ), illustrated in Fig. I.2, it is an angular function of an antenna radiation parameter as it is always considered at a given distance. If not specified otherwise, the radiation pattern usually refers to the electric field magnitude.

Field pattern

The electric or magnetic field pattern is a type of radiation pattern where the quantity of interest is the electric field $\mathbf{E}$ itself (or magnetic one $\mathbf{H}$), seen as a function over the region of interest, e.g. $\mathbf{E}(r, \theta, \varphi)$ in spherical coordinates. Strictly speaking, an electromagnetic field is time dependent, i.e. $\mathbf{E}(t, r, \theta, \varphi)$. However this time dependency can be assumed
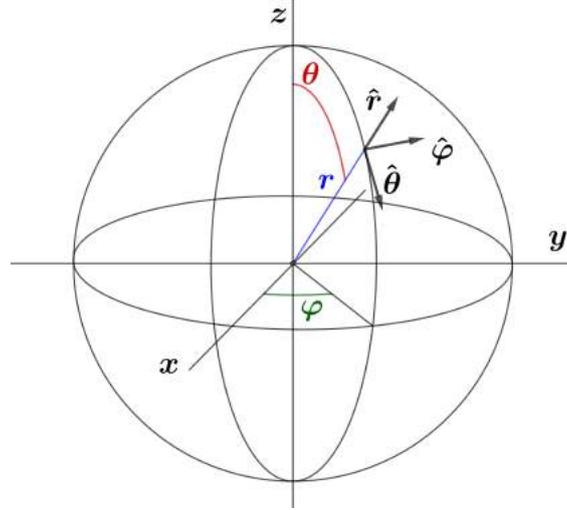
Figure I.2: The spherical coordinates and the spherical basis.

harmonic by looking at each frequency independently, which happens in practice as antenna measurements requires a discretization of the frequency axis, also called electrical axis. Thus $\mathbf{E}(t, r, \theta, \varphi) = e^{\pm j\omega t}\mathbf{E}(r, \theta, \varphi)$ where $\omega = 2\pi f$ with f the considered frequency. The sign of the exponent sets the time convention and can be chosen arbitrarily for antenna measurements. An example of an electric field pattern simulated using CST is shown in Fig. I.3.
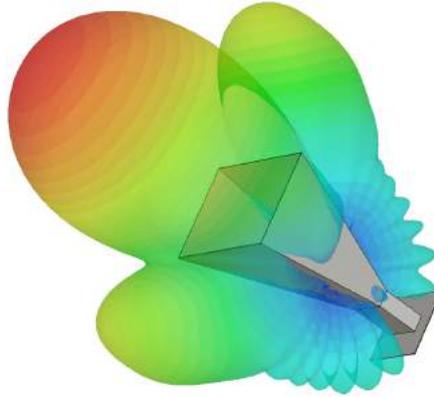
Figure I.3: The electric far-field magnitude of a standard gain horn in X band simulated using Computer Simulation Technology (CST) [2] Wavestudio.

The electromagnetic fields are vectors and different conventions can be used to describe them. In the case of spherical measurements, the spherical coordinate basis, given by $(\hat{r}, \hat{\Theta}, \hat{\varphi})$ in Fig. I.2 is often considered. The co- and cross-polarization definitions by Ludwig [3] are also often used in practice. The third Ludwig definition transforms the spherical basis into what can be called a Horizontal/Vertical basis in most cases (due to the orientation of the probe polarization in the anechoic chamber corresponding to these directions), $(\hat{r}, \hat{v}, \hat{h})$. This transformation is defined as shown in Fig. I.4.
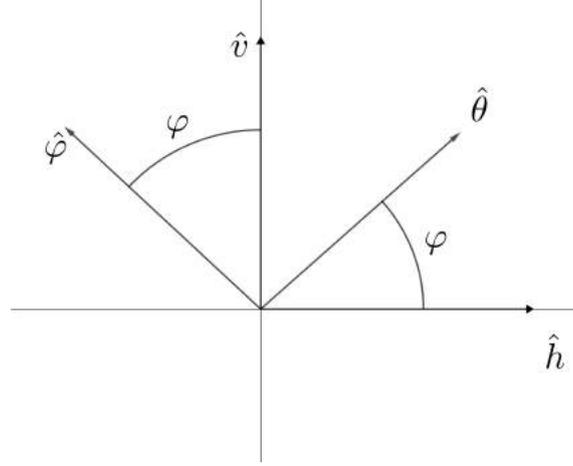
Figure I.4: The transformation between the spherical basis and the third definition of co- and cross-polarization by Ludwig.

Gain and Directivity

Antennas can emit or receive power. This means that the interaction between such systems is enabled by a power flux [4]. The gain relates this power flux density depending on the direction (θ, φ), to the power accepted by the antenna. The gain G is defined as "the ratio of the radiation intensity in a given direction to the radiation intensity that would be produced if the power accepted by the antenna were isotropically radiated". For a single main-beam antenna, the gain simply refers to the maximum. There are several variations on this definition depending on the consideration of the various losses.

The directivity D connects the power flux density to the total radiated power. It measures how much the power flux is focused in some directions. It is defined as "the ratio of the radiation intensity in a given direction from the antenna to the radiation intensity averaged over all directions". It is given by the equation [5]

$$D(\theta, \varphi) = \frac{4\pi \|\mathbf{E}(\theta, \varphi)\|_2^2}{P_{\mathrm{rad}}} \tag{I.1}$$

where P_{rad} is the radiated power. The radiation efficiency η is defined as the ratio G/D. If all the accepted power by the antenna is radiated, the efficiency is maximal ($\eta = 100$ %).

Polarization

The polarization of an electromagnetic wave is defined by the curve described by the electric field vector through time in a plane perpendicular to the propagation direction. The polarization of the antenna is thus "the polarization of the wave transmitted by the antenna". The polarization of this wave describes how this vector oscillation is behaving with respect to time at a given position. There are 3 main polarization types:

1. Linear polarization: the electric field oscillates within a given plane, see Fig. I.5a.

2. Circular polarization: the electric field oscillates isotropically in all orthogonal directions with respect to the propagation one, see Fig. I.5b.

3. Elliptical polarization: the electric field oscillates in all orthogonal directions with different intensities. The tip of the electric field **E** follows an ellipse.

If not stated otherwise, the polarization of the antenna commonly refers to the one in the maximum gain direction. Circular and elliptical polarizations are given a rotation direction of the field, which can be either left or right handed. For the circular case they are abbreviated LHCP (and RHCP) for Left-Handed (and Right-Handed) Circular Polarization. If the large axis is understood as the propagation direction, a RHCP from the source is seen as LHCP from the receiver point-of-view.
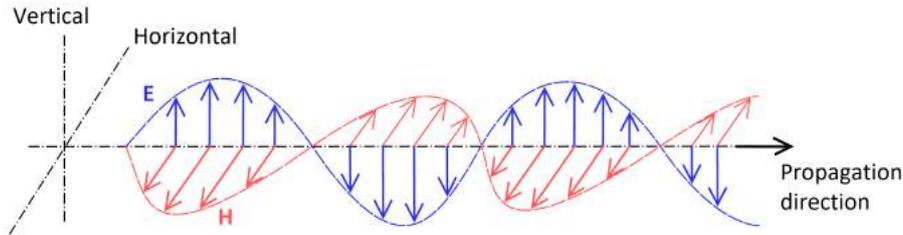
(a) Linear polarization.
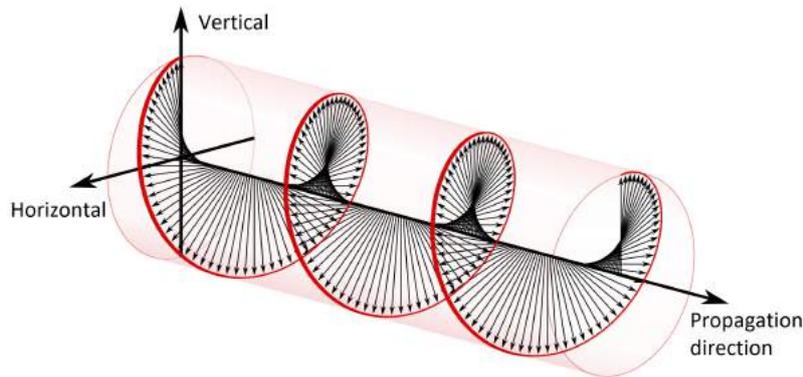
(b) Circular polarization, **E** or **H**.

Figure I.5: (a) The linear and (b) circular polarization types. The vertical and horizontal axes defines the polarization directions. The propagation direction axis can also be understood as a time axis if the electric field is observed at a given position. *Credits: Wikipedia.*

I.2.b   Antenna pattern measurement techniques

There are various techniques to perform an antenna radiation pattern characterization. Its choice depends mainly on the antenna type and application. The measurement techniques are split in two main categories; the near and far-field measurements, depending on the distance between the AUT and the probe. These two regions are defined in [6] as illustrated in Fig. I.6. A typical measurement configuration is made of the AUT or DUT, mounted on a positioning system, and a probe.

In the far-field region, the electromagnetic wave can be approximated locally by planes and the magnitude of the electric field decreases isotropically. The variations of the field are thus determined by the angles only and the measurement distance can be omitted. The electric far field is a function of the spherical coordinates angles (θ, φ) as in Fig. I.2. In the near field, these considerations do not hold, leading to more complicated coupling
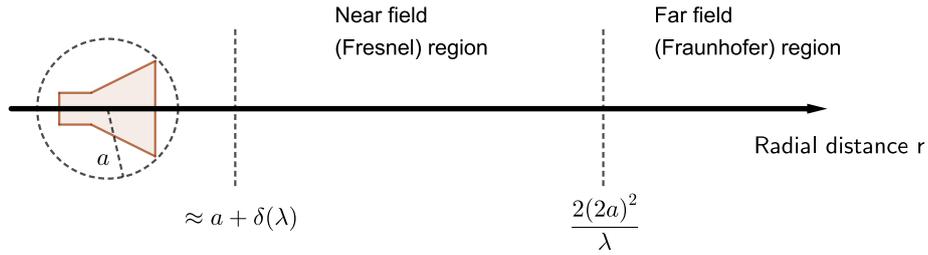
Figure I.6: The measurement regions around the antenna. The radius of the minimal sphere is denoted a and the measured wavelength is λ, $\delta(\lambda)$ is a margin to delimit the reactive region, in which no measurements are feasible.

computations and measurement procedures. However the far field might be out of reach in practice. For example, an antenna operating at 30 GHz and mounted on a satellite having maximal size 2 m has a far-field region at 80 m according to the relation given in Fig. I.6.

Near-field ranges

In most near-field measurement systems, the measurement data is expanded into a modal basis. The complicated function representing the electrical field is thus represented by an expansion into a known function basis and the antenna pattern characterization consists in the determination of the expansion coefficients, the weights, of the radiation pattern in the basis. This expansion allows in particular to transform the field and consequently to derive the far field (often called Near to Far Field Transformation, NFFT). Because of this transformation, such techniques are sometimes called *indirect measurements* [4]. The main point of near-field testing is to avoid the possibly very large measurement distances or complex measurement configurations, then performing a transformation to obtain the far field. There are three main types of near-field measurements: planar, cylindrical and spherical. For all three, the pattern of the probe has to be compensated in some way.

For the usual planar measurement technique, the NFFT is performed by a Fourier Transform, requiring a constant step sampling. However, the constraint imposed by this post-processing technique over the sampling as led to a lot of research on this domain. For example, spiral scanning over the plane have been developed in [8] to reduce the number of required field samples. The principle of a standard planar scanning system is shown in Fig. I.7.

A widely measurement type is the spherical near field, leading to an IEEE standard procedure document [9] and well known for its accuracy [10]. Similarly as in the planar measurements, the usual technique requires a constant angular step sampling in both directions θ, φ, leading to possibly prohibitive field acquisition times when used with the standard method described by Hansen [6]. The cylindrical measurements are close to the spherical ones. This method is particularly adapted for the characterization of antennas for radar applications with azimuthal scanning.

Far-field ranges

By definition, the measured signal from the probe in far field is considered to be the electric field, allowing a direct measurement of this quantity. However, to speed up the 3D characterization process, an interpolation using a function basis can still be performed.
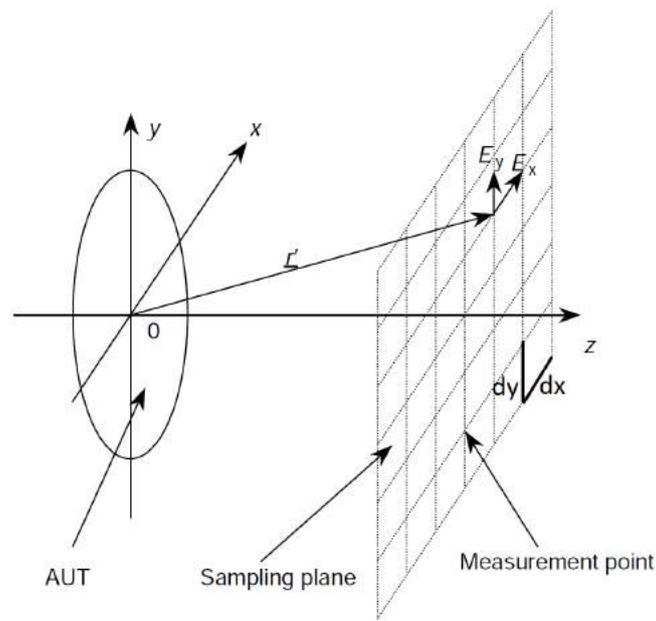
Figure I.7: Coordinate system for planar scanning, adapted from [7].

The experimental data presented in this manuscript is in the far field.

Because of possibly long measurement distances, making the true far field impossible for indoor measurements, outdoors systems have been developed but are heavily impacted by the environment. Fortunately, we can reach the far-field condition using collimating elements, such systems are know as Compact Antenna Test Range (CATR) [4]. While the usual definition of the far field involves the distance between the probe and the AUT, it is truly characterized by the fact that the emitted electromagnetic waves can be approximated locally by planes, as detailed in [7]. CATR systems generate a plane wave using lens and/or reflectors, allowing to reach the far field without resorting to large measurement configurations. An example of such measurement system is sketched in Fig. I.8. Two photographies of CATR system are shown in Fig. I.11.a for the IETR-UR1 one, with a rolled edge reflector, and in Fig. I.9 for the one located at CNES, with a serrated edge reflector.
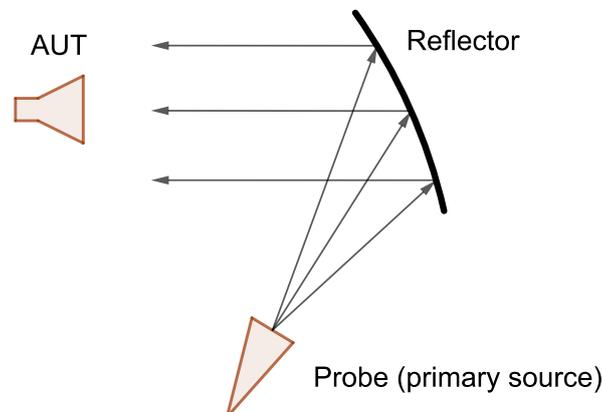
Figure I.8: An example of a CATR measurement configuration.

Figure I.9: CATR measurement at CNES with a serrated reflector. *Credits: D. Belot, CNES.*

While being powerful, such systems are costly as the reflectors have to be designed and calibrated very carefully within the measurement environment. The operator also has to ensure that the AUT is within the so-called quiet zone, the region where the reflected wave from the primary source is planar. The reflector size is proportional to the generated quiet zone, and its shape accuracy defines the upper bound of the frequency range. Moreover, the feeds have to fulfil radiation pattern symmetry and phase centre stability. These constraints are major problem for submillimetric wave applications.

I.2.c IETR measurement facilities

The antenna characterization equipments are regrouped under the M^{2}ARS division for the UR1 part (it stands for Manufacturing Measurement Analysis of Radiating Systems) [11], managed by L. Le Coq. These equipments are about to evolve significantly at the time of this manuscript. They currently contain, among prototyping equipments and measurement systems for other tasks:

1. A planar near-field system for measurements between 10 GHz and 500 GHz, illustrated in Fig. I.10.

2. Two spherical measurement systems in far field, CAMILL (for millimetric and submillimetric operating antennas), using CATR or direct illumination configurations and CACENDRA (for centimetric operating antennas), illustrated in Fig. I.11.

These spherical systems are roll-over-azimuth sequential positioners with a step-by-step field acquisition (complete stop at each sampling position) and a mechanical or electrical change of the polarization. An illustration of such system is shown in Fig. I.12, the relation with the spherical coordinates defined in Fig. I.2 is also displayed.

Other equipments are located in the INSA part of the laboratory. The antenna characterization part involves two near-field spherical scanners provided by two MVG multi-probe systems, Stargate SG32 and MVG Starlab [12], illustrated in Fig. I.13. The former system operates between 0.65 and 18 GHz, the antenna is positioned at the center of an arch containing multiple probes, the AUT rotates over one axis to perform the spherical scan.

Figure I.10: Near-field planar measurement system of IETR-UR1 - 10 to 500 GHz.

(a) CAMILL - 18 to 330 GHz.

(b) CACENDRA - 0.8 to 26 GHz.

Figure I.11: Spherical far-field measurements systems of IETR-UR1. (a) A horn in CA-MILL with the rolled edge reflector for CATR measurements (direct illumination also possible). (b) A Luneburg lens on the positioning system of CACENDRA.

Figure I.12: Roll-over-azimuth positioning system for spherical measurements of IETR-UR1.

An oversampling can be achieved by a slight tilt of the arch to move the probes, enabling thin but fast spherical scans with a limited number of probes.

I.3   Antenna radiation pattern measurement

The radiation pattern of the antenna is measured to perform the characterization of its radiation properties. This section introduces the metrics used to compare these measurements, the number of required field samples and the duration of their acquisition.

Figure I.13: StarLab multi-probe system from MVG with its calibration horn located at IETR-INSA [13].

I.3.a   Metrics for antenna pattern comparison

In order to assess a new measurement technique or configuration, to chose between two different DUT operating modes and so on, one has to use metrics to compare the obtained radiation patterns. The comparison between these patterns can be achieved using two approaches: point-wise or global comparison. The point-wise comparison of two patterns provides a new pattern, depending on the used metric, while a global comparison of two patterns returns a single number to evaluate the proximity between the two. This number can be used as an objective function for optimization purposes or to compare the accuracy of different post-processing methods. In this section, $f_1(\theta, \varphi)$ and $f_2(\theta, \varphi)$ are two radiation patterns over the sphere and $\mathbf{y}_1, \mathbf{y}_2$ their corresponding discretizations over the same sampling.

Point-wise metrics

Each point-wise comparison metrics will emphasize on some aspects of the differences between the compared patterns. The choice mainly depends on what differences are looked more specifically. The presented metrics are all defined in [14].

$$
\begin{aligned}
\Delta_{\mathrm{lin}}(\theta, \varphi) &= |f_1(\theta, \varphi) - f_2(\theta, \varphi)| & \text{Linear difference} \\
\Delta_{W,\mathrm{lin}}(\theta, \varphi) &= W_{\mathrm{lin}}\Delta_{\mathrm{lin}}(\theta, \varphi) & \text{Weighted lin. diff.}
\end{aligned}
$$

$$
\begin{aligned}
\Delta_{\mathrm{log}}(\theta, \varphi) &= 20\log_{10}|f_1(\theta, \varphi)| - 20\log_{10}|f_2(\theta, \varphi)| & \text{Logarithmic difference} \\
\Delta_{W,\mathrm{log}}(\theta, \varphi) &= W_{\mathrm{log}}\Delta_{\mathrm{log}}(\theta, \varphi) & \text{Weighted log. diff.}
\end{aligned}
$$

The weighting functions W_{lin} and W_{log} are used to mitigate the differences between the patterns over regions where the comparison is not relevant. For example, if a measurement configuration is known to produce reliable patterns down to -50 dB, focusing on the differences occurring at -60 dB is highly questionable. An example of such weighting function, with s the magnitude in dB of the normalized reference pattern f_1 with a minimum confidence of -60 dB, is defined in [14] by

$$
W(s) = \begin{cases} 1 + 10^{-60/20} - 10^{(-60-s)/20} & \text{if} -60 \leq s \leq 0, \\ \text{Discard} & \text{otherwise.} \end{cases}
$$

Let us consider the far-field pattern of an E-plane horn at 30 GHz to illustrate some of these metrics. The reference is provided by an ideal, theoretical pattern from [5], the simulation is a result given by CST and the measurement is mimicked by the theoretical expression with an additive Gaussian white noise. The patterns are illustrated in Fig. I.14. As illustrated, the logarithmic difference $\Delta_{\log}$ does not assume any confidence level, and all magnitudes in dB are considered with the same importance. Conversely, the weighted difference $\Delta_{W,\log}$ differentiates these differences with respect to the magnitude level. The control of the confidence threshold allows to better fit the reality of the measurement configuration when interpreting the results.

(a) Radiation patterns.   (b) Comparison metrics.
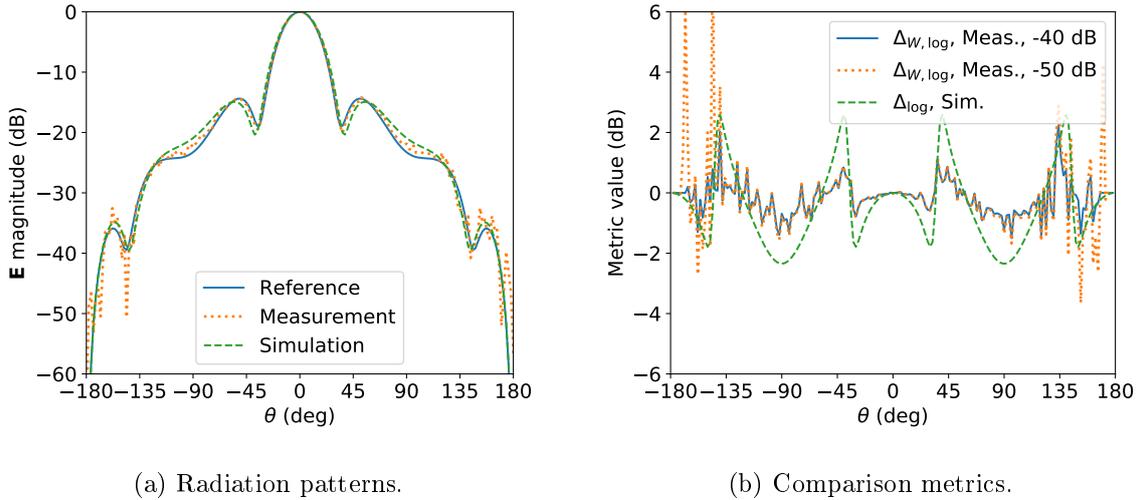
Figure I.14: Pointwise comparison metric values over patterns of an E-plane horn: (a) field magnitude patterns, (b) metrics values between the considered pattern and the reference. Two confidence levels, -40 and -50 dB are used for the weighted logarithmic difference.

Global metrics

Any mathematical norm over a finite space provides such metric in practice, as the field is always discretized in some way. However, specific norms have been developed to better contrast the differences in antenna measurements. It is worth noting that some antenna parameters such as the directivity in (I.1) can also be used as figure of merit to provide comparison metrics.

A standard family of mathematical norms are given by the ℓ_p functions, $p \geq 1$. The ℓ_p norm of a complex vector $\mathbf{y}$ of size M is defined as [15]

$$\|\mathbf{y}\|_p = \left(\sum_{i=1}^{M} |y_i|^p \right)^{1/p} \tag{I.2}$$

This definition can be extended to $p = \infty$. The ℓ_∞ or ∞-norm of $\mathbf{y}$, $\|\mathbf{y}\|_\infty$, is the maximum modulus component of $\mathbf{y}$. As a side-note, the ℓ_2 norm is also known as the Euclidean norm and corresponds to the intuitive notion of distance in a 2D or 3D space. Most of the global comparison metrics used in antenna measurements have convenient expressions when expressed using the ℓ_p norms.

The relative residual field is the normalized ℓ_2 norm of the difference introduced in [16]. It mostly emphasizes on the errors in the highest magnitudes regions between a reference, discretized in $\mathbf{y}_1$, and another field discretization $\mathbf{y}_2$, eventually an estimation of the reference. It is defined as

$$\varepsilon(\mathbf{y}_1, \mathbf{y}_2) = \frac{\|\mathbf{y}_1 - \mathbf{y}_2\|_2}{\|\mathbf{y}_1\|_2}. \tag{I.3}$$

If $\mathbf{y}_2$ is expected to be a good estimate of $\mathbf{y}_1$, the value should be close to 0. The degree of correlation [16,17] rather measures the proximity between two fields, a value of 1 indicating that the two vector are the same. It indicates if the two patterns follows close variations, but is not very sensitive to slight, local, differences such as additive noise with low magnitude. It is defined as

$$\delta(\mathbf{y}_1, \mathbf{y}_2) = \frac{\|\langle \mathbf{y}_1, \mathbf{y}_2 \rangle\|_2^2}{\|\mathbf{y}_1\|_2^2 \|\mathbf{y}_2\|_2^2}, \tag{I.4}$$

where $\langle \mathbf{y}_1, \mathbf{y}_2 \rangle$ is the Hermitian product.

Finally, the Equivalent Noise Level [18], ENL, is a normalized mean error in dB between a reference $\mathbf{y}_1$ and another field $\mathbf{y}_2$, as in the relative residual field[1]. This metric should be considered when the two vector fields are expected to be close to each other in a uniform manner over the measurement region. Because of the mean operation, a localized significant difference, even in the main beam, might be out of sight if the fields in the others regions are very similar. However, this metric has the advantage to provide an intuitive result and ENL can be easily compared between various comparison scenarios. It is defined as

$$\text{ENL}(\mathbf{y}_1, \mathbf{y}_2) = 20 \log_{10} \left(\frac{\|\mathbf{y}_1 - \mathbf{y}_2\|_1}{M \|\mathbf{y}_1\|_\infty} \right). \tag{I.5}$$

Gaussian noise mean (dB)	-40	-50	-60
Residual field ε	1.12×10^{-3}	1.03×10^{-4}	9.88×10^{-6}
Correlation degree δ (%)	99.95	99.99	99.99
Equivalent Noise Level ENL (dB)	-38.9	-48.3	-58.7

Table I.1: Global comparison metrics value for the E-plane horn between the reference and the noisy patterns of Fig. I.15.

An illustration of these metrics is given by considering the far-field pattern of an E-plane horn at 30 GHz. The normalized reference pattern and three altered versions using additive Gaussian/white noise with different mean magnitudes are shown in Fig. I.15. The corresponding values of the aforementioned metrics are in the table I.1. The link between the ENL and the noise mean magnitude is quite clear. Similar variations can be observed with the residual field but over a different scale, where reducing the noise mean by 10 dB roughly divide the metric value by 10. As claimed, the correlation degree does not discriminate efficiently these different situations because of the additive noise scenario.

---

[1]The Equivalent Error Signal (EES) is used as a synonym to ENL in this manuscript. The EES quantity often refers in the literature to an error radiation pattern instead.
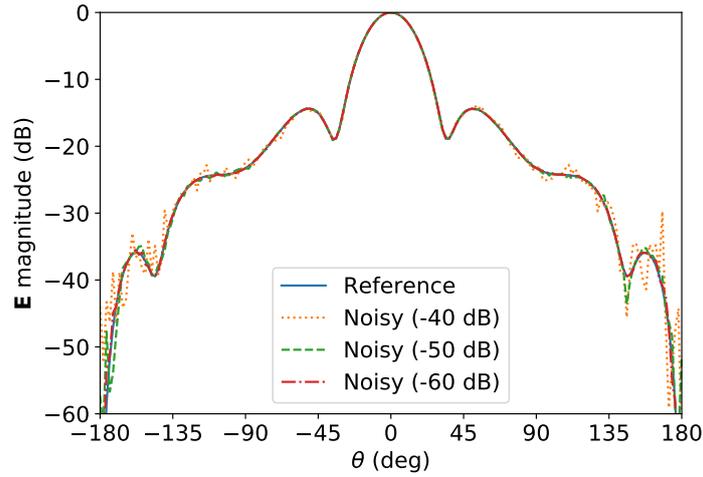
Figure I.15: The E-plane horn pattern magnitude, reference and noisy patterns with multiple Gaussian noise mean magnitudes, -40, -50 and -60 dB.

I.3.b   Number of field samples

The required number of field samples depends on the used measurement technique. The minimum sampling step, either angular or spatial for spherical or planar measurements, respectively, is often referred to as Nyquist sampling rate. Strictly speaking, the Nyquist-Shannon sampling theorem is only valid for a bandwidth limited signal using the Fourier transform [19], such as planar measurements. An example of this sampling limitation is given in Fig. I.16 However, it can be generalized to other transformations or expansions.
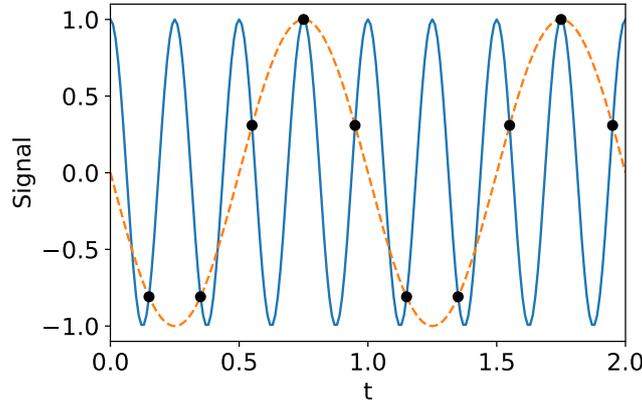
Figure I.16: Illustration of the Nyquist sampling rate: the two signals provide the same time sampling (markers). If the true signal to be characterized is represented by the plain blue line, this measurement sampling rather identifies the orange one (aliasing).

In planar near-field measurements using a square grid, the minimal spatial sampling step is derived in [7] and given by

$$dx = dy = \frac{\lambda}{2\sin\theta_{\max}} \tag{I.6}$$

where θ_{max} stands for the upper bound in θ for which the characterization is achieved and the steps dx, dy are the distance between two sampling points in the x and y direction of the plane. These quantities are illustrated in Fig. I.17. The steps are also shown in 2D in Fig. I.7. According to sampling theory, it allows an exact reconstruction of a properly bandwidth limited signal in the characterized region determined by θ_{max}.
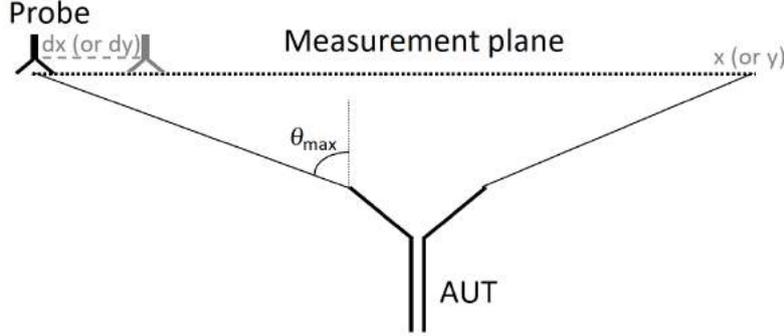
Figure I.17: A planar near-field system scheme, adapted from [7]. θ_{max} is the half field of view and dx or dy the steps between two sampling positions over the measurement plane.

For spherical near and far field, the angular step between the sampling positions given by the spherical wave theory in the famous book by Hansen [6], and is

$$\delta\theta = \frac{\pi}{N+1}, \delta\varphi = \frac{2\pi}{2N+1} \tag{I.7}$$

where $N = \lfloor ka \rfloor + n_1$ with k the wavenumber and a the minimal sphere radius, the sphere centered at the origin of the measurement coordinate system and enclosing all the sources, as illustrated in Fig. I.6, n_1 is an integer usually set to 10. It leads to the following total number of samples

$$M_H = 2(N+1)(2N+1). \tag{I.8}$$

Note the factor 2 at the beginning, coming from the two orthogonal polarizations measured for each sampling position.

If the sources (the DUT) are enclosed in a large surface Σ (in terms of electrical length), Bucci *et al.* [20] gives another formula

$$M_B = 2\frac{\mathcal{A}(\Sigma)}{(\lambda/2)^2} \tag{I.9}$$

where $\mathcal{A}(\Sigma)$ stands for the area of the surface Σ enclosing the sources and the factor 2 comes from the polarizations per position, as before. According to the authors, an oversampling is required for successful characterization.

I.3.c   Duration of the field acquisition

The duration of the field acquisition is impacted by numerous factors. For a given measurement configuration, the sampling strategy and the number of samples are the critical ones. Using a simple rigid modelling of the positioning engines cinematic and time-stamped measurements, we are able to estimate the field acquisition time for given sampling in IETR

anechoic chamber CACENDRA. More details are available in the Appendix A. The steps of the acquisition procedure for samplings having cuts in θ in this system are:

1. Measurement of one polarization component of the field for a fixed θ, varying φ.

2. Mechanical change of the measured field polarization (rotation of the probe).

3. Same as step 1 for this new polarization.

4. Returning to the first polarization orientation and moving to the next θ.

5. Repeat steps from 1 to 4 until all θ have been run through.
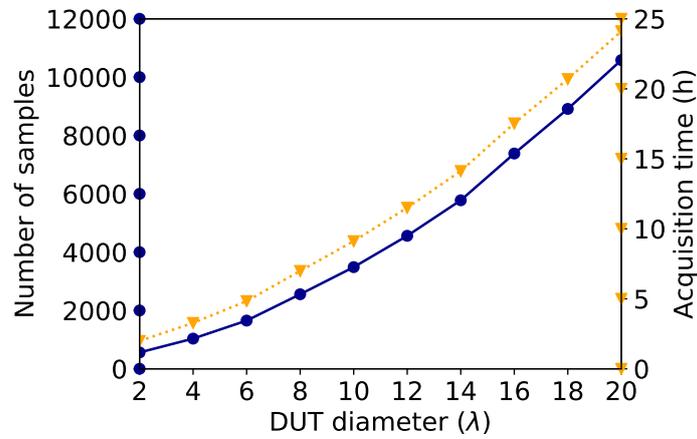
Figure I.18: Number of samples M_H according to spherical near-field measurement theory and estimated field acquisition time in IETR anechoic chamber CACENDRA.

According to the spherical measurement theory [6], the number of field samples is determined by the maximum electrical size of the DUT and the sampling has to follow an equiangular sampling (constant step in both $\delta\theta$ and $\delta\varphi$, which can be different). The results are shown in Fig. I.18. We clearly observe the link between the field acquisition duration and the number of samples. Note however that this agreement can be less obvious using different measurement system configurations and sampling strategies (using a continuous acquisition and a spiral scanning for example).

Bibliography

[1] IEEE standard for definitions of terms for antennas. *IEEE Std 145-2013 (Revision of IEEE Std 145-1993)*, pages 1–50, 2014.

[2] Cst studio suite 2020. Technical report, Dassault Systèmes. Available at https://www.3ds.com/fr/produits-et-services/simulia/produits/cst-studio-suite/.

[3] A. C. Ludwig. The definition of cross polarization. *IEEE Trans. on Antennas and Propag.*, AP-21:116 – 119, 02 1973.

[4] J. Mccormick, C. Parini, S. Gregson, and D. Janse Van Rensburg. *The Theory and Practice of Modern Antenna Test Range Measurements*. Jan 2014.

[5] C. A. Balanis. *Antenna Theory: Analysis and Design*. Wiley-Interscience, 2005.

[6] J. Hald, J.E. Hansen, F. Jensen, and F.H. Larsen. *Spherical Near Field Antenna Measurements*. Peter Peregrinus, 1988.

[7] Gregson S., McCormick J., and Parini C. *Principles of Planar Near-Field Antenna Measurements*, volume Series 53. IET, 2007.

[8] R.G. Yaccarino, L.I. Williams, and Y. Rahmat-Samii. Linear spiral sampling for the bipolar planar near-field antenna measurement technique. *IEEE Transactions on Antennas and Propagation*, 44(7):1049–1051, 1996.

[9] IEEE recommended practice for near-field antenna measurements. *IEEE Std 1720-2012*, pages 1–102, 2012.

[10] O. Breinbjerg. Spherical near-field antenna measurements — the most accurate antenna measurement technique. In *2016 IEEE International Symposium on Antennas and Propagation (APSURSI)*, pages 1019–1020, 2016.

[11] Plateforme M2ARS. IETR-UR1, 2020. Available at https://www.ietr.fr/plateforme-m2ars-manufacturing-measurement-analysis-radiating-systems.

[12] Starlab 650MHz-18GHz. MVG, 2020. Available at https://www.mvg-world.com/fr/products/antenna-measurement/multi-probe-systems/starlab.

[13] Bases de mesure champ proche. IETR-INSA, 2020. Available at https://www.ietr.fr/bases-de-mesure-champ-proche.

[14] S. Pivnenko, J. E. Pallesen, O. Breinbjerg, M. S. Castaner, P. C. Almena, C. M. Portas, J. L. B. Sanmartin, J. Romeu, S. Blanch, J. M. Gonzalez-Arbesu, C. Sabatier, A. Calderone, G. Portier, H. Eriksson, and J. Zackrisson. Comparison of antenna measurement facilities with the dtu-esa 12 ghz validation standard antenna within the eu antenna centre of excellence. *IEEE Trans. on Antennas and Propag.*, 57(7):1863–1878, July 2009.

[15] S. Boyd and L. Vandenberghe. *Convex Optimization*. Cambridge University Press, New York, NY, USA, 2004.

[16] G. Giordanengo, M. Righero, F. Vipiana, M. Sabbadini, and G. Vecchi. Fast antenna testing with reduced near field sampling. *IEEE Trans. on Antennas and Propag.*, 62(5):2501–2513, May 2014.

[17] G. Minatti, S. Maci, P. De Vita, A. Freni, and M. Sabbadini. A circularly-polarized isoflux antenna based on anisotropic metasurface. *IEEE Trans. on Antennas and Propag.*, 60(11):4998–5009, Nov 2012.

[18] F. Saccardi, F. Rossi, L. Scialacqua, and L. J. Foged. Truncation error mitigation in free-space automotive partial spherical near field measurements. In *AMTA 2017*, pages 1–6, Oct 2017.

[19] C. E. Shannon. Communication in the presence of noise. *Proceedings of the IRE*, 37(1):10–21, 1949.

[20] O. M. Bucci, C. Gennarelli, and C. Savarese. Representation of electromagnetic fields over arbitrary surfaces by a finite and nonredundant number of samples. *IEEE Trans. on Antennas and Propag.*, 46(3):351–359, March 1998.

Chapter II

Antenna characterization using sparse spherical wave expansion

II.1 Introduction

II.1.a Motivations

The Spherical Waves (SW) are solutions of the Maxwell's equations in spherical coordinates. Because they also form an orthogonal function basis, they are very convenient to expand and interpolate the radiated spherical near and far field [1]. The use of SW for the characterization of the antenna radiation pattern is already well established and widely spread in the antenna measurement community [1–4]. Although very accurate, this standard spherical measurement approach may be time consuming as it requires an important number of field samples. To give some insights, note that the characterization of the 3D radiation pattern of a DUT of diameter 10λ requires at IETR approximately 10 hours for the acquisition of the field, see Fig. I.18. This duration increases drastically in the case of embedded antennas, for which the maximal electrical size of the DUT includes the whole structure that contributes inevitably to the radiated field. For all these reasons as well as the ones detailed in the global introduction (p. 14), the need for faster antenna characterization based on SW has recently received a lot of attention.

II.1.b State of the art

The SW expansion of the radiated field requires very limited prior knowledge about the DUT: its maximum dimension and the measurement frequency. It also provides an exact computation of the expansion coefficients following a generalized Nyquist sampling rate approach (provided that the signal is bandwidth limited). Moreover, this technique to determine the SW expansion coefficients is robust again noise as coefficients are derived from integral operations. These beneficial aspects come at the price of a high number of required field samples, denoted M_H, where the subscript H stands for Hansen [1]. This number of field samples is $M_H = 2(N+1)(2N+1) \approx 4(\pi D + 10)^2$ with D the diameter of the antenna in wavelength.

Other analytical field expansions have been proposed to tackle the antenna characterization problem. Thus, Prof. Bucci *et al.* [5] have proposed another analytical function basis that is constructed from the radiation operator, with a number of samples also based on a compact bandwidth assumption. Surfaces with a revolution axis that fit the DUT geo-

metry are then used to minimize the number of field samples, as shown in Fig. II.1. This method has also been adapted numerically to further account for the antenna geometry [6].

Figure II.1: The DUT is enclosed in a convex shape Σ, allowing to reduce the number of field samples [5].

Numerical basis can also be constructed in order to reduce the number of field samples, provided that detailed information are available on the DUT. The presentation of this type of approaches is left for the Chapter IV that precisely proposes such a technique to speed up antenna measurements.

The fields radiated by the DUT exhibit regularities and symmetries. These physical properties render the spherical wave spectrum of antennas to be sparse. It means that a small number of SW are sufficient to described the pattern radiated by antennas. This sparsity aspect has been noticed in [7] and first exploited for antenna characterization in [8] and [9]. The authors have shown that sparse recovery algorithms can be used to characterize antennas with fewer samples than number of unknowns (SW expansion coefficients). Since many SW are negligible, as illustrated in Fig.II.2, the number of required field samples can be significantly reduced. According to the authors of [8], the number of field samples can be reduced by a factor up to 75 % with respect to the Nyquist rate equivalent, also known as the standard method.

This sparse SW expansion technique has been applied successfully in the far field [10] using scalar SW with a sampling strategy well suited for IETR positioning systems (sequential roll-over-azimuth with step-by-step acquisition) called the *igloo* sampling. This sampling has also the advantage to be distributed almost uniformly over the sphere while enabling efficient spherical scans.

The under-sampling theory [11] applied to fast antenna measurements has led to considerations on more sophisticated samplings to better harness the mathematical properties of sparse recovery. To this end, a sampling that minimizes the cross correlation between the discretization of the basis functions has been proposed by [12]. Even if the SW form an orthogonal basis of functions over a sphere, their discretization does not necessarily lead
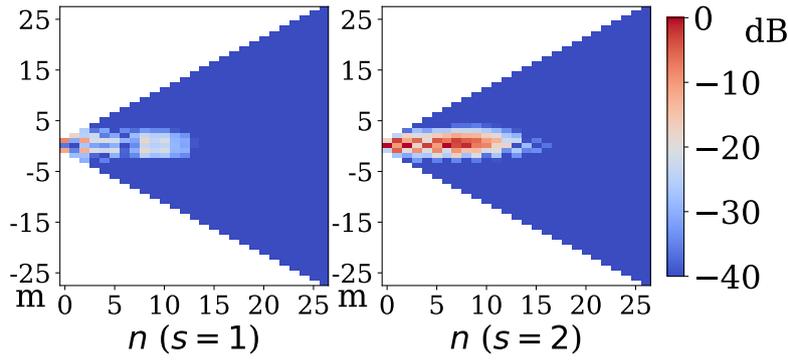
Figure II.2: An example of SW expansion coefficient spectrum (simulated patch array in X band). Many SW coefficients have a magnitude that can be neglected, lower than -40 dB as compared to the maximum level.

to orthogonal vectors. However, orthogonality can be promoted by optimizing the position of the field samples. Three examples of field samples with various number of points that induce a low mutual coherence of the sensing matrix are shown in Fig. II.3. However, the complicated distribution of the field samples over the sphere remains a problem for the scan in practice.
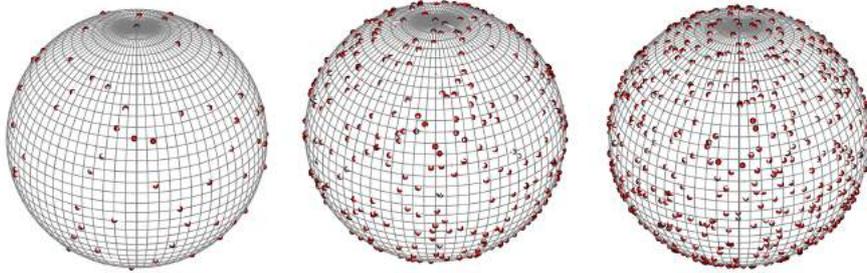

Figure II.3: Spherical samplings (red dots) with low correlation between the SW discretization for $M = 97, 500$ and 800 measurement points [12].

Besides,Phase Transition Diagrams (PTD) are a useful representation, also coming from the under-sampling theory [13], to draw conclusions on the number of samples using various sampling strategies to ensure successful characterization using sparse recovery techniques [14]. These transitions are evaluated by randomly drawing large families of expansion coefficients which are being retrieved by sparse recovery algorithm from the fields they generate. By doing so, it is possible to give an estimation of the probability of successful coefficients identification, and thus of the proper antenna characterization. The value of this probability depends on the number of field samples, the number of SW and the number of significant SW expansion coefficients. Roughly speaking, the smaller the number of significant SW coefficients, the smaller the number of field samples. This expected and intuitive rule of thumb is illustrated by the PTD in Fig. II.4. If $\zeta = 20$ % of the coefficients are non-zero, only $\delta \approx 50$ % of sampling data are required with respect to the number of coefficients to determine. If the proportion of non-zero coefficients increase to $\zeta = 40$ %, then $\delta \approx 80$ % are required. Interestingly, it appears that only a few samples separate a failing recovery from a successful one. This sharp transition is discussed in [13].
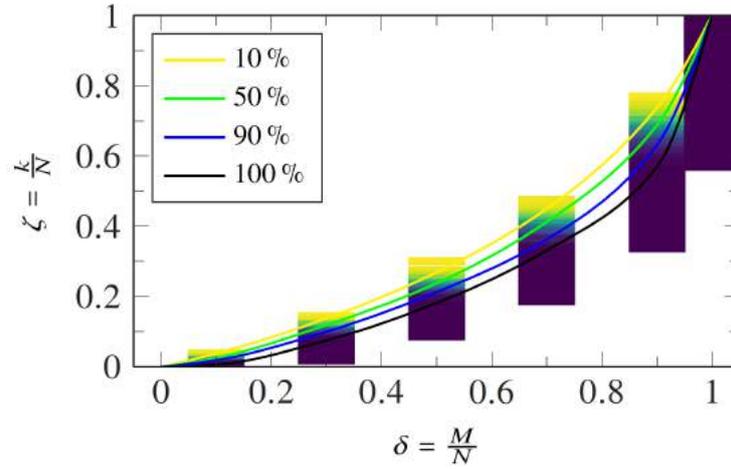
Figure II.4: An example of phase transition diagram for antenna measurements from [14]. The probability of successful recovery of the coefficients is a function of the number of field samples M, the number of unknowns N and the number of non-zero coefficients k.

II.1.c   Contributions

This chapter proposes procedures to automatize and render the fast antenna pattern characterization via sparse SW expansion more reliable. The sparse recovery algorithms, that are necessary for our fast measurement procedure, are not parameter free. More specifically, they require the proper tuning of a regularization parameter, which can be understood in our problem as an error tolerance, also known as data fitting. A procedure to automatically choose this parameter by going through several solutions using a reduced set of field samples is proposed.

Besides, the field sampling strategy is a crucial point to ensure a successful fast antenna measurement procedure. The number of field samples and the sampling distribution over the sphere are addressed by exploiting and extending the conventional use of phase transition diagrams. Realistic assumptions in the derivation of a minimal number of samples suitable for uniform sampling strategies, e.g. the *igloo*, are made and lead to reliable antenna sampling numbers.

Experimental examples and estimated gains in terms of field acquisition duration validate the proposed procedures.

II.2   Spherical wave expansion

II.2.a   Introduction of the spherical waves

The electromagnetic field $(\mathbf{E}, \mathbf{H})$ in a linear, isotropic and homogeneous medium with an assumed harmonic time dependence in $e^{-j\omega t}$ are solutions to the following Maxwell's equations [1]

$$\nabla \times \mathbf{H} = -j\omega\varepsilon\mathbf{E} + \mathbf{J}, \tag{II.1}$$

$$\nabla \times \mathbf{E} = j\omega\mu\mathbf{H} - \mathbf{M}. \tag{II.2}$$

where $\omega = 2\pi f$, f being the frequency, and ε, μ are the permittivity and the permeability of the medium and $\mathbf{J}, \mathbf{M}$ are the electric and magnetic currents, respectively.

Furthermore, when the considered propagation region is source-free, this equation simplifies as the currents are identically zero, $\mathbf{J} \equiv \mathbf{0}$, $\mathbf{M} \equiv \mathbf{0}$. Then, the electromagnetic field satisfies the so-called vector wave equation

$$\nabla \times (\nabla \times \mathbf{E}) - k^2 \mathbf{E} = \mathbf{0} \tag{II.3}$$

where $k = 2\pi/\lambda$ is the propagation constant or the wavenumber, λ being the wavelength.

The SW form an orthogonal function basis of the solutions of the vector wave equation (II.3). More specifically, they provide an orthogonal basis of the space of square integrable functions over the sphere [15]. It means in particular that any continuous function on the sphere, such as the electric field radiated by antennas, can be expanded into the SW basis. Thanks to these two properties, the use of such function basis in a spherical antenna measurement context is relevant.

The SW, as solutions to the vector wave equation (II.3), are obtained using the separation of variables technique. A SW is a product of three functions, each of them depends on one spherical coordinate, r, θ and φ. A SW is described by one index specifically for the radial dependency, the propagation type c (standing, travelling inward or outward waves) and three more indexes being the propagation mode s, Transverse Electric or Magnetic, (TE or TM), the degree n and the order m. The SW $F_{smn}^{(c)}$ are expressed as follow

$$\mathbf{F}_{smn}^{(c)}(r, \theta, \varphi) = \text{Radial}(r) \times \text{Elevation}(\theta) \times \text{Azimuth}(\varphi). \tag{II.4}$$

II.2.b   Definitions

Azimuth dependency:

The azimuth part in φ depends on the order m only and simply reads: $\text{Azimuth}(\varphi) = e^{im\varphi}$.

Elevation dependency: Legendre polynomials

The Legendre polynomials of degree n, denoted P_n are solutions of the following equation over $[-1, 1]$

$$\frac{\mathrm{d}}{\mathrm{d}x}\left[(1-x^2)\frac{\mathrm{d}}{\mathrm{d}x}P_n(x)\right] + n(n+1)P_n(x) = 0. \tag{II.5}$$

In particular, they form an orthogonal basis of continuous functions over $[-1, 1]$. These polynomials are converted into the associated Legendre polynomials P_n^m, that depends both on the order m and the degree n, defined in θ as [1]

$$P_n^m(\cos\theta) = (\sin\theta)^m \frac{\mathrm{d}^m}{\mathrm{d}(\cos\theta)^m} P_n(\cos\theta). \tag{II.6}$$

They can be normalized so that their integral over $\theta \in [0, \pi]$ is equal to unity, as follows

$$\overline{P}_n^m(\cos\theta) = \sqrt{\frac{2n+1}{2}\frac{(n-m)!}{(n+m)!}} P_n^m(\cos\theta). \tag{II.7}$$

where ! is the factorial operator (for any integer n, $n! = 1 \times 2 \times \cdots \times n$).

These normalized associated Legendre polynomials are the elevation part of the spherical vector wave functions (II.4), i.e. $\text{Elevation}(\theta) = \overline{P}_n^m(\cos\theta)$.

Radial part: Bessel functions

The radial part can be used to represent four propagation types: $c = 1$ or 2 for standing waves, $c = 3$ for outward travelling waves and $c = 4$ for inward travelling waves. The radial dependency depends on the degree n. Following the notations in [1], the radial dependency is denoted $\text{Radial}(r) := z_n^{(c)}(kr)$ in (II.4) and defined as

$$
\begin{aligned}
z_n^{(1)}(kr) &= j_n(kr) && \text{Spherical Bessel} \\
z_n^{(2)}(kr) &= n_n(kr) && \text{Spherical Neumann} \\
z_n^{(3)}(kr) &= h_n^{(1)}(kr) && \text{Spherical Hankel (1}^{\text{st}}\text{ kind)} \\
z_n^{(4)}(kr) &= h_n^{(2)}(kr) && \text{Spherical Hankel (2}^{\text{nd}}\text{ kind)}
\end{aligned}
$$

where r is the distance to the origin.

Spherical vector wave functions

The general expressions of the normalized SW are [1]

$$
\mathbf{F}_{1mn}^{(c)}(r,\theta,\varphi) = N_{n,m} e^{jm\varphi} z_n^{(c)}(kr) \left(\frac{jm \overline{P}_n^{|m|}(\cos\theta)}{\sin\theta} \hat{\theta} - \frac{\mathrm{d}\overline{P}_n^{|m|}(\cos\theta)}{\mathrm{d}\theta} \hat{\varphi} \right) \tag{II.8}
$$

$$
\begin{aligned}
\mathbf{F}_{2mn}^{(c)}(r,\theta,\varphi) = N_{n,m} e^{jm\varphi} &\left[\frac{n(n+1)}{kr} z_n^{(c)}(kr) \overline{P}_n^{|m|}(\cos\theta) \hat{r} \right. \\
&\left. + R_{2n}^{(c)}(kr) \left(\frac{\mathrm{d}\overline{P}_n^{|m|}(\cos\theta)}{\mathrm{d}\theta} \hat{\theta} + \frac{jm \overline{P}_n^{|m|}(\cos\theta)}{\sin\theta} \hat{\varphi} \right) \right]
\end{aligned} \tag{II.9}
$$

where $N_{n,m}$ and $R_{2n}^{(c)}(kr)$ are defined as

$$
N_{n,m} = \frac{1}{\sqrt{2\pi}} \frac{1}{\sqrt{n(n+1)}} \left(-\frac{m}{|m|} \right)^m \tag{II.10}
$$

$$
R_{2n}^{(c)}(kr) = \frac{1}{kr} \frac{\mathrm{d}}{\mathrm{d}(kr)} (kr z_n^{(c)}(kr)) \tag{II.11}
$$

These expressions are used for the computation of the SW. As a side note, quantities such as associated Legendre polynomials and Bessel functions are typically evaluated using recurrence relations. More details about their numerical computation are given in Appendix C.

II.2.c Expansion of the electromagnetic field

General formula

In a source-free region, the electromagnetic field $(\mathbf{E}, \mathbf{H})$ is a solution to the vector wave equation (II.3). Therefore, the radiated field can be expanded into spherical wave functions [1] as follows

$$\mathbf{E}(r, \theta, \varphi) = \frac{k}{\sqrt{v}} \sum_{csmn} Q_{smn}^{(c)} \mathbf{F}_{smn}^{(c)}(r, \theta, \varphi) \tag{II.12}$$

$$\mathbf{H}(r, \theta, \varphi) = -jk\sqrt{v} \sum_{csmn} Q_{smn}^{(c)} \mathbf{F}_{3-s,m,n}^{(c)}(r, \theta, \varphi) \tag{II.13}$$

where v is the admittance[1] of the propagation medium and $Q_{smn}^{(c)}$ are the complex SW expansion coefficients. When the observation point (r, θ, φ) is outside the minimal sphere, which center is at the origin and containing all the sources, the value $c = 3$ suffices to expand the field and the expansion of the electric field (II.12) simplifies to

$$\mathbf{E}(r, \theta, \varphi) = \frac{k}{\sqrt{v}} \sum_{s=1}^{2} \sum_{n=1}^{\infty} \sum_{m=-n}^{n} Q_{smn}^{(3)} \mathbf{F}_{smn}^{(3)}(r, \theta, \varphi). \tag{II.14}$$

A similar expression can be derived for the magnetic field based on II.13. Consequently, the characterization of the radiated field of the antenna boils down to the identification of $Q_{smn}^{(3)}$, often called spherical coefficients. For convenience, the c dependence is omitted in the sequel and the coefficients are denoted as Q_{smn} unless stated otherwise. The same is done for $\mathbf{F}_{smn}^{(3)}$, denoted $\mathbf{F}_{smn}$. The spherical coefficients are usually displayed using two triangles, one for each propagating mode $s = 1$ for TE and $s = 2$ for TM, using the pattern shown in Fig. II.5.

Truncation order

The expansion of the electric field (II.14) is a series over the degree n. For a numerical implementation, this series can be truncated according to the electrical length of the minimal sphere by the following rule [1]

$$N = \lfloor ka \rfloor + n_1 \tag{II.15}$$

where a is the radius of the minimal sphere, as shown in Fig. II.6. The positive integer n_1 is a safety margin introduced to mitigate potential truncation errors. This margin is usually set to $n_1 = 10$. As a side note, it can be safely reduced when expanding the far field. The summation of (II.14), $\sum_s \sum_n \sum_m$ is written $\sum_{smn}$ for convenience in the sequel.

---

[1]The reference [1] rather uses η for the admittance. This notation is saved for impedance in this manuscript.
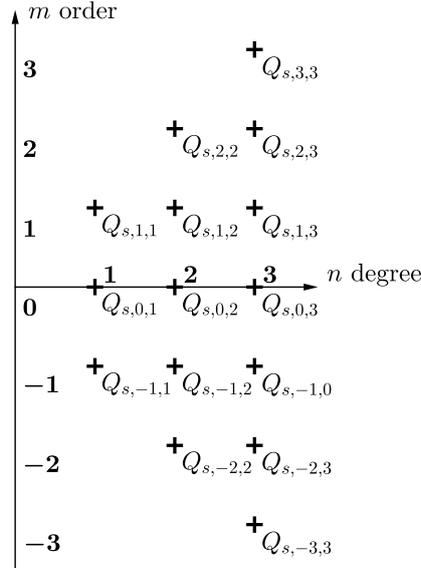
Figure II.5: Triangle representation of spherical coefficients Q_{smn}, each spherical coefficients set contains two of them, one for each s value ($s = 1$ for TE or $s = 2$ for TM).
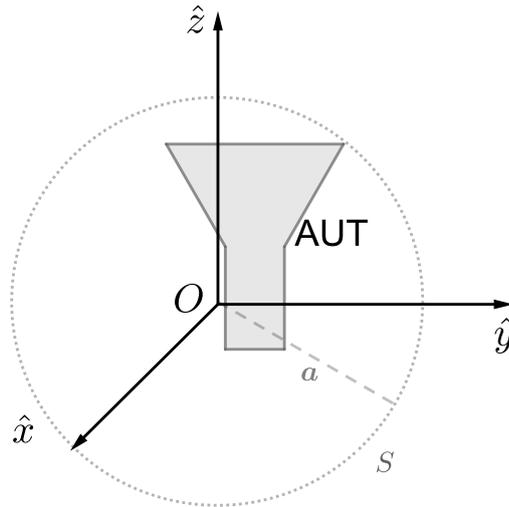

Figure II.6: AUT minimal sphere S of radius a with respect to the measurement coordinate system, whose origin is not necessarily located at the center of the antenna. SW expansion is valid everywhere outside S.

Radiated power

The normalization of the different quantities involved in the definition of the SW allows an easy computation of the radiated power using the following equation

$$P_{\text{rad}} = \frac{1}{2} \sum_{smn} |Q_{smn}|^2. \tag{II.16}$$

A standard sanity check is performed to ensure a proper choice of the truncation order, the N-test [1]. The radiated power can be evaluated individually for a given region of the SW

spectrum. The n-spectrum represents the power radiated for each degree n and is defined as

$$P(n) = \frac{1}{2} \sum_{sm} |Q_{smn}|^2. \tag{II.17}$$

The N-test is satisfied when the n-spectrum decreases significantly as n gets close to N. Otherwise, truncation error cannot be considered negligible. A common threshold value of -40 dB for a normalized n-spectrum is often taken but can be smaller depending on the aimed measurement result accuracy.

Directivity

The simple expression for the radiated power also allows expressing the directivity defined in (I.1) using the spherical coefficients. It is given in [1] to be

$$D(\theta, \varphi) = \frac{\|\sum_{smn} Q_{smn} \mathbf{K}_{smn}(\theta, \varphi)\|^2}{\sum_{smn} |Q_{smn}|^2} \tag{II.18}$$

where $\mathbf{K}_{smn}$ are the far-field pattern functions. They are asymptotic expressions of the SW and are defined as

$$\mathbf{K}_{smn}(\theta, \varphi) = \lim_{r \to \infty} \sqrt{4\pi} \frac{kr}{e^{jkr}} \mathbf{F}_{smn}^{(3)}(r, \theta, \varphi). \tag{II.19}$$

II.3 Spherical coefficients identification

The antenna characterization using the SW expansion implies the identification of the spherical coefficients Q_{smn}. From these coefficients, the field radiated by the DUT can be reconstructed outside the minimal sphere enclosing all sources, i.e. S in Fig. II.6. For a truncation order N of the SW expansion defined as in (II.15), the number of spherical coefficients to determine is

$$N_c = 2N(N + 2). \tag{II.20}$$

The method to determine these N_c spherical coefficients depends both on the number of field samples and the sampling strategy. A distinction between a spherical near field and a far field configuration must also be made.

II.3.a Spherical field measurement configuration

In the far field, the measured quantity is the electric field radiated by the AUT, hence the measured data can be directly plugged into the SW expansion (II.14). In the near field, the radiation pattern of the probe has to be compensated, leading to the use of the transmission formula instead. More details can be found at p. 62 and following in [1].

Most of the measurements shown in this work have been performed in the far field. The only near-field cases are coming from either simulations or measurements carried out using the MVG Starlab [4]. In the case of electromagnetic full wave simulation, the value of the field is provided everywhere without having to resort to any probe compensation. In the case of the measurements done with the Starlab, the probe compensation is already included in the MVG software. Consequently, the spherical wave expansion formula (II.12) is the only one used in this manuscript.

II.3.b Analytical method: Nyquist sampling rate

The analytical method to identify the SW coefficients [1] is performed by projecting the measured or discretized field into SW by exact derivation of some integrals under the hypothesis of a (spatial) bandwidth limited signal. These computations rely on a Fourier transform approach and a generalization of the Nyquist sampling theorem to the SW. The sampling scheme requires a constant step in both angular coordinates θ, φ, such a sampling is often called equiangular and an example is illustrated in Fig. II.7a. It is worth pointing out the oversampling at the pole of this technique.

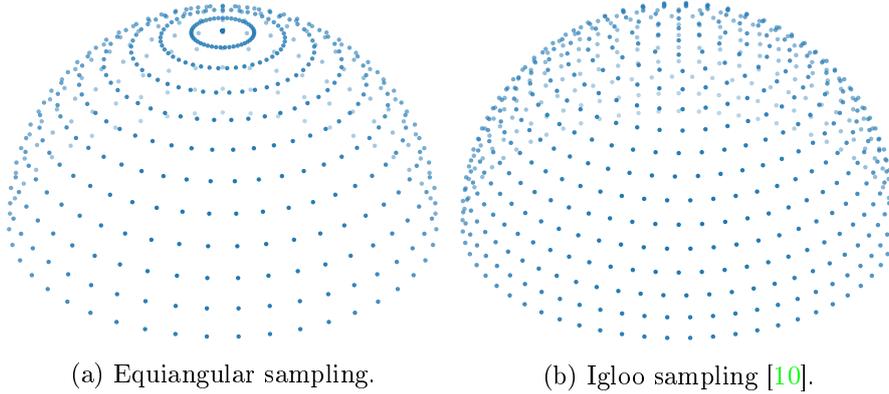(a) Equiangular sampling.   (b) Igloo sampling [10].

Figure II.7: Two different spherical sampling strategies over the hemisphere.

The identification of the spherical coefficients using this technique is exact, computationally efficient and scales well to high truncation orders [3]. However, this method requires a high amount of field samples [1], which is, for an equal step in both angles θ, φ, given by

$$M_H = 2(2N+1)(N+1) \tag{II.21}$$

where N is the truncation order of the SW expansion given by (II.15). For a DUT of diameter 10λ, the truncation order is $N = 41$ and $M_H = 6972$. Note that the factor two in front stands for the two polarizations of the field.

II.3.c Numerical method: approximated expansion

The angular directions are discretized when performing the measurement, the electric field is measured in two orthogonal/tangential directions at P positions over a sphere of radius R denoted by (θ_p, φ_p) for $p = 1, ..., P$. The SW expansion (II.14) can then be rewritten as a linear system of equation, whose matrix-vector formulation is

$$\mathbf{y} = \mathbf{A}\mathbf{x} \tag{II.22}$$

where the various indexes (s, m, n) of the SW must be ordered.

We define in this regard

$$
\mathbf{y} = \begin{bmatrix} E_\theta(\theta_1, \varphi_1) \\ \vdots \\ E_\theta(\theta_p, \varphi_p) \\ E_\varphi(\theta_1, \varphi_1) \\ \vdots \\ E_\varphi(\theta_p, \varphi_p) \end{bmatrix}, \ \mathbf{x} = \begin{bmatrix} Q_1 \\ Q_2 \end{bmatrix}, Q_s = \begin{bmatrix} Q_{s,-1,1} \\ Q_{s,0,1} \\ Q_{s,1,1} \\ Q_{s,-2,2} \\ Q_{s,-1,2} \\ \vdots \\ Q_{s,N,N} \end{bmatrix} \tag{II.23}
$$

$$
\mathbf{A} = \frac{k}{\sqrt{\upsilon}} \begin{bmatrix} \mathbf{F}_{\theta,1mn} & \mathbf{F}_{\varphi,1mn} \\ \mathbf{F}_{\theta,2mn} & \mathbf{F}_{\varphi,2mn} \end{bmatrix}. \tag{II.24}
$$

where $\mathbf{F}_{\theta,1mn}, \mathbf{F}_{\varphi,1mn}$ denotes the $\hat{\theta}, \hat{\varphi}$ component of $\mathbf{F}_{1mn}$, respectively.

This matrix formulation allows using standard linear system inversion procedures to identify the spherical coefficients $\mathbf{x}$ from the known measured field $\mathbf{y}$. The least square problem or regularized least square using Singular Value Decomposition (SVD) approaches are two examples. Most of these matrix inversion procedures requires at least as much data as unknowns to work properly. It means that the number of measured field samples (length of $\mathbf{y}$) should be equal to or greater than the number of unknown SW coefficients (length of $\mathbf{x}$), N_c in (II.20). These standard matrix inversion approaches provide admittedly an approximated solution but they only require about half of the measurement samples as compared to the analytical approach: $M_{LS} \approx M_H/2$.

In addition, the matrix formulation allows using any spherical sampling strategy. At IETR, the use of the igloo sampling [10], shown in Fig. II.7b, allows to avoid the over-sampling near the poles induced by the equiangular sampling while enabling fast spherical scans with a constant elevation θ step and and constant azimuthal φ step at a given elevation.

As a summary, the matrix approach has the following advantages

- Enables a flexible sampling scheme.

- Reduces the number of sampling points as compared to the analytical approach.

Conversely, the drawbacks are

- Approximated solutions.

- Numerical stability has to be assessed.

- Computationally more demanding.

II.4   Sparse recovery of the spherical coefficients

Any under-determined linear system of equations, one having more unknowns than ob-servations/data, has an infinite number of solutions. Under the assumption that the true solution is sparse, i.e. it contains a lot of zeroes, we are able to determine a solution vector among the infinity of them [11, 13, 16]. The fields emitted by any DUT present symmet-ries and smoothness, reducing their inner complexity. A small number of SW coefficients

suffices to describe the radiated field with respect to their total number N_c in (II.20). Consequently, the spherical coefficients form a sparse vector and sparse recovery techniques can be used to identify or approximate it, as already shown in [8–10]

II.4.a   Norms and sparsity

Let us introduce different norms that will be later used to describe the sparse recovery and different optimization methods.

The ℓ_p norm, $p \geq 1$, of a complex vector $\mathbf{x}$ of size M reads [17]

$$\|\mathbf{x}\|_p = \left(\sum_{i=1}^{M} |x_i|^p\right)^{1/p} \tag{II.25}$$

This definition can be extended to the case $p = \infty$. The ℓ_∞ or ∞-norm of $\mathbf{x}$ is the maximum modulus component. For $0 < p < 1$, the ℓ_p function is no longer a norm but can still be computed from (II.25). We can also define the ℓ_0 "norm", which is the number of non-zero components of $\mathbf{x}$. The ℓ_0 norm is the true measure of the sparsity. The unit balls for some ℓ_p norms are illustrated in Fig. II.8.
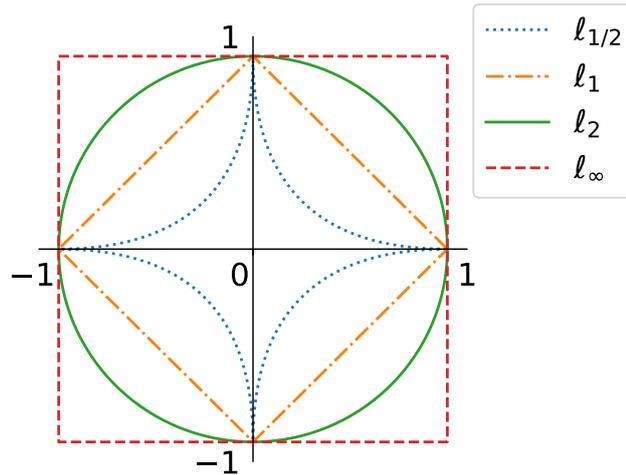

Figure II.8: Unit balls (the set of vectors having unity norm) for ℓ_p, $p = 1/2, 1, 2$ and ∞.

II.4.b   From ℓ_0 to ℓ_1 minimization

The solution $\mathbf{x}$ of $\mathbf{Ax} = \mathbf{y}$ is assumed to be sparse, the sparsity of $\mathbf{x}$ is given by its ℓ_0 norm, namely $\|\mathbf{x}\|_0$. Since an under-determined system has an infinity of solutions, our choice is to search for the sparsest one, which translates into the following optimization problem, called ℓ_0-minimization [11]

$$\min_{\mathbf{x}} \|\mathbf{x}\|_0 \text{ subject to } \mathbf{Ax} = \mathbf{y}. \tag{II.26}$$

Unfortunately, this problem is NP-hard [11, 16], meaning that reaching a solution requires an intractable computation time even for small size problems. Various classes of algorithms

have been proposed to solve this sparse recovery problem, that is encountered in many applications.

Greedy algorithms

This class of algorithms focuses on the regularization term $\|\mathbf{x}\|_0$. Components of $\mathbf{x}$ are added sequentially till the equality constraint $\mathbf{Ax} = \mathbf{y}$ is satisfied. The greatest example of this class is the Matching Pursuit [18]. Before adding another component, the algorithm check if the previously chosen ones can be updated to better fit the equality, hence the name. However it might get stuck in a loop depending on the updates. The orthogonal version of this algorithm, the Orthogonal Matching Pursuit (OMP) [19], corrects this problem but induces costly computational tasks. The greedy algorithms are mostly variants of the OMP (StOMP, ROMP, ...).

Thresholding algorithms

The family of thresholding techniques rather focuses on the equality constraint $\mathbf{Ax} = \mathbf{y}$. This residual error $\|\mathbf{y} - \mathbf{Ax}\|_2$ is minimized iteratively, and the sparsity is ensured by thresholding the coefficients of the estimated solution. Among the many algorithms of this class, we can cite the Iterative Hard Thresholding [20]. It simply puts to zero the negligible coefficients between each iteration while trying to minimize the residual error. However the returned solution might be non-satisfactory even if the correct non-zero components have been identified. Again, there are several variants based on this approach for mitigating these drawbacks, for example the Hard Thresholding Pursuit [16].

Convex relaxation

The complexity of the ℓ_0-minimization and the various numerical problem it induces are due to the non-convexity of the ℓ_0 norm. However, the optimization problem (II.26) can be turned into a convex optimization problem that is much easier to solve by replacing the ℓ_0 norm by the ℓ_1 one. This operation is called convex relaxation. Instead of the ℓ_0-minimization problem problem, one rather solves the convex, ℓ_1, one, named Basis Pursuit (BP) [11] and defined as

$$\min_{\mathbf{x}} \|\mathbf{x}\|_1 \text{ subject to } \mathbf{Ax} = \mathbf{y}. \tag{II.27}$$

The name Basis Pursuit comes from the process in finding the solution of this problem, which is about selecting columns of $\mathbf{A}$ to form an invertible submatrix that can be used to solve the equality constraint. It has been proven in [21] that the solution to the ℓ_1-minimization problem (II.27) is equal to the ℓ_0 one if the sparse vector $\mathbf{x}$ to be recovered is sparse enough. Indeed, the ℓ_1 norm also provides sparse solutions [11,16], as illustrated in Fig. II.9.

For a 2D example, the solutions for ℓ_1 and ℓ_2 minimizations are the intersections of the scaled unit balls and the plain straight line that represents the solution of $\mathbf{Ax} = \mathbf{y}$. The minimal ℓ_1 solution line will likely hit a corner of the scaled corresponding norm ball, leading to one coordinate being 0. On the contrary, the ℓ_2 norm does not have a preferred direction and hence does not possess such sparsity feature, both coordinates of the minimal ℓ_2 solution are non-zero.
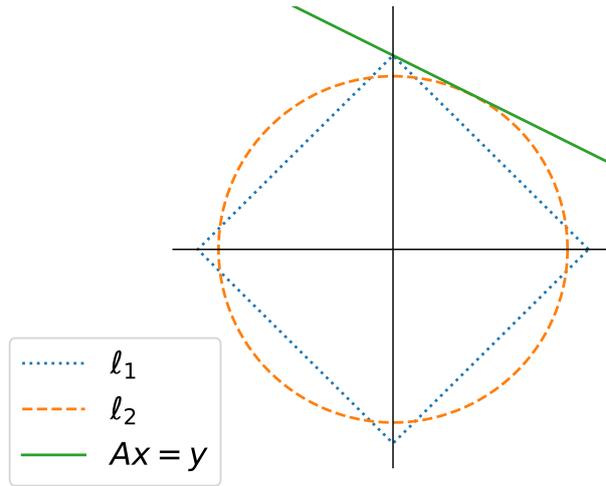
Figure II.9: Geometrical visualization of the sparsity induced by ℓ_1 minimization for a linear system $\mathbf{Ax} = \mathbf{y}$.

II.4.c Basis Pursuit DeNoising (BPDN)

The use of ℓ_1-minimization for sparse recovery has been motivated, leading to the formulation of a convex optimization problem (II.27). However, real world measurements are noisy and the equality constraint $\mathbf{Ax} = \mathbf{y}$ is not suitable for such data. This can be accounted by replacing this equality constraint by an inequality with an user-defined upper bound, leading to the following problem [11]

$$\min_{\mathbf{x}} \|\mathbf{x}\|_1 \text{ subject to } \|\mathbf{Ax} - \mathbf{y}\|_2 \leq \sigma \tag{II.28}$$

where $\sigma \geq 0$ is the error tolerance parameter. This problem is known as Basis Pursuit DeNoising (BPDN). The name comes from the same reasons as the Basis Pursuit in (II.27) and the denoising is due to the inequality constraint, which mitigates the effects of noise over the minimization process. The BPDN is solved in this work using the fast and efficient SPGL1 algorithm [22, 23], which stands for Spectral Projected Gradient for ℓ_1-minimization. The solution to the BPDN problem (II.28) is approximated by iterative resolutions of LASSO problems (Least Absolute Shrinkage Selection Operator), which are also called ℓ_1-regularization problems and are defined in [16] as

$$\min_{\mathbf{x}} \|\mathbf{Ax} - \mathbf{y}\|_2 + \lambda \|\mathbf{x}\|_1 \tag{II.29}$$

where λ is the regularization parameter. These problems are easier to solve, the SPGL1 algorithm iterates over the parameter λ till the returned solution also satisfies the BPDN for the chosen error tolerance σ.

Application to the characterization of a horn at 30 GHz

The field reconstruction using sparse recovery technique of a pyramidal horn simulated in HFSS is demonstrated. The antenna has a minimal sphere of radius $a = 3$ cm, and consequently a truncation order of $N = 28$ which implies $N_c = 1680$ spherical coefficients

at 30 GHz. The standard analytical method requires $M_H = 3306$ field samples in this case. Two *igloo* samplings of different sizes and linear system resolution methods are considered for the characterization.

The first one has $M_{TSVD} = 2245$ data, and the spherical coefficients are identified using the Truncated Singular Value Decomposition (TSVD) [24], a classical method for over-determined systems closely related to least-square solutions. The second one emulates a fast measurement procedure with only $M_{BPDN} = 630$ measured field samples and spherical coefficients are found by solving the BPDN problem.

The reconstructed fields from both coefficient identification strategies are compared to the simulation by displaying their magnitudes in Fig. II.10 following the Ludwig-3 definitions of co- and cross-polarizations [25]. The far-field radiated by the horn is accurately reconstructed down to very low magnitude levels in both cases despite the lower number of samples, even for the fast testing sampling. Thus, a significant reduction of the number of field samples is achieved while preserving the accuracy of the field reconstruction. We have $M_{TSVD} = 0.68M_H$ and $M_{BPDN} = 0.2M_H$. In other words, the number of field samples used for the sparse recovery approach is five times smaller than the one advocated by the generalized Nyquist sampling rate technique.
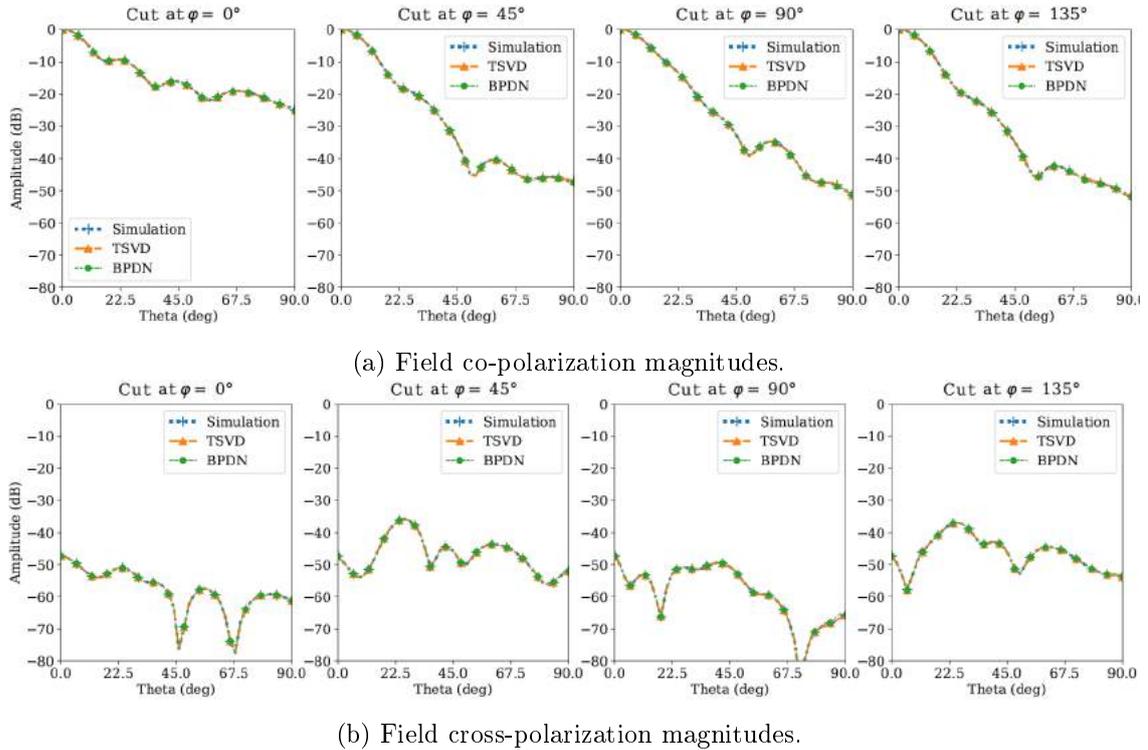

(a) Field co-polarization magnitudes.

(b) Field cross-polarization magnitudes.

Figure II.10: Simulated and reconstructed field magnitudes over some cutting planes on the co-polarization and cross-polarization components.

II.4.d   The error tolerance parameter

The error tolerance parameter σ in (II.28) has to be properly set, as it greatly influences the solution of the sparse recovery problem. Its determination is a well known problem in convex optimization theory, it is discussed in this section in the context of fast antenna measurements.

Criterion for ℓ_2 regularization

The ℓ_2 regularization, also known as Tikhonov regularization, problem [26] is formulated

$$\min_{\mathbf{x}} \|\mathbf{Ax} - \mathbf{y}\|_2^2 + \lambda \|\mathbf{x}\|_2^2 \qquad \text{(II.30)}$$

where $\lambda > 0$ is the regularization parameter, playing a similar role as σ in (II.28). This parameter controls the data fitting, i.e. the trust given in the data. This well known problem has been largely investigated for a wide range of applications. Without regularization ($\lambda = 0$), it boils down to solve the standard least square problem. As the regularization parameter λ increases, the solution of the least square problem is more and more forced to exhibit the smallest possible energy, $\|\mathbf{x}\|_2$.

The curve defined by $\lambda \mapsto (\|\mathbf{Ax} - \mathbf{y}\|_2, \|\mathbf{x}\|_2)$ presents typically a L-shape in ℓ_2 regularization contexts, as displayed in Fig. II.11a. It has been shown that the most relevant choice of λ without further assumptions is given by the value corresponding to the corner of this curve [27]. We illustrate this criterion with an example in Fig. II.11 and II.12. The quantity $\mathbf{x}_\lambda$ denotes the solution of the ℓ_2 regularization problem (II.30) for λ as the regularization parameter. A true signal $\mathbf{y}_0$, displayed in Fig. II.12 is reconstructed using 21 noisy data points, which is modelled by Gaussian white noise, for a Discrete Cosinus Transform (DCT) matrix with 101 coefficients, or unknowns.

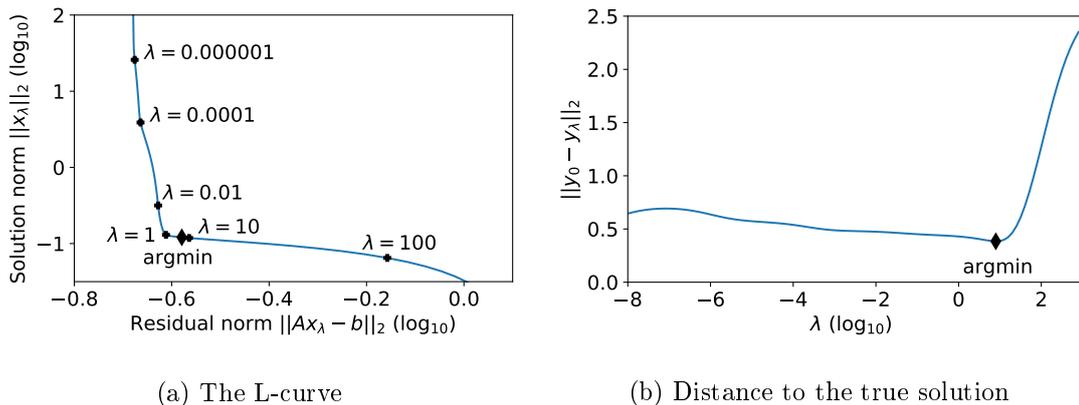(a) The L-curve   (b) Distance to the true solution

Figure II.11: (a) Typical L-curve observed for Tikhonov regularization, (b) reconstruction metric with respect to the true signal. The criterion recommends the penalty term value $\lambda \approx 1$.

The corner of the curve is the best compromise between minimizing the residual error, i.e. solving at best the linear system, and minimizing the norm of the solution, understood as a measure of its complexity. If we go past the corner on the horizontal part of the curve, the residual error is increased without impacting the complexity of the solution. Conversely, if we go up the vertical part, we do little improvements over the residual errors at the cost of significantly more complex/larger norm solutions, indicating that we are probably trying to fit some noisy contributions instead of the desired signal.

Extension to ℓ_1 minimization

The error tolerance parameter σ in (II.28) plays the same role as the regularization parameter λ in the ℓ_2 regularization (II.30), as demonstrated in [28], or in the LASSO problem
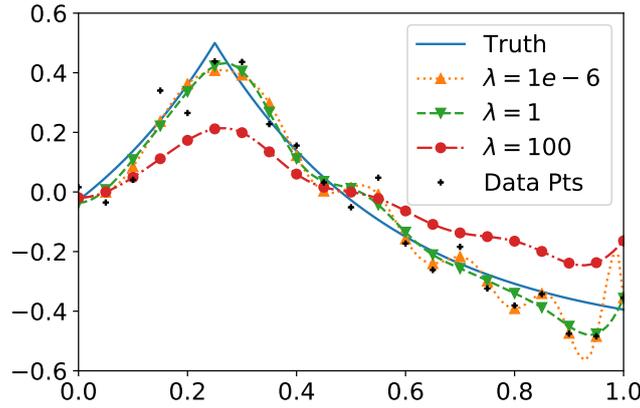
Figure II.12: Illustration of the reconstructed signals using noisy data sample for several penalty terms λ. The choice $\lambda = 1 \times 10^{-6}$ leads to an under-regularization (oscillations), $\lambda = 1$ is the penalty term given by the criterion and $\lambda = 100$ induces an over-regularization (also known as dampening).

(II.29). For this reason, we propose to use the L-curve approach previously described in order to find the best error tolerance parameter value σ.

The curve defined by $\sigma \mapsto (\|\mathbf{Ax} - \mathbf{y}\|_2, \|\mathbf{x}\|_1)$, similar to the definition of the L-curve for ℓ_2 regularization, also presents a L shape, as illustrated in the examples Fig. II.14a and II.15a. However, it is notably smoother. This has been discussed in [22] and the corner criterion has also been tested in ℓ_1 minimization context, e.g. for tomography in [29]. The same explanation as previously discussed remains true, the corner is the best trade-off between the sparsity of the solution and the residual error.

The corner of the L-curve can be identified accurately by computing its curvature κ. It is mathematically defined at any point of a smooth curve as the inverse radius of the circle approximating at best this curve around the considered point, also known as the osculating circle. The curvature of the curve in Fig. II.13 at the point P is $1/R$. Consequently, we recommend to use the value σ that corresponds to the maximum curvature of the curve $\sigma \mapsto (\|\mathbf{Ax} - \mathbf{y}\|_2, \lambda\|\mathbf{x}\|_1)$.
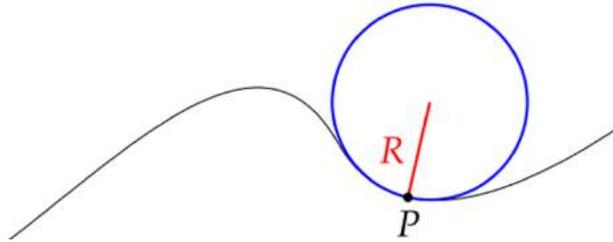

Figure II.13: The curvature of the curve at the point P is given by the inverse of the radius R of the best approximating circle of the curve at that point.

Search algorithm for the error tolerance parameter

The curvature κ of a plane curve quantifies how much the curve changes its direction locally. Hence the corner of the L-curve corresponds to the maximum of the curvature.

Unfortunately, the computation of the L-curve is time consuming. A search algorithm has been developed in [30] for ℓ_2-regularization for the automatic and efficient identification of the curve corner using Menger curvature estimation. This algorithm has been adapted to our problematic. It is provided in the Appendix B, Algorithm 2.

However, the Menger estimation of the curvature has been observed to provide noisy results in our context. Another estimation technique of the curvature, called the parabola method [31] has been implemented to overcome this problem. The input of the algorithm is an interval to search in, which is provided by a first estimation of the error tolerance parameter $\widetilde{\sigma} = \sqrt{M}\|\mathbf{y}\|_\infty 10^{-T/20}$ with M the size of $\mathbf{y}$, the number of measurement data, and T the estimated noise-floor over the measurement data in dB. This estimation comes from a simple upper bound of the residual error under the assumption that every sampling point data is true down to $-T$ dB. Then it suffices to consider the following interval $\left[\frac{\widetilde{\sigma}}{10}, 10\widetilde{\sigma}\right]$. The output of the search algorithm is noted σ_κ in the sequel.

Application to fast antenna measurements

Let us consider the measurement of a reflectarray at 12 GHz in order to assess our procedure to choose the error tolerance criterion. The DUT has a minimal sphere of radius 12 cm, leading to a truncation order $N = 42$ of the SW series, or equivalently $N_c = 4606$ spherical coefficients to identify. A fast measurement is achieved by considering a sample of size $M = 3112$ along an *igloo* sampling. This small dataset is used to identify the N_c coefficients to interpolate the field over a dense measurement sampling to compare with the reference data. The accuracy of the reconstruction using the fast measurement sampling is assessed by computing the residual field and the ENL, defined in (I.3) and (I.5), respectively. As shown by the results in Fig. II.14, the best reconstruction metrics values corresponds to the corner of the curve, captured by the maximum curvature, which confirms the validity of the proposed strategy. In these figures, the grey area represents the zone where the error parameter σ should be chosen. This zone is precisely the one of the best field interpolations as shown by the values of the comparison metrics.
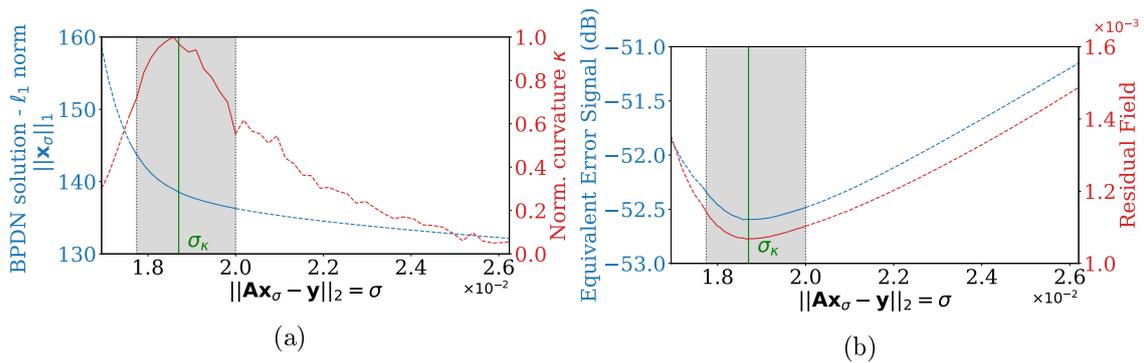

Figure II.14: Fast measurement of the reflectarray at 12 GHz: (a) L-curve in BPDN and its normalized curvature, (b) corresponding metrics values. The green line σ_κ is the value returned by the automatic research algorithm.

The choice of the error tolerance parameter has also been tested with the same methodology on a radiating cavity antenna at 6 GHz, which is a less directive antenna than the reflectarray and consequently provides a very different example. The results are displayed

in Fig. II.15. The σ choices leading to the best reconstruction metrics are located around the maximum curvature point. However, we can note that the criterion slightly overshoots the optimal choice here, which is often the case in ℓ_2 regularization as reported in [27].

For both cases, the maximum curvature search algorithm σ_κ has provided correct results, as shown in Fig. II.14b and II.15b.
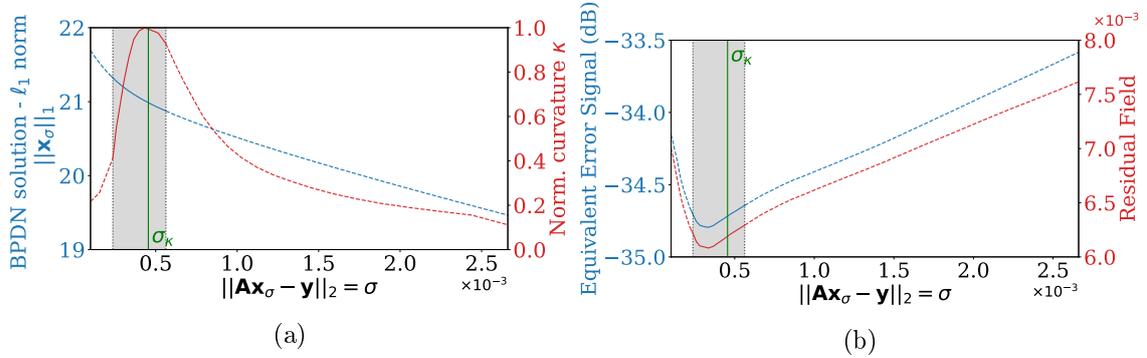

Figure II.15: Fast measurement of the radiating cavity antenna at 6 GHz: (a) L-curve in BPDN and its normalized curvature, (b) corresponding metrics values. The green line σ_κ is the value returned by the automatic research algorithm.

II.5   On the number of field samples

The sparse recovery of the spherical coefficients allows to significantly reduce the number of field samples as compared to standard approaches while ensuring a proper and accurate antenna characterization. We propose a methodology to derive the minimum number of samples to properly retrieve the sparse SW coefficients and therefore to enable a fast characterization of its radiation pattern.

II.5.a   Phase transition diagrams

The Phase Transition Diagrams (PTD) are a 2D graphic that display under which conditions an under-determined linear problem can be properly solved. These conditions are:

1. the sampling size, under the measurement ratio δ, the number of measurements over the number of unknown coefficients. It is the abscissa axis of the graphic.

2. the sparsity level ζ, the number of non-zero coefficients in the solution over the number of measurements. It is the ordinate axis.

For a fixed numerical solution, given its sparsity and the number of field samples, the PTD indicates whether the resolution might be successful or not. The typical aspect of a PTD is represented in Fig. II.16. Roughly speaking and as expected, the sparser the solution, the easier its recovery from a small number of samples. While this holds true in general, this global tendency is not enough to provide a minimum number of samples.

In the original paper [13], the PTD are analytically computed for Gaussian sensing matrices $\mathbf{A}$. However it can be generalized numerically to various sensing matrices. We extend the application of PTD to fast antenna measurements where the sensing matrices are built from SW.
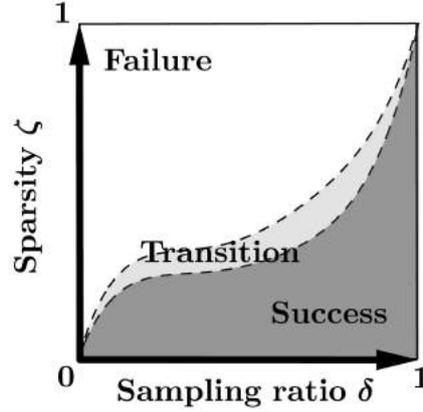
Figure II.16: Phase transition diagram sketch with its three regions: failure, transition and success of the solution identification as a function of its sparsity ζ (the number of non-zeros in the solution) and the sampling ratio δ (number of field samples over the total number of coefficients).

II.5.b   Application to antenna measurements

The first applications of PTD for antenna characterization can be found in [9, 10]. A detailed study using PTD is also provided in [14], from which Fig. II.4 comes from. Prof. Eibert *et al.* use a formulation that is closer to the original theory of [13], enabling a comparison with exact bounds, such as the Bounded Orthonormal System one [32]. The impact of the probe compensation for spherical near-field measurements is also taken into account, which increases the practical relevance of this work. The present manuscript adds on these interesting investigations by considering scenarios that are, we believe, more representative of antenna characterization problems.

The numerical derivation of a PTD can be done as follows. A spherical expansion coefficient set is drawn to generate field samples over given spherical samplings. These field samples are used as measurement data and the BPDN is solved to retrieve the coefficients. Finally, the retrieved solution is compared to the exact one to assess the success or failure of the procedure. This process must be repeated enough times to provide a relevant and reliable estimation of the probability of successful recovery. This computation has to be done for various couples of measurement ratios and sparsity levels (δ, ζ) so as to be able to display a 2D PTD graphic. A number of 200 SW coefficient sets have been generated for each tested couple in the present work.

The random drawing of the SW expansion coefficients can be done in various ways, the same parameters in the Gaussian law were considered for drawing the coefficients across the whole spectrum. However, the truncation order has to be set so that the radiated power by the SW having degree $n \approx N$ is negligible. This verification is performed by the N-test. It means that a realistic SW coefficient magnitude set should be significantly smaller for the degrees n close to the truncation order N. This can be ensured by a proper decrease of the variance parameter of the Gaussian law, forcing the magnitude of the coefficients to decrease as expected.

Moreover, real measurement data are noisy. Therefore a relevant measure of sparsity is rather provided by the proportion of significant coefficients instead of non-zero ones. If a coefficient has a negligible magnitude with respect to other ones and to the expected measurement accuracy, its identification is not relevant. Consequently, we introduce the

effective sparsity to count how many coefficients we can expect to retrieve in practice. The effective sparsity ζ_T with threshold T is defined as follows

$$\zeta_T = \frac{1}{N_c} \# \left\{ \frac{|x_i|}{\|\mathbf{x}\|_\infty} > 10^{T/20}, i = 1, \dots, N_C \right\} \tag{II.31}$$

where N_c is the total number of coefficients, $\#$ is the cardinal operator and T the threshold separating significant and negligible coefficient magnitudes. If a value of $T = -40$ dB is chosen in practice, the radiated field generated by truncating lower magnitude coefficients is close up to -50 dB in ENL in (I.5) to the original one.

Furthermore, the goal of the fast measurement procedures is to reconstruct the radiation pattern. It is therefore the true figure of merit that distinguishes a successful from a failed recovery. The success of the fast characterization procedure is thus tested on the radiation patterns rather than the spherical coefficients. We have used the ENL metric to this end, comparing the reference field generated by the randomly drawn coefficients and the field reconstructed from the coefficients found by the BPDN and the reduced number of samples. The criterion for successful recovery is that the ENL between the reference and the reconstructed pattern must be lower than -50 dB, corresponding to choice of the effective sparsity T_{-40}.

Finally, the influence of the sampling over the sparse recovery performance can be significant and studies have been led to derive a sampling strategy that minimizes the cross-correlation of the sensing matrix and therefore enlarges the "success" region in the PTD [12]. During this work, we have chosen to limit ourselves to the *igloo* sampling and the spiral sampling, both illustrated in Fig. II.17. The *igloo* sampling is the one used at IETR, for reasons previously discussed, and the spiral one is one of the best approximation of a uniform sampling on the sphere, providing a reference test. This sampling has also been treated in [14].
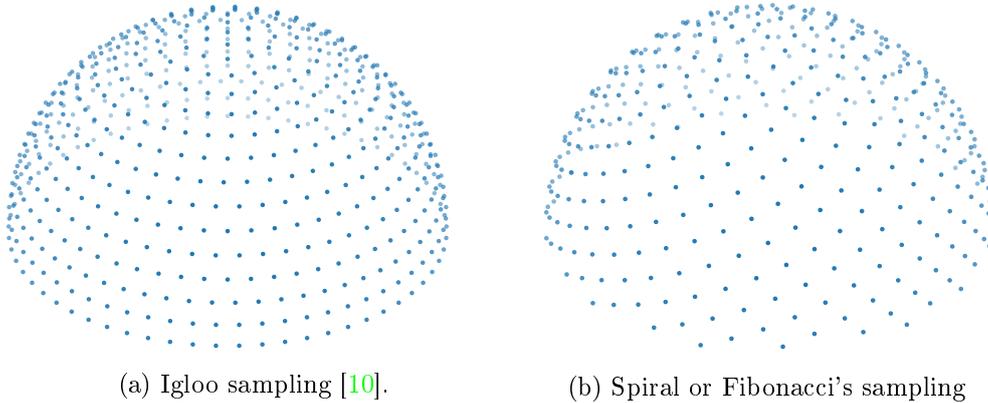

(a) Igloo sampling [10].   (b) Spiral or Fibonacci's sampling

Figure II.17: Two different spherical sampling strategies tested using PTD over the hemisphere.

The results for the criterion success ENL < -50 dB and using two sampling strategies for the fast measurement samplings, *igloo* and spiral, are shown in Fig. II.18. According to these results, a measurement ratio $\delta = 75$ % is enough to properly characterize any antenna for a truncation order $N = 40$. Indeed, this ratio leads to successful field reconstruction in all cases for this truncation order. Further studies have been carried out to show that this ratio is stable with respect to the truncation order N of the SW expansion, as suggested

by Fig. II.19. This figure can be seen as a cutting plane of the PTD for $\zeta_{-40} = 40$ %.
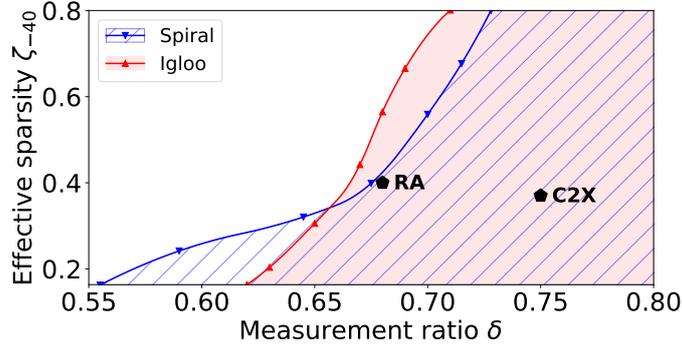

Figure II.18: Obtained transition diagram, probability evaluated from 200 trials. Dashed or coloured regions mean 100 % successful reconstruction for the criterion success being EES < -50 dB for a truncation order $N = 40$ of the SW. The markers denotes two measurements presented in Section II.4.d.
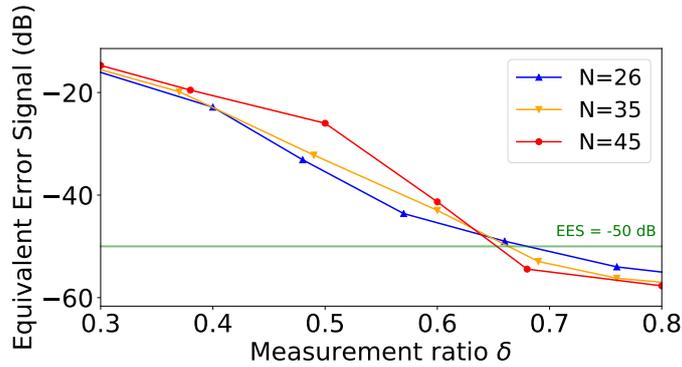

Figure II.19: ENL (average value over 200 trials) using an *igloo* sampling for several SW series truncation order N and an effective sparsity of $\zeta_{-40} = 0.4$.

As a conclusion and according to our results, for a given antenna having truncation order N, the total number of coefficients to determine is $N_c = 2N(N+2)$ and the measurement data set has to be as least at $0.75N_c$ to ensure a successful antenna characterization for our chosen success criterion and sampling strategy.

II.5.c   Fast antenna measurements at IETR

The IETR spherical measurement systems have been described and illustrated in Section I.2.c. They consist in roll-over-azimuth positioning systems with sequential engine motions using a step by step field acquisition. Details about the measurement procedure, i.e. how the system is going through the sampling is also given in Section I.2.c, and the estimation of the duration of the field acquisition is detailed in Appendix A.

For a given DUT, we can deduce the number N_c of SW involved in the expansion of its radiated field from its electrical size. According to the PTD computed for SW matrices and realistic data in the context of antenna measurements, we conclude that a fast measurement with sparse recovery technique and SW function basis requires only 75% of the number of

expansion coefficients N_c as field sampling size. The number of samples if thus given by

$$M_{BPDN} \approx \frac{3}{2} N(N+2) \tag{II.32}$$

where N in (II.15) is given by the electrical length of the DUT. The sparse recovery technique allows using only a field sampling size of 37 % of the analytical, Nyquist sample rate, approach for which of the number of samples was $M_H = 2(2N+1)(N+1)$.

Combining this statement with the estimated field acquisition duration at IETR, the time savings induced by the fast measurement method with respect to the standard method in our measurement facilities can be deduced and are plotted in Fig. II.20.
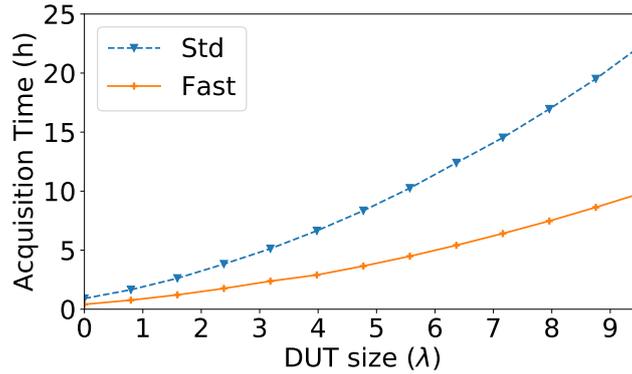

Figure II.20: Estimated field acquisition duration at IETR as a function of the DUT maximal size in wavelength λ. Std stands for the standard spherical measurement method based on the Nyquist sampling rate [1] and Fast for the sparse recovery method, using an *igloo* sampling and with a 75 % measurement ratio.

Application to the measurement of a Pillbox antenna at 270 GHz

The DUT is a square of 24 mm made of copper with radiating slots designed by KTH and IETR [33]. This antenna has been measured at 270 GHz at IETR using a fast measurement sampling over a hemisphere. The considered minimal sphere has a radius of 14 mm and consequently a truncation order of $N = 120$ is considered. Since the measurement is only performed over the hemisphere, only even SW can be used in the expansion, $\mathbf{F}_{smn}$ such that $m+n$ is even, by assuming a symmetric radiation pattern with respect to the equator, leading to $N_c = 29280$ coefficients. The fast measurement sampling has 21834 field samples, or a measurement ratio of ≈ 75 %, as advocated by the PTD results. The analytical approach would have required $M_H = 2(2N+1)(N+2) = 58322$ field samples in comparison. The reference for reconstruction assessment is provided by dense measurements over the cutting planes $\phi = 0°$ and $45°$.

The 3D reconstruction of the field using the fast measurement procedure, i.e. *igloo* sampling and ℓ_1 minimization by BPDN, is given in Fig. II.21 and the comparison to the reference over the cutting planes in Fig. II.22. An excellent agreement between the reconstructed and densely measured field over the cutting planes is achieved despite the significant reduction in the number of samples. The proposed fast antenna characterization approach has allowed to bring down the field acquisition duration from 62 to 26 hours.
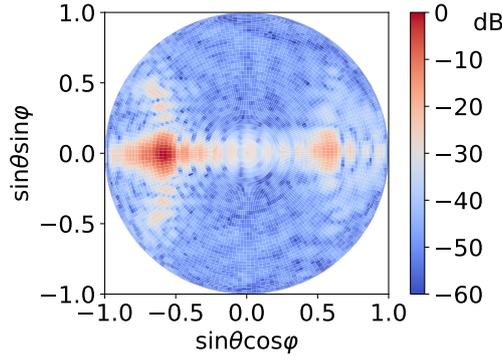
Figure II.21: Normalized magnitude of the 3D reconstructed radiated field of the pillbox antenna at 270 GHz.

(a) $\varphi = 0°$ (b) $\varphi = 45°$
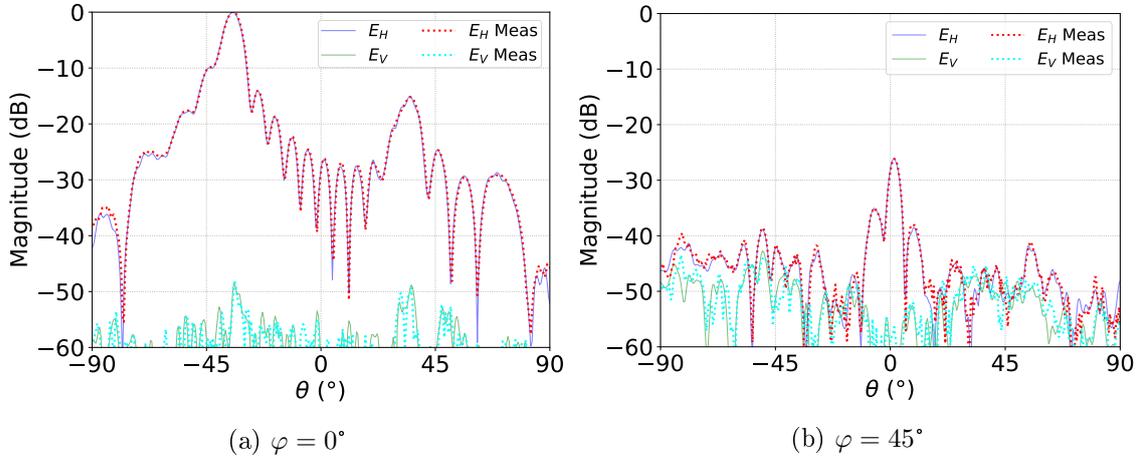
Figure II.22: Normalized magnitudes of the radiated fields from the pillbox antenna at 270 GHz, comparison of the reconstructed field and the reference measurement (dense measure) (a) over the main cutting plane and (b) another one containing a lot of minimums.

II.6   Conclusion

The SW expansion of radiated fields and the fast antenna measurement technique using sparse recovery have been introduced and detailed. The proposed fast antenna pattern characterization approach requires the choice of an error tolerance parameter and the number of samples to be measured. An automatized procedure has been developed to apply the sparse recovery of the SW expansion of radiated fields. More specifically, a search algorithm has been proposed to properly set the data fitting term whereas existing tools have been adapted to derive the general minimal number of samples. This fast measurement procedure reduces the field acquisition duration by a factor around 2 as compared to the standard technique based on the Nyquist sampling rate in the IETR measurement facilities.

Besides, it is possible to further enhance the sparsity of the measured antenna spectrum and consequently improve the reconstruction of its radiation pattern from a given number of field samples. To this end, the optimization of the antenna positioning is addressed in the next chapter as a mean to improve, by post-processing, the accuracy of the antenna pattern measurement.

Bibliography

[1] J. Hald, J.E. Hansen, F. Jensen, and F.H. Larsen. *Spherical Near Field Antenna Measurements*. Peter Peregrinus, 1988.

[2] IEEE recommended practice for near-field antenna measurements. *IEEE Std 1720-2012*, pages 1–102, 2012.

[3] O. Breinbjerg. Spherical near-field antenna measurements — the most accurate antenna measurement technique. In *2016 IEEE International Symposium on Antennas and Propagation (APSURSI)*, pages 1019–1020, 2016.

[4] Starlab 650MHz-18GHz. MVG, 2020. Available at https://www.mvg-world.com/fr/products/antenna-measurement/multi-probe-systems/starlab.

[5] O. M. Bucci, C. Gennarelli, and C. Savarese. Representation of electromagnetic fields over arbitrary surfaces by a finite and nonredundant number of samples. *IEEE Trans. on Antennas and Propag.*, 46(3):351–359, March 1998.

[6] M. D. Migliore. On electromagnetics and information theory. *IEEE Trans. on Antennas and Propag.*, 56(10):3188–3200, Oct 2008.

[7] F. Jensen and A. Frandsen. On the number of modes in spherical wave expansions. In *AMTA 2004*, 10.

[8] D. Loschenbrand and C. Mecklenbrauker. Fast antenna characterization via a sparse spherical multipole expansion. Aachen, 2016. 4th International Workshop on Compressed Sensing Theory and its Applications to Radar, Sonar and Remote.

[9] R. Cornelius, D. Heberling, N. Koep, A. Behboodi, and R. Mathar. Compressed sensing applied to spherical near-field to far-field transformation. pages 1–4, Davos, 2016. Eur. Conf. Antennas Propag. (EuCAP).

[10] B. Fuchs, L. Le Coq, S. Rondineau, and M.D. Migliore. Fast antenna far field characterization via sparse spherical harmonic expansion. *IEEE Trans. on Antennas and Propag.*, 65(10):5503–5510, Oct. 2017.

[11] M. Elad. *Sparse and Redundant Representations - From Theory to Applications in Signal and Image Processing*. Springer, 2010.

[12] C. Culotta-Lopez, D. Heberling, A. Bangun, A. Behboodi, and R. Mathar. A compressed sampling for spherical near-field measurements. In *AMTA 2018*, Williamsburg Virginia, USA, November 2018.

[13] D. L. Donoho and J. Tanner. Precise undersampling theorems. *Proceedings of the IEEE*, 98(6):913–924, June 2010.

[14] B. Hofmann, O. Neitz, and T. Eibert. On the minimum number of samples for sparse recovery in spherical antenna near-field measurements. *IEEE Trans. on Antennas and Propag.*, 67(12):7597–7610, 2019.

[15] E.L. Hill. The Theory of Vector Spherical Harmonics. *American Journal of Physics*, 22:211–214, April 1954.

[16] S. Foucart and H. Rauhut. *A Mathematical Introduction to Compressive Sensing.* Birkhauser, 2013.

[17] S. Boyd and L. Vandenberghe. *Convex Optimization.* Cambridge University Press, New York, NY, USA, 2004.

[18] S. G. Mallat and Z. Zhang. Matching pursuits with time-frequency dictionaries. *IEEE Transactions on Signal Processing*, 41(12):3397–3415, Dec 1993.

[19] G. Davis, S. Mallat, and Z. Zhang. *Adaptive Time-Frequency Approximations with Matching Pursuits*, volume 5. Elsevier B.V., 1994.

[20] T. Blumensath and M. E. Davies. Iterative hard thresholding for compressed sensing. *CoRR*, abs/0805.0510, 2008.

[21] David L. Donoho and Michael Elad. Optimally sparse representation in general (nonorthogonal) dictionaries via l1 minimization. *Proceedings of the National Academy of Sciences*, 100(5):2197–2202, 2003.

[22] E. van den Berg and M. P. Friedlander. Probing the pareto frontier for basis pursuit solutions. *SIAM Journal on Scientific Computing*, 31(2):890–912, 2008.

[23] E. van den Berg and M. P. Friedlander. SPGL1: A solver for large-scale sparse reconstruction, June 2007.

[24] G. H. Golub and C. F. Van Loan. *Matrix Computations.* The Johns Hopkins University Press, third edition, 1996.

[25] A. C. Ludwig. The definition of cross polarization. *IEEE Trans. on Antennas and Propag.*, AP-21:116 – 119, 02 1973.

[26] A. Tikhonov. On the stability of inverse problems. *Proceedings of the USSR Academy of Sciences*, 39:195–198, 1943.

[27] P. C. Hansen. The L-curve and its use in the numerical treatment of inverse problems. In *Computational Inverse Problems in Electrocardiology*. WIT Press, 2000.

[28] J.J. Fuchs. Recovery of exact sparse representations in the presence of bounded noise. *IEEE Transactions on Information Theory*, 51(10):3601–3608, 2005.

[29] J. Nasehi Tehrani, A. McEwan, C. Jin, and A. van Schaik. L1 regularization method in electrical impedance tomography by using the l1-curve (pareto frontier curve). *Applied Mathematical Modelling*, 36(3):1095 – 1105, 2012.

[30] A. Cultrera and L. Callegaro. A simple algorithm to find the l-curve corner in the regularization of inverse problems. *CoRR*, abs/1608.04571, 2016.

[31] H. Kim and J. Rossignac. Parabola-based discrete curvature estimation. In *15th Int. Conf. on Computer Graphics, Visualization and Computer Vision (WSCG)*, Jan. 2006.

[32] Arya Bangun, Arash Behboodi, and Rudolf Mathar. Sparse recovery in wigner-d basis expansion. In *2016 IEEE Global Conference on Signal and Information Processing (GlobalSIP)*, pages 287–291, 2016.

[33] A. Gomez-Torrent, M. Garcia-Vigueras, L. Le Coq, A. Mahmoud, M. Ettorre, R. Sauleau, and J. Oberhammer. A low-profile and high-gain frequency beam steering subterahertz antenna enabled by silicon micromachining. *IEEE Trans. on Antennas and Propag.*, 68(2):672–682, Aug. 2020.

Chapter III

Antenna positioning for radiation pattern reconstruction

III.1   Introduction

III.1.a   Motivations

The positioning of the Antenna Under Test (AUT), i.e. its location and orientation in the anechoic chamber, is crucial to ensure the proper measurement of its radiation pattern. Therefore, alignment and centering procedures, that are often time consuming, are systematically used before any measurement. However, the accurate determination of the position of the antenna within the anechoic chamber is not an easy task, especially at high frequencies since this accuracy is tied to the wavelength. In addition, it is not always straightforward to guess in advance where to place at best the antenna in order to improve its radiation pattern characterization because of the possible interactions between the AUT and its surrounding. Besides, when the antenna is mounted on a structure, the Device Under Test (DUT) cannot always be positioned at will in the measurement system because of cinematic or weight constraints. For all these reasons, the development of a procedure to automatically find the best antenna positioning would greatly contribute in improving its radiation pattern characterization. In this chapter, the positioning of the AUT refers to both the position and the orientation of the antenna with respect to the measurement coordinate system. A translation refers to a change of the position and rotation to the orientation.

III.1.b   State of the art

Many works have been led to understand the influence of the AUT positioning on its radiation pattern measurement. It has been investigated for SW expansion in [1]. As illustrated in Fig. III.1, the power distribution over the spectrum of a dipole is shown to be connected to its distance from the origin.

New field sampling strategies have been proposed in [2] to improve the characterization of an offset-mounted antenna. When a relevant position to expand the field is known *a priori*, it is possible to translate the SW origin in post-processing so as to reduce its SW truncation order and to enable a down-sampled field acquisition, as smartly proposed in [3]. Finally, approaches to reduce the computational burden induced by a change of the SW expansion origin changes are given in [4]. Note that the change of the SW expansion
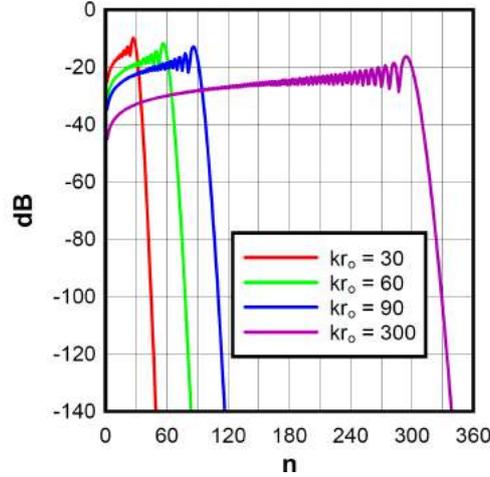
Figure III.1: The n-spectrum of the SW expansion of a Hertz dipole located at different electric distances kr_0 from the origin [1].

origin requires to adapt the probe compensation technique, which is necessary for spherical near-field measurements and has been addressed in [5].

Besides, two iterative approaches have been proposed to optimize the antenna positioning in post-processing. The first one [6] minimizes the number of significant modes to improve the field reconstruction quality according to the sparse recovery theory [7], as discussed in Section II.5. Indeed, the reconstruction accuracy from a low density field sampling is linked to the number of significant modes in the expansion, as shown in [8–11]. As illustrated in Fig. III.2, an inappropriate positioning generates many non-zero spherical coefficients while describing the same antenna yet.

(a) Rotated and shifted dipole.
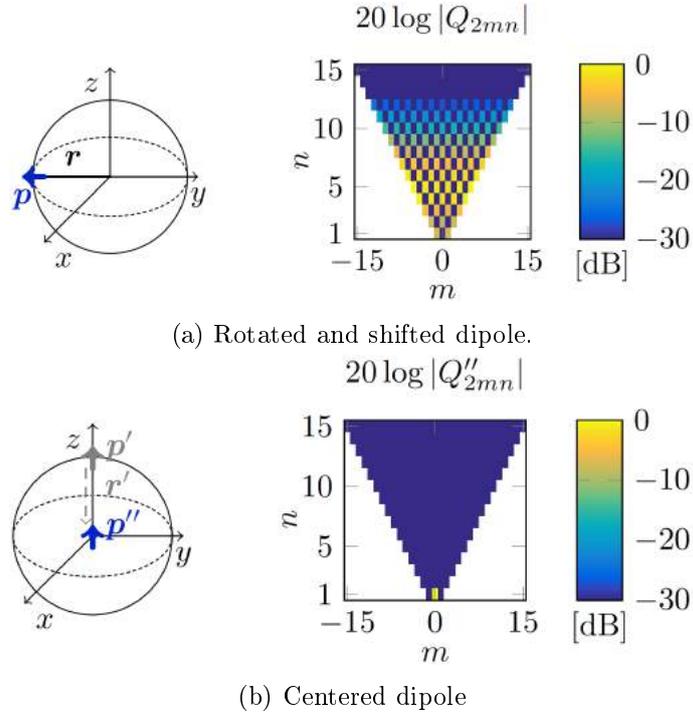

(b) Centered dipole

Figure III.2: Dipole positioning and corresponding SW spectra [6].

However, the number of non-zero coefficients is not the only indicator of a *good* or *bad* antenna positioning and the distribution of these coefficients over the spectrum also provides meaningful information. A second strategy [12] works over the power distribution over the spectrum, the n-spectrum, to estimate the so-called radiation center of the antenna. It corresponds to the phase center in the case of antennas having a single main beam. A fixed perturbation in the 6 directions from the current position (the 3 Cartesian ones in both ways) is applied with a fixed step. The origin is then moved in the direction leading to the best power concentration within a predetermined low frequency part of the spectrum.

Finally, the orientation of the AUT also modifies its SW spectrum. Consequently, one can legitimately wonder how to choose the coordinate system orientation yielding the sparsest field expansion. This very point has also been addressed by [6]. To our best knowledge, this is the only work where the AUT orientation is optimized to this end. Consequently, this work will be referred to as State-Of-the-Art (SOA) when dealing with antenna orientation optimization.

III.1.c Contributions

The Spherical Wave (SW) spectrum encompasses many valuable physical information about the AUT radiated field that deserve to be fully exploited. More precisely, it provides an identity card of the radiated field relatively to a given coordinate system. This means that both the position and the orientation of the antenna with respect to the measurement system influence the SW expansion, as illustrated with a dipole in Fig. III.2, from [6]. Although the antenna positioning is imposed by its placement in the measurement system at first, it can be changed after the acquisition of the field by post-processing. The analytical nature of the SW indeed allows for exact transformations on translating or rotating the electromagnetic field [13].

To optimize the positioning of the AUT, the SW spectrum must be concentrated towards low spatial or angular frequency content, i.e. the slowly varying SW, as they are easier to identify. The *best* position can thus be defined as the coordinate system origin achieving the highest concentration in the low-degree part of the SW spectrum, for which an appropriate metric is proposed thereafter. The optimization of the antenna orientation is performed by enhancing the sparsity of its SW spectrum, i.e. the number of non-zero coefficients involved in the expansion of the radiation pattern. Finally both approaches are combined into a full positioning optimization procedure that is carried out in post-processing, namely after the radiated field acquisition. Note that this antenna positioning procedure does not require any additional field measurement.

III.2 Spherical wave function transformations

The formula to achieve the analytical translation and rotation of the SW functions are given and their effects over the SW spectrum of an antenna are illustrated.

III.2.a Rotation

Let $\mathbf{r}$ be the position in the measurement coordinate system and $\mathbf{r}_{\text{rot}}$ the position in the one rotated according to Euler's angle $(\varphi_0, \theta_0, \chi_0)$ in zyz convention, as illustrated in Fig.
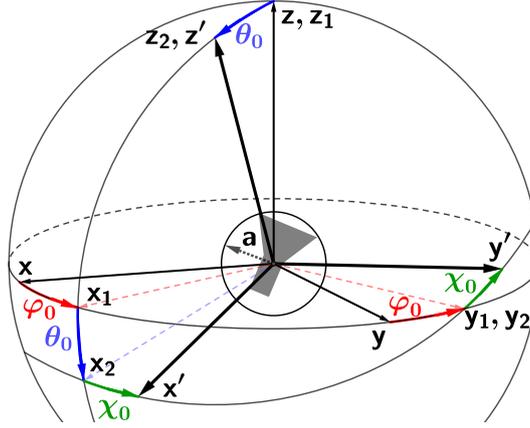
Figure III.3: Euler's angles in zyz convention. Three rotations of angles $(\varphi_0, \theta_0, \chi_0)$ with respect to the axis $\mathbf{z}, \mathbf{y}_1, \mathbf{z}_2 = \mathbf{z}'$ enables to go from the basis $\{\mathbf{x}, \mathbf{y}, \mathbf{z}\}$ to $\{\mathbf{x}', \mathbf{y}', \mathbf{z}'\}$. The radius of the minimum enclosing sphere around the antenna is denoted a. The intermediate basis $\{\mathbf{x}_1, \mathbf{y}_1, \mathbf{z}_1\}$ and $\{\mathbf{x}_2, \mathbf{y}_2, \mathbf{z}_2\}$ are also displayed.

III.3. We have from [13] p.343 the following expression

$$\mathbf{F}_{smn}(\mathbf{r}) = \sum_{\mu=-n}^{n} D_{\mu m}^{n}(\chi_0, \theta_0, \varphi_0) \mathbf{F}_{s\mu n}(\mathbf{r}_{\text{rot}}) \tag{III.1}$$

where $D_{\mu m}^{n}$ are the Wigner D-functions, defined from the (small)d-functions [14].

III.2.b   Translation

Let $\mathbf{r}$ be the position in the measurement system and $\mathbf{r}'$ the position in the translated one by some vector $\mathbf{d}$, as depicted in Fig. III.4. If the observation distance $\|\mathbf{r}\|$ is larger than the translation distance $\|\mathbf{d}\|$, for a translation over the z-axis, then we have from [13] p.353 the following expression

$$\mathbf{F}_{s\mu n}(\mathbf{r}) = \sum_{\sigma=1}^{2} \sum_{\substack{\nu=|\mu| \\ \nu \neq 0}}^{\infty} C_{\sigma\mu\nu}^{sn(1)}(k\|\mathbf{d}\|) \mathbf{F}_{\sigma\mu\nu}^{(c)}(\mathbf{r}') \tag{III.2}$$

where $C_{\sigma\mu\nu}^{sn(1)}(k\|\mathbf{d}\|)$ are the translation coefficients depending on the distance and the measured frequency.

An arbitrary translation is achieved by a 3 step process

1. A first rotation to align the translation vector with the z-axis.

2. A translation over the z-axis.

3. A second rotation to put the antenna back to its initial orientation.

The transformation of the coordinate system tied to the AUT can also be done more easily the in far field since it boils down to a simple phase shift. Let us consider an arbitrary component (e.g. $\hat{\theta}$ or $\hat{\varphi}$ component) of the electric far field E with respect to the measurement basis around O. The same field component in the translated measurement
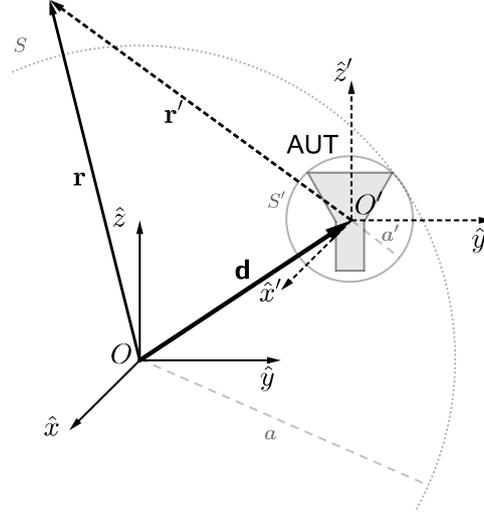
Figure III.4: Translation of the coordinate system by a vector $\mathbf{d}$. The corresponding minimal spheres enclosing the AUT are S, S' with radii a, a' respectively.

system around O', as in Fig. III.4, noted E_d is expressed as [15,16]

$$E_d = E e^{-jk\frac{\mathbf{r}'}{\|\mathbf{r}'\|}\cdot\mathbf{d}},\tag{III.3}$$

where $\cdot$ is the scalar product. Note that the amplitude and sampling positions changes are neglected when considering a far field scenario.

By applying either the SW transformation (III.2) or the phase shift of the field (III.3), the electric far field can be derived in any translated coordinate system. The modification of the SW is more accurate as there is no approximation over amplitude or sampling positions changes. This improved accuracy comes at a price of costly operations in terms of computational power.

III.3 Effects of antenna positioning on the spherical wave spectrum

A translation of the coordinate system is known to generate modifications on the distribution of significant spherical coefficients over both the degree n and the order m. More specifically, rotations have an impact only on the distribution over the order m, as rotation of a SW in (III.1) with given degree n is written using only SW of the same degree n. These considerations are represented in Fig. III.5. The intuitive explanation is that any rotation around the origin does not change the radius of the minimum sphere enclosing the AUT and thus the truncation order N in (II.15) of the SW series. Conversely, any translation does modify this radius and therefore N.

Illustrations with a simulated horn antenna

We illustrate these effects using a full wave electromagnetic solver (Ansys HFSS [17]) of a horn antenna at 30 GHz. The far field is expanded on the SW basis for several shifts of the antenna position over the z-axis by a step of a wavelength: at initial position, close to
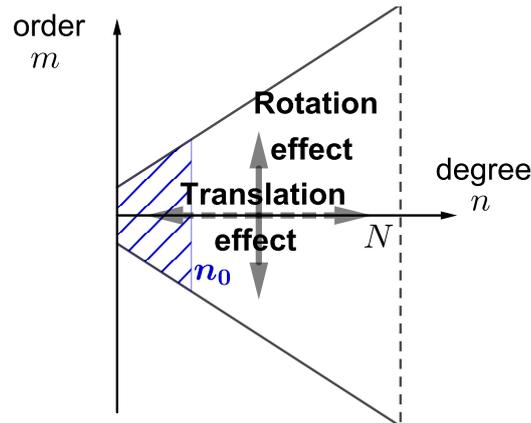
Figure III.5: Representation of a SW spectrum and the effects of a change in the coordinate system. Rotations will only have an effect over the order m while translations impact both the orders and the degrees n. The dashed region represents the area of the spectrum where $n \leq n_0$, a fixed, arbitrary, degree.

its *a priori* phase center, between the apex point of the flanges and the aperture [15], and after translations of the coordinate system origin of $1, 2$ and 3 wavelengths λ on the z-axis. The spherical coefficients are displayed in Fig. III.6. All these coefficient sets describe the same far field in magnitude, as only the phase changes significantly. As the translation of the AUT increases, the spread of the spectrum towards higher degrees n becomes more significant.
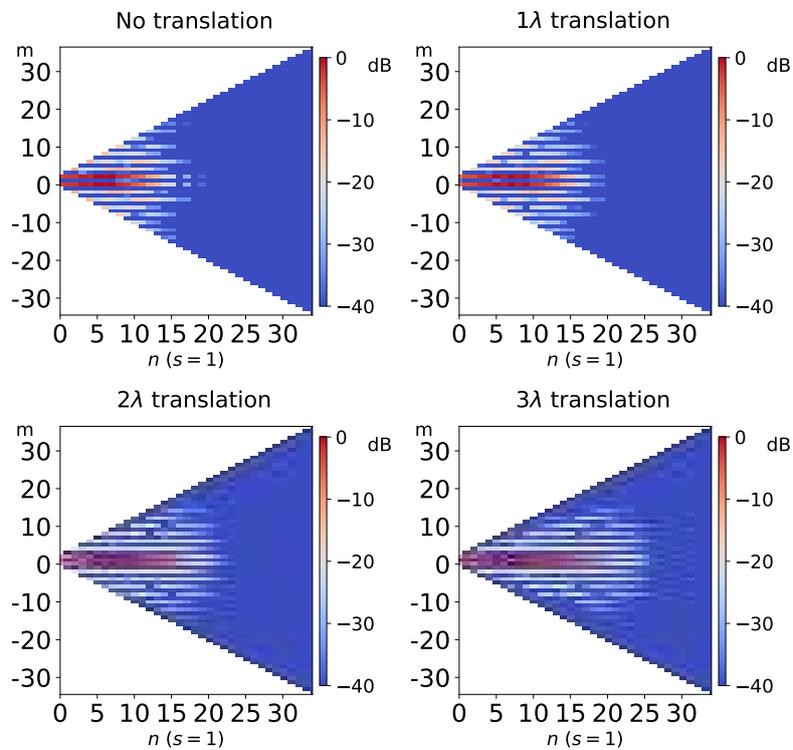

Figure III.6: Normalized spherical coefficients for $s = 1$ of the horn antenna at 30 GHz at several positions. Translations are performed along the z-axis.

A similar numerical investigation is carried out for the rotation of the AUT by random Euler's angle triplet and the results are displayed in Fig. III.7. As previously claimed, there is no spread of the significant modes to larger degrees n when changing the orientation of the antenna, but only over the orders m.
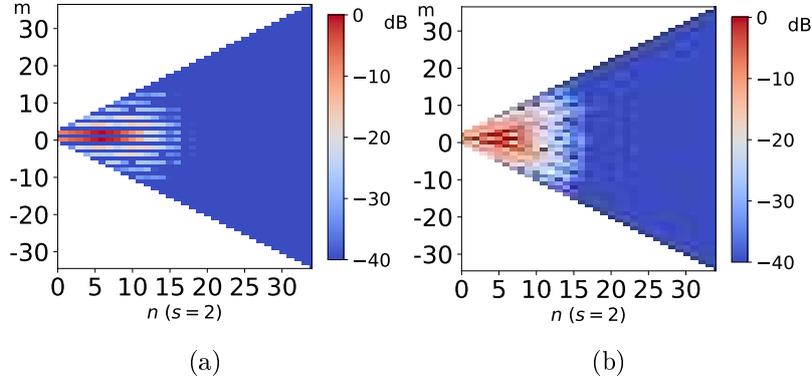

Figure III.7: Normalized SW spectra of a horn antenna at 30 GHz. (a) Expansion in the initial coordinate system and (b) after rotation by Euler's angles $(170, 32, 63)°$ (b).

III.4 Optimization of the antenna position

III.4.a Spherical coefficient distribution

The transformation of the coordinate system modifies the power distribution over the SW spectrum in both the order and the degree directions. We introduce a metric to quantify this distribution along the degree n. This metric is harnessed to better position the antenna and consequently to improve its radiation pattern characterization.

The n-spectrum

The spectrum is truncated at a given truncation order N defined in (II.15) from the minimal sphere. The power remaining in the spectrum for degrees $n \geq N$ must be negligible to ensure a proper characterization. This verification is called the N-test [13] and is based on the n-spectrum, already defined in (II.17) and recalled here. The power radiated for the spherical coefficient set Q_{smn} of an antenna at a given degree n is expressed as follows:

$$P(n) = \frac{1}{2} \sum_{sm} |Q_{smn}|^2. \tag{III.4}$$

As an illustrative example, let us consider the horn antenna simulated at 30 GHz previously investigated. The n-spectra corresponding to the spherical coefficients after various translations over the z-axis presented in Fig. III.6 are shown in Fig. III.8. The 0λ case means that the origin is centered around the phase center of the horn. The spread of significant modes to higher degrees n leads to greater values of the n-spectrum $P(n)$ in these regions.
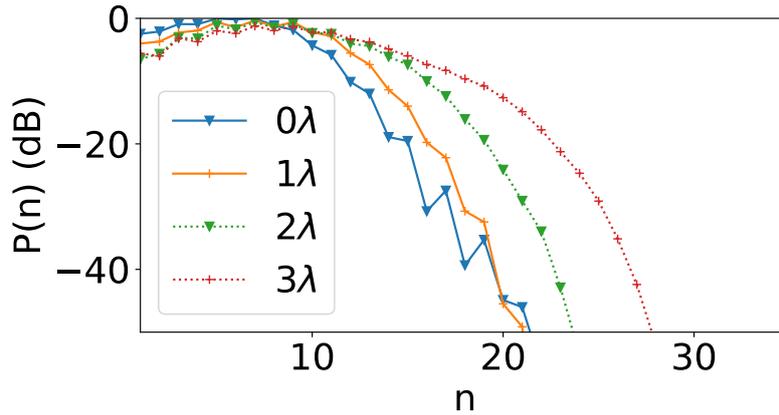
Figure III.8: Normalized n-spectra of the horn antenna at 30 GHz for different translations over the z-axis.

Advantages of Low Degree Modes

The *best* antenna position is defined in this chapter as the origin of the SW expansion leading to the highest concentration of the SW coefficient to low degrees n, or equivalently the fastest decreasing n-spectrum. There are multiple reasons to motivate this definition. A faster decrease of the n-spectrum allows the reduction of the truncation order N. Consequently, it requires less field samples and reduces computational load. For example in Fig. III.8 and a standard criterion of power below -40 dB, the horn properly positioned (no translation, 0λ) requires a minimum truncation order around $N = 20$, or 880 coefficients whereas the horn translated by a distance of 3λ needs at least $N = 27$, and consequently 1566 coefficients. Moreover, a low-degree spectrum induces a more compact representation of the antenna and is connected to the radiation center, as explained in [12].

The modes having high-spatial frequencies, or equivalently high-degree SW, require more field samples to be properly identified with respect to low-frequency ones, because of aliasing phenomenons. If the actual power distribution can lead to a reduction of the truncation order (e.g. by a N-test), the true number of unknowns decreases and fewer samples are thus required to achieve a proper reconstruction for a given accuracy level.

We illustrate this statement by randomly generating two families of 100 spherical coefficients spectra having the same total number of coefficients N_c, truncation order of $N = 45$, and non-zero coefficients (30 %). Non-zero coefficients are drawn over the degrees $n \leq 25$ for the first family and $n \leq 35$ for the second one. The only difference between the two families is the power distribution is constrained differently over the degrees. Using a sparse recovery approach, the BPDN in (II.28), each spectrum is recovered using far-field samples of different sizes M, or different sampling ratio M/N_c. The accuracy of the recovered spectrum is assessed by comparing the reconstructed far field from the M field samples to the one directly generated by the randomly drawn spectrum. This comparison is achieved using the Equivalent Error Signal (EES), understood as a synonym to the previously defined ENL. The results are displayed in Fig. III.9.

As an example, a field sampling ratio $M/N_c = 60\%$ is enough for all 100 trials of the low-frequency family ($n \leq 25$) to achieve a reconstruction accuracy of -45 dB in EES. Conversely, the high-frequency one ($n \leq 35$) never reached this accuracy for this sampling ratio and required around 70 % to perform equally well. This trend is expressed over all
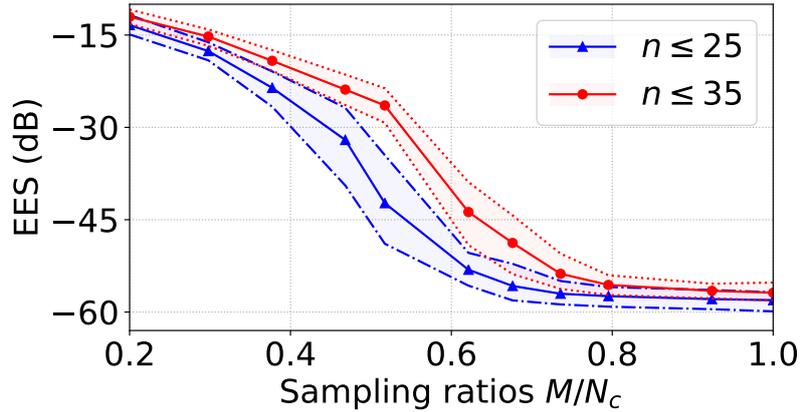
Figure III.9: Reconstruction accuracy in EES for 100 trials (median in plain lines and envelopes in dotted ones) for two spherical spectra families of same size N_c and same number of non-zero coefficients (30 %) but different power distributions over the degrees n (constrained to $n \leq 25$ or $n \leq 35$) with respect to the sampling ratio M/N_c, M being the size of the field sample used for recovery.

the sampling ratios as the median values of reconstruction accuracy in EES is always better for the lower frequency spectra using the same sampling ratio.

III.4.b   Determination of the antenna position

A simple criterion is presented to characterize the power distribution over the degrees. It is then used as an objective function in order to foster low-degree spectra.

The cumulative n-spectrum

The cumulative n-spectrum is defined for all degrees n lower than the truncation order N. Its value at a given degree $n_0 \leq N$ contains the power of all modes of degrees $n \leq n_0$, the region illustrated by the dashed area in Fig. III.5. We consider the normalized version, allowing a constant scale, which is not mentioned explicitly in the name for convenience in the sequel, and is given by

$$H(n_0) = \frac{1}{P_{\mathrm{rad}}} \sum_{n=1}^{n_0} P(n). \tag{III.5}$$

As a cumulative normalized function, it increases towards 1 as n_0 approaches the truncation order N. A faster decrease of the power in the n-spectrum leads to a cumulative spectrum reaching 1 more quickly, as illustrated in Fig. III.10, corresponding to the n-spectra of the horn at 30 GHz for several positions shown in Fig. III.8 and the spectra in Fig. III.6.

A cumulative spectrum can be associated to a mean value, which is defined by

$$\langle \mathbf{H} \rangle = \frac{1}{N-1} \sum_{n=1}^{N-1} H(n). \tag{III.6}$$

It is clear that a cumulative spectrum converging faster to 1 has a larger mean value. Mean values for the cumulative spectrum curves of the horn in Fig. III.10 are shown in Table
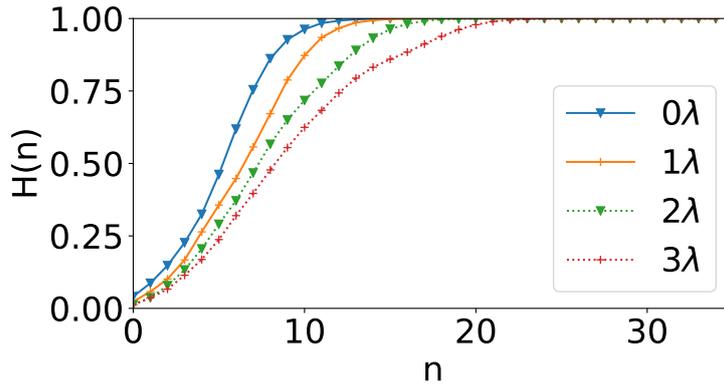
Figure III.10: Cumulative n-spectra H of a horn antenna at 30 GHz for different translations over the z-axis. A better concentration on low degrees n modes makes the curve approaching 1 for lower n-values.

III.1. We do not consider the last value $H(N)$ in the computation as it is always equal to 1.

In order to better emphasize the contrast between the cumulative spectra and to help the choice of the best antenna position, we replace H by a modified version defined as:

$$H_{\text{mod}}(n) = 10 \log_{10} \left[\frac{n}{N} (1 - H(n)) \right]. \tag{III.7}$$

Working on $1 - H(n)$ maps the increase towards 1 of the cumulative spectrum function to a decrease to 0, where values can be better discriminated by the logarithmic scale. The multiplication by n/N accounts for the number of SW of same degree n while keeping the values in the interval $[0, 1]$. The values of the cumulative spectrum and its modified version are reported in Table III.1 for the horn simulated at 30 GHz, showing the improvements in the discrimination of high-frequency content of this adapted metric.

Table III.1: Means of the cumulative n-spectra of the Horn at 30 GHz for Several Translations over the z-axis:

Translation Distance	0λ	1λ	2λ	3λ
$\langle \mathbf{H} \rangle$	0.84	0.80	0.77	0.73
$\langle \mathbf{H}_{\text{mod}} \rangle$ dB	-69.1	-67.7	-52.4	-24.1

III.4.c Optimization problem formulation

The concentration of the power distribution to the low-degree part is achieved by a minimization of the mean value of cumulative n-spectrum on the modified scale $\langle \mathbf{H}_{\text{mod}} \rangle$. Given a translation $\mathbf{d}$ of the AUT relatively to the origin of the measurement coordinate system, as in Fig. III.4, we identify the spectrum $\mathbf{Q_d}$ with the method of our choice (analytical projection or numerical inversion), enabling the evaluation of the cumulative n-spectrum and therefore its mean value, denoted $\langle \mathbf{H}_{\text{mod}} \rangle(\mathbf{Q_d})$. This optimization problem can be formulated as follows

$$\min_{\mathbf{d}} \langle \mathbf{H}_{\text{mod}} \rangle(\mathbf{Q_d}). \tag{III.8}$$

The solution of this optimization problem is an estimation of the *best* translation to apply to the AUT, leading to the highest concentration of the radiated power on the low degree part according to our metric. This solution is denoted $\mathbf{d}^*$.

Note that in the case of a numerical inversion to find the spectrum $\mathbf{Q_d}$, two situations can be distinguished to get the matrix formulation (II.22) after a translation $\mathbf{d}$:

- $\mathbf{A_d x} = \mathbf{y}$ with near- or far-field data, with $\mathbf{A_d}$ the translated version of the SW contained in $\mathbf{A}$.

- $\mathbf{A x} = \mathbf{y_d}$ where $\mathbf{y_d}$ contains electric far-field data and computed according to (III.3).

This antenna position procedure is carried out in post-processing, once the AUT measurements are done. No additional measurements are required.

III.4.d   Optimization of antenna position using gradient descent.

We propose an iterative algorithm to solve the optimization problem (III.8) and find the antenna position that concentrates the significant spherical modes on the low degrees.

Gradient Descent Algorithm

The optimization of the position, or equivalently the translation $\mathbf{d}$ from the origin of the measurement coordinate system, using (III.7) or (III.8) is not a convex problem and cannot be solved easily. We propose a gradient descent technique to find the translation $\mathbf{d}^*$ corresponding to the *best* AUT position. This iterative algorithm follows the negative (approximated) gradient of the objective function, $\langle \mathbf{H}_{\mathrm{mod}} \rangle (\mathbf{Q_d})$. The detailed procedure is given in Algorithm 1. The proposed approach is general and can be applied with no modification to all spherical coefficient identification methods (analytical and numerical ones), for both near-field and far-field measurements.

Algorithm 1 Concentration of the spherical spectrum power distribution to low degrees

---

Require: δ the perturbation step, μ the gradient multiplier, $\mathbf{d}_0$ the initialization point.
 1: **Initialization**
 2: $\mathbf{d} \leftarrow \mathbf{d}_0$
 3: **while** Stopping criterion not met **do**
 4:    Apply the translation $\mathbf{d}$
 5:    Compute the spherical coefficients at $\mathbf{d}$, $\mathbf{Q_d}$
 6:    Evaluating $\langle \mathbf{H}_{\mathrm{mod}} \rangle (\mathbf{Q_d})$
 7:    # *Computation of the numerical gradient* $\mathbf{D}$
 8:    **for** $\hat{u} = \hat{x}, \hat{y}, \hat{z}$ **do**
 9:        $\mathbf{d}_{\hat{u}} \leftarrow \mathbf{d} + \delta \hat{u}$
10:        Compute the spherical coefficients at $\mathbf{d}_{\hat{u}}$, , $\mathbf{Q}_{\mathbf{d}_{\hat{u}}}$
11:        Evaluating $\langle \mathbf{H}_{\mathrm{mod}} \rangle (\mathbf{Q}_{\mathbf{d}_{\hat{u}}})$
12:        $D_{\hat{u}} \leftarrow \left[\langle \mathbf{H}_{\mathrm{mod}} \rangle (\mathbf{Q}_{\mathbf{d}_{\hat{u}}}) - \langle \mathbf{H}_{\mathrm{mod}} \rangle (\mathbf{Q_d}) \right] / \delta$
13:    $\mathbf{D} \leftarrow [D_{\hat{x}}, D_{\hat{y}}, D_{\hat{z}}]^T$
14:    # *Position Update*
15:    $\mathbf{d} \leftarrow \mathbf{d} - \mu \mathbf{D}$
16: **return** $\mathbf{d}$

Implementation Details

The perturbation step δ is the (small) change applied to the translation for approximating the gradient of the metric. This value has to be chosen relatively to the expected accuracy of the measurement system configuration to generate perturbations that are meaningful with respect to the available data. A too small δ would result in a noisy and unstable estimation. Conversely, a too large δ would lead to unfaithful and too coarse gradient evaluation. A value of $\delta = 0.5$ mm has been successfully used in all presented cases. The gradient multiplier μ is a constant chosen in order to avoid large updates of $\mathbf{d}$ within one iteration by a proper re-scaling of the gradient. It should be fixed so that the position update is not too large in terms of wavelength or with respect to the tested structure to ensure proper convergence of the algorithm. A value $\mu \approx 10^{-5}$ for normalized data ($\|\mathbf{y}\| = 1$) leads to updates around several mm for most cases.

The initialization point $\mathbf{d}_0$ in Algorithm 1 can be set using various methods. A starting value $\mathbf{d}_0 = \mathbf{0}$ means that the optimization is started from the origin of the measurement coordinate system. It can also be chosen randomly or one can provide an initial guess based on some prior knowledge, e.g. the estimated known position of the AUT geometrical center with respect to the measurement coordinate system.

Multiple stopping criteria can be chosen. One can use the difference of the cost function between two or more iterations, the decrease of the cost function below a predefined threshold or define a maximum distance for the translation $\mathbf{d}$, (for example with respect to the wavelength or the dimensions of the antenna), or a predefined number of iterations.

With proper parameter tuning, a notable reduction of the objective function has been achieved within only a few iterations for all investigated cases. The translation corresponding to the lowest value of the cost function should be kept.

III.4.e Validations on near-field simulations

The proposed approach for AUT position optimization is applied on various radiating structures, whose near field is computed by CST MWS [18].

Antenna linear 11-Patch Array at 9.5 GHz

Let us consider a linear array composed of 11 patches operating in X band at 9.5 GHz, an illustration is given in Fig. III.11. Each square patch has side length of 10 mm and the overall size of the array is 165 mm ($\approx 5.25\lambda$), the electric near field is exported from CST at 200 mm from the geometric center. As illustrated, not all patches are fed with the same amplitude. The left patch is not receiving any power and the feeding is increasing as we go to the right patch in order to generate an asymmetric current distribution. The truncation order is $N = 27$, or 1566 coefficients and a field sample along an *igloo* sampling of size 900 is taken to generate a very coarse measurement set and is used for both position optimization and reconstruction.

Taking the geometric center of the array as the origin yields the spectra displayed in Fig.III.12.a while the optimized position yields the ones in III.12.b. If the geometric center of the antenna is taken as the origin of the measurement coordinate system, the proposed algorithm finds the optimized coordinate system origin to be at $\mathbf{d}^* = (0.6, 18.7, 2.1)$ mm, meaning that it is shifted towards the area containing most part of the electric current density. It also preserves the symmetry around the x-axis, the orthogonal direction to
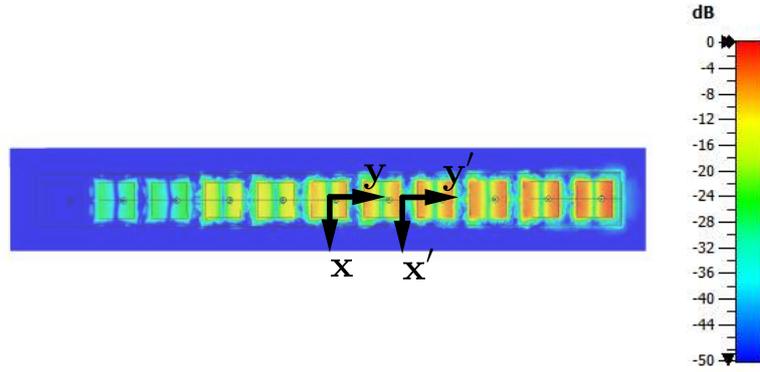
Figure III.11: Normalized surface current magnitude of the 11-patch array (average value over one phase cycle): measurement coordinate system $(\mathbf{x}, \mathbf{y})$ (geometric center) and optimized one $(\mathbf{x'}, \mathbf{y'})$.

the array, with a shift of less than $\lambda/50$. No additional knowledge have been used in the process. The whole AUT position optimization process takes about 52 s on an Intel i7 8700 with 16 GB RAM.

The optimized coordinate system position enables not only to significantly reduce the amount of significant spherical coefficients but also to concentrate them to low-degree modes as displayed in Fig. III.12.
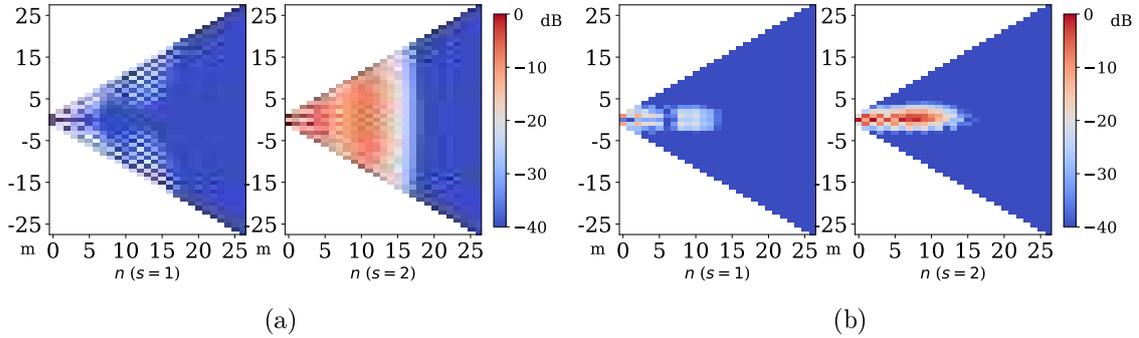

Figure III.12: Normalized spherical coefficients of the patch array: (a) with origin at the geometric center, (b) with optimized position.

The accuracy of the reconstructed radiated field from the same initial data set with respect to the reference (the electric spherical near field exported from CST over a dense set of points) are evaluated by EES values of -42.5 dB for the geometric center and -56.5 dB for the optimized position. The co-polarization component of the field magnitude for the reference data and the reconstructions with and without optimization of the position are displayed in Fig. III.13. There are clear improvements in the reconstruction of the field using the fast measurement sampling thanks to the position optimization.

Antenna on a satellite structure at 11 GHz

As a study case, a single rectangular patch is now placed on a platform of the satellite ANGELS [19] (the real payload being a different antenna), the whole structure is displayed in Fig. III.14 and we exploit the simulated spherical near field simulated at 5 m from the
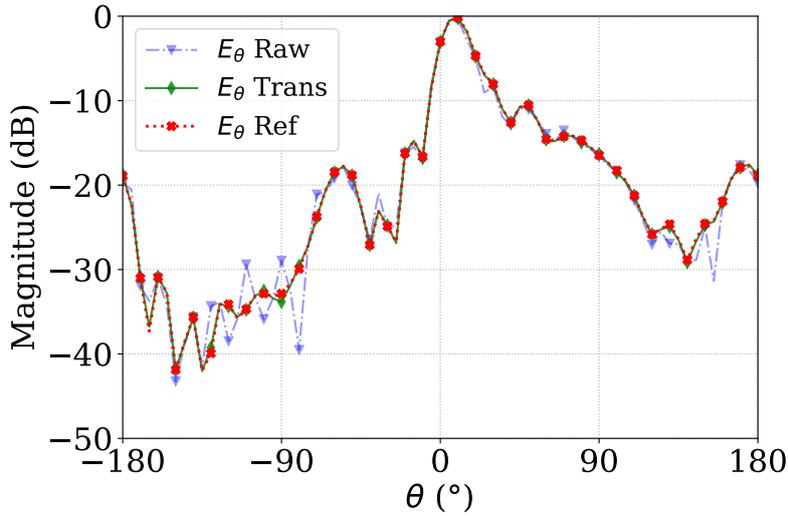
Figure III.13: Electric field normalized magnitude in the main cutting plane. Comparison of the reference and the reconstructions using the fast measurement sampling before (Raw) and after (Trans) position optimization.

origin of the measurement coordinate system, supposed at the center of the satellite's body for practical reasons: cinematic or weight for instance. The minimum sphere is set to enclose the satellite body and some parts of the solar panels, leading to 6726 spherical coefficients. The dataset comes from a field sampling of size 1700 along an *igloo*. There are enough data with respect to the patch alone according to the fast measurement sampling rule while still having a largely under-determined linear system to cope with for the whole structure.

The geometric center of the antenna is then located at $\mathbf{d}^c = (0, 120, 113)$ mm from the center of the satellite, which corresponds to a distance of approximately 6λ. The optimization process starts from the center of the satellite and converges to an optimized position of $\mathbf{d}^* = (0.3, 125.6, 102.9)$ mm that turns out to be fairly close to the coordinates of the antenna geometric center. The spectra are represented in Fig. III.15 and the modified cumulative n-spectra $\mathbf{H}_{\mathrm{mod}}$ are shown in Fig. III.16. The returned optimized position is close but not equal to the geometric center, resulting in a different power distribution. Indeed, we observe more power at very low degrees when centered at the antenna but the optimized position allows a faster decrease of the contained power for degrees $n \geq 10$, allowing for a slightly more accurate far-field reconstruction for the considered data. The obtained EES of the reconstructed field from the same initial data over a dense reference sampling are respectively -43.1 dB and -43.6 dB for the centered on the antenna and the optimized position from the center of the satellite.

Discussion

The geometry of the radiating structure does not always help the choice of the origin for the coordinate system of the SW expansion. In the patch array case, various excitation sets induce different radiation patterns and consequently several ideal coordinate system origins. The proposed procedure enables to automatically determine the position leading to a high concentration of the spectrum over the low-degree modes without any knowledge
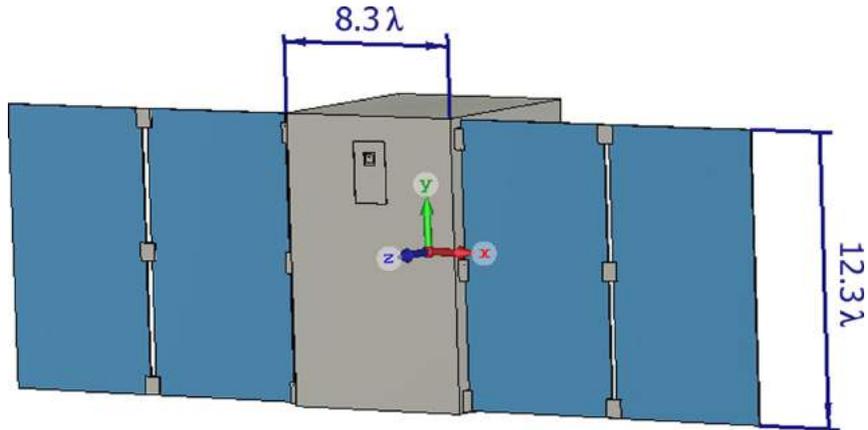
Figure III.14: Simulated model of the antenna (a patch) on a platform satellite (a simplified version of ANGELS) with the patch antenna at 11 GHz and the measurement coordinate system.
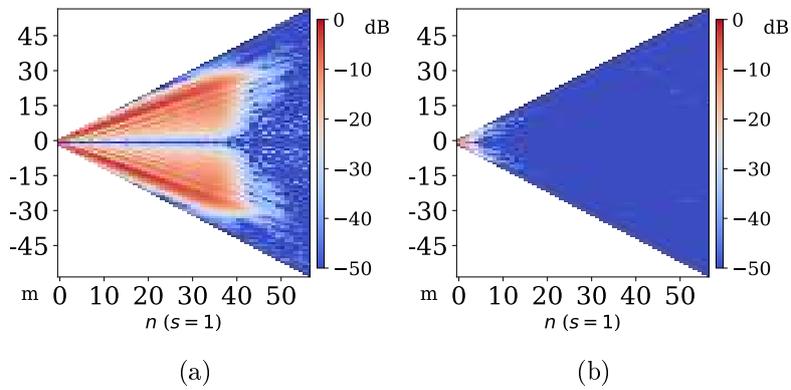

Figure III.15: Normalized spherical coefficients for $s = 2$ of the mounted patch at 11 GHz: (a) measurement coordinate system, (b) optimized position.
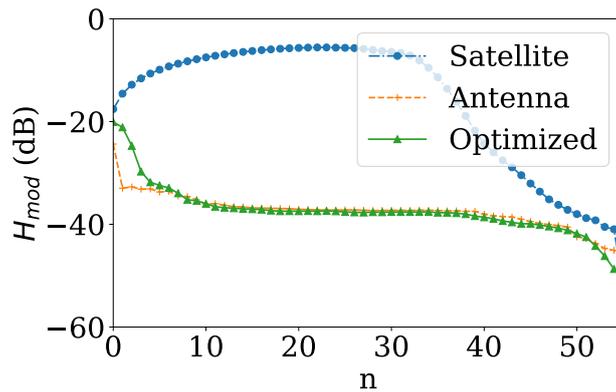

Figure III.16: Modified scale of the cumulative n-spectra for the initial measurement origin, centered on the antenna and with optimized position.

of the structure apart from its maximum dimension and measured frequency in order to set the truncation order of the SW series. It is of great interest for reconfigurable antennas, where several operating modes must be tested. In the case of the antenna embedded in a

satellite, the procedure automatically finds the *best* position (according to our metric), at a distance of around 6 λ from the measurement origin. This optimized location yields a slight improvement of the pattern reconstruction and confirm the stability of the proposed procedure. Indeed, despite having a small number of measurement samples with respect to the spherical coefficients to be determined, the necessary large translation of the AUT is properly retrieved.

These representative numerical examples demonstrate the robustness of the approach as well as its practical relevance. The proposed procedure enables to compensate automatically uncertainties on the antenna position with respect to the measurement system. It also allows to accurately position embedded antennas when the interaction between the radiator and its structure cannot be neglected.

III.4.f   Validations on far-field measurements

Let us now consider radiating structures that have been measured in the far-field anechoic chambers of the M^{2}ARS facilities at IETR. These facilities are equipped with a roll-over-azimuth positioning system and a mechanical probe polarization change. The field is acquired step by step following an *igloo* strategy [9].

Two antenna far-field measurements, carried out over an hemisphere using a low-density sampling, are presented here. The reference is provided by a measurement of a densely sampled cutting plane. Since the sampling positions only cover a hemisphere in far field, we can restrict ourselves the modes of $\mathbf{F}_{smn}$ such that $n + m$ is even. By assuming the symmetry of the radiation pattern with respect to the equator, all the spherical coefficients Q_{smn} such that $m + n$ is odd are necessarily zero. This trick further reduces the number of samples required to characterize the radiation pattern over the measurement region.

Leaky Wave Antenna (LWA) in K Band

The AUT is a LWA designed and measured at IETR at 18 GHz, based on [20]. Let us compare the reconstruction of the field over the cutting plane $\varphi = 90°$ for the measurement coordinate system origin and the optimized position using the proposed approach. The antenna has a radius of $a = 15$ cm, leading to a truncation order of $N = 65$ hence 4420 even spherical coefficients to retrieve. The measurement data follows an *igloo* sampling and has size 3458, leading to a sampling ratio of 78 %, slightly above the 75 % required by our previous study for fast measurements in [21]. The usual method in [13] would have required a data set of size around 1.7×10^4. The antenna have been measured using a CATR configuration in CAMILL described in Section I.2.c. To be properly located in the quiet zone, the antenna had to be shifted away from the nominal position in terms of minimal sphere, leading to high-degree contributions ober the degree n.

The spherical coefficients before and after optimization for one propagating mode s are displayed in Fig. III.17, leading to the objective function $\langle \mathbf{H}_{\mathrm{mod}} \rangle$ values of -11.2 dB and -39.5 dB with a proportion of significant coefficients being 54 % and 27 % respectively. The cutting plane for comparison to reference is shown in Fig. III.18. We observe a much better agreement of the field reconstruction when optimizing the position of the antenna. The reconstructed field phases around the main beam angular zone are plotted in Fig. III.19. These phase behaviors have been smoothed out significantly after repositioning the AUT by applying the proposed procedure. Using the data phase-shift equation (III.3) for
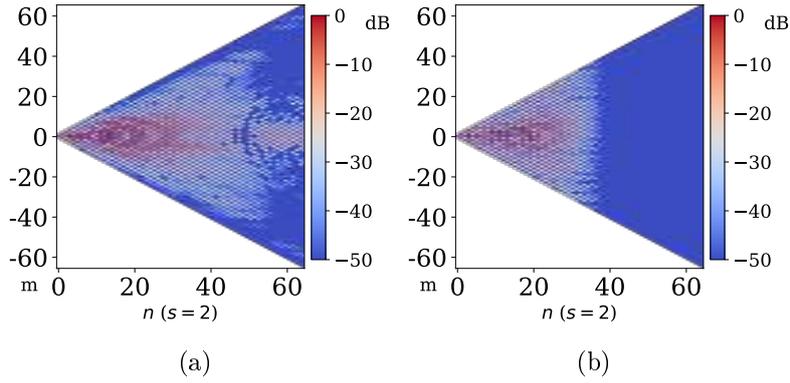
(a) (b)

Figure III.17: Normalized spherical coefficients for $s = 2$ of the LWA at 18 GHz (a) for the measurement coordinate system origin position and (b) with optimized position .

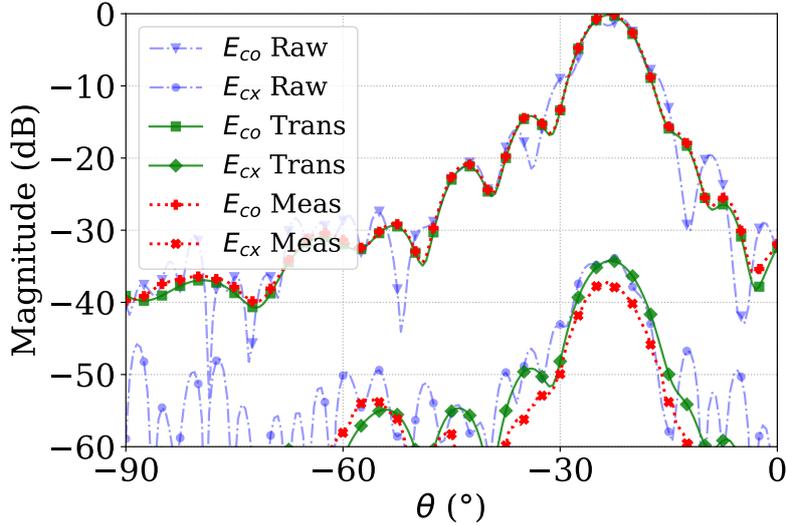optimizing the AUT position, the optimization process took 47 s on an Intel i7 8700 with 16 GB RAM.

Figure III.18: Normalized magnitude of the field co- and cross-polarization components over the cutting plane $\varphi = 90°$ of the LWA at 18 GHz .

Circularly polarized horn antenna at 320 GHz

This antenna has been designed and measured at IETR [22] along a coarse sampling over the hemisphere at 320 GHz. We use the same methodology as the previous one with a cutting plane at $\varphi = 0°$. The minimal sphere leads to a truncation order of $N = 50$, hence 2650 even coefficients. The measurement data set has been acquired along an *igloo* sampling and of size 2122, corresponding to a sampling ratio $\approx 80\%$. The usual method in [13] would have required a data set of size around 10^4.

The spherical coefficients for one propagating mode s for measurement and optimized positions are displayed in Fig. III.20, leading to objective function $\langle \mathbf{H}_{\mathrm{mod}} \rangle$ values of -22.2 dB and -26.6 dB with proportion of significant coefficients of 15 % and 6 % respectively. The cutting plane in magnitude for comparison to the reference is shown in Fig. III.21.
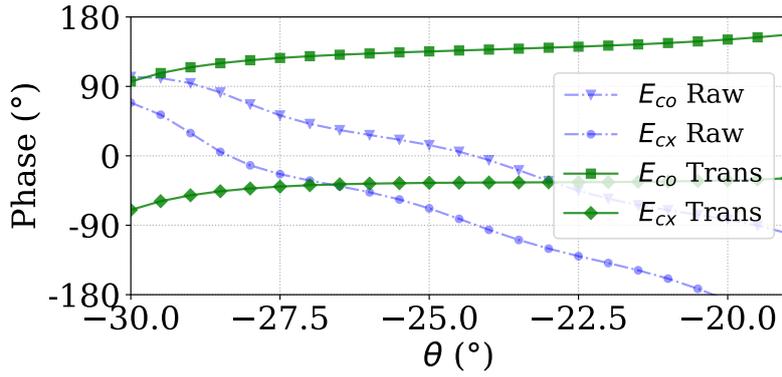
Figure III.19: Phases of the reconstructed field co- and cross-polarization components around the main lobe over the cutting plane $\varphi = 90°°$ of the LWA at 18 GHz .

The reconstructed field phases around the main beam angular zone are plotted in Fig. III.22, the optimized antenna position leads, here as well, to smoother phase variations.
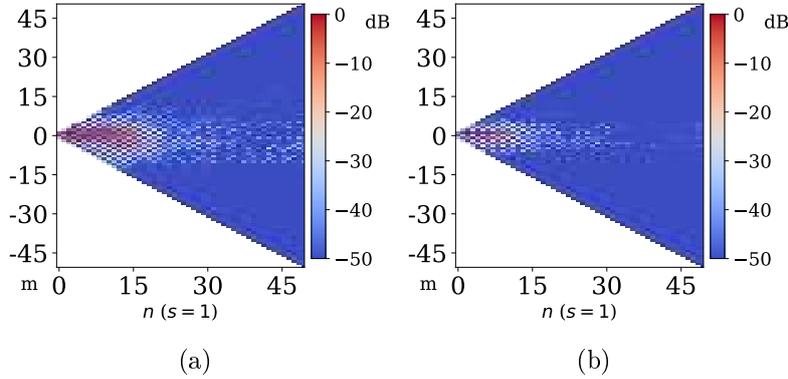

Figure III.20: Normalized spherical coefficients for $s = 1$ of the horn at 320 GHz (a) for the measurement coordinate system origin position and (b) with optimized position .

Discussion

The concentration of the spectrum in low-degree modes has been achieved in both cases as shown by the spectra. This leads to significant improvements in the field reconstruction from a given initial undersampled far-field dataset and thereby validates experimentally our approach. The position optimization of the antenna induces smoother phase variations over the main beam. This particular point is described in [12,23] and referred to as the antenna radiation center, the virtual point from which the main beam of the antenna is emitted.

III.5 Optimization of the antenna orientation

The orientation of the AUT is optimized in order to foster the sparsity of its SW spectrum. A sparser SW spectrum can indeed be correctly retrieved from a smaller number of field samples as shown in Section II.5. Consequently, the effective sparsity is used as a metric to optimize the rotation of the AUT.
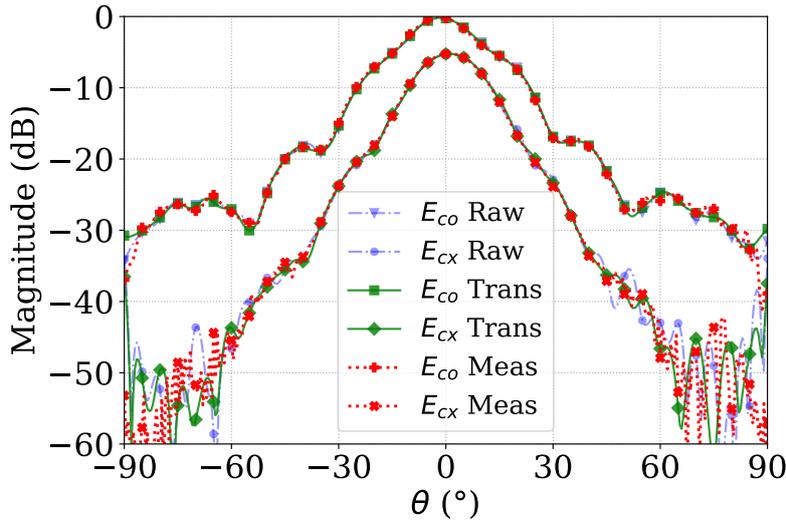
Figure III.21: Normalized magnitude of the field co- and cross-polarization components over the cutting plane $\varphi = 0°$ of the horn at 320 GHz.
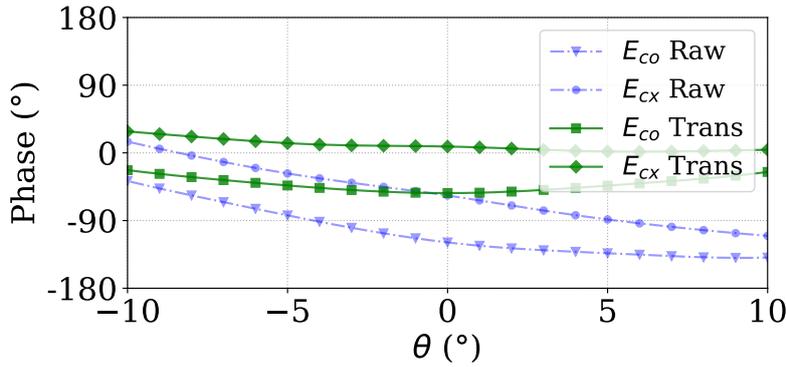

Figure III.22: Phases of the reconstructed field co- and cross-polarization components around main lobe over the cutting plane $\varphi = 0°$ the horn at 320 GHz.

III.5.a   Optimization problem formulation

The goal is to find the rotation angles $(\varphi_0, \theta_0, \chi_0)$ leading to the sparsest SW representation of the field radiated by the AUT. The rotation angle φ_0 only introduces a phase shift according to (III.1), and thus does not influence the sparsity of the antenna spectrum. Therefore, only the couple of rotation angles (θ_0, χ_0) has to be determined. After rotations of angles (θ_0, χ_0), the equation satisfied by the radiated field reads

$$(\mathbf{AR}_{\theta_0, \chi_0})\mathbf{x}(\theta_0, \chi_0) = \mathbf{y} \qquad\qquad (\text{III.9})$$

where $\mathbf{R}_{\theta_0, \chi_0}$ is the matrix encoding the rotation of the SW, described in (III.1) for the couple (θ_0, χ_0). We then solve:

$$\min_{\mathbf{x}} \|\mathbf{x}\|_1 \text{ subject to } \|\mathbf{AR}_{\theta_0, \chi_0}\mathbf{x} - \mathbf{y}\|_2 \leq \sigma \qquad\qquad (\text{III.10})$$

We evaluate the effective sparsity k_{-40} defined in (II.31) of the solution $\mathbf{x}(\theta_0, \chi_0)$ using only the two rotation angles (θ_0, χ_0). The computation of $\mathbf{R}_{\theta_0, \chi_0}$ takes about 1.5 s and the resolution of (III.10) using SPGL1 takes about 1.2 s for a matrix $\mathbf{A}$ of size 2522×4606 with an Intel i7-8700 and 16 GB RAM. The resolution of the BPDN problem is not as time consuming as computing the SW rotation matrix. However, testing a lot of couples (θ_0, χ_0) may become a heavy computational task. To avoid that difficulty, the effective sparsity of the SW spectra, noted $k_{-40}(\theta_0, \chi_0)$, is estimated from a coarse (θ_0, χ_0) grid using Gaussian processes and a relevant restriction of the research domain.

The SOA method [6] proposes to find $\mathbf{x}(0, 0)$ before optimizing over the three Euler's angles by minimizing $\|\mathbf{R}_{\varphi_0, \theta_0, \chi_0} \mathbf{x}(0, 0)\|_1$. Note that this problem is much harder than minimizing $\|\mathbf{Tx}\|_1$ for a given matrix T, as it cannot be casted into a convex optimization problem. Iterative minimization methods, such as gradient descent, may be trapped in local minima and will require a lot of rotation matrix computations. The optimization has to be done for several initialization points and one should keep in mind that the final result may not be the true minimum.

III.5.b   Effective sparsity minimization

The rotation of the SW basis can be seen as the rotation of the AUT into the new coordinate system. Physically, it represents a continuous modification of the field, and thus of its spectrum. The function $k_T(\mathbf{x}(\theta_0, \chi_0))$ can consequently be fairly well approximated by a continuous function, as shown in Fig. III.23. Gaussian Processes (GP) are stochastic objects that can be used to interpolate continuous functions. They are well adapted to situations where evaluating the function is computationally heavy. GP have already shown a great relevance in many applications and motivated a lot of research [24]. They enable the computation of confidence intervals and parameters tuning for better estimation depending on the fed data. The region with the lowest sparsity is indeed well identified with a few samples. In this case, the SOA method detects a sparsity minimum but the minimization of $\|\mathbf{R}_{\varphi_0, \theta_0, \chi_0} \mathbf{x}(0, 0)\|_1$ does not lead to the correct Euler's angles.
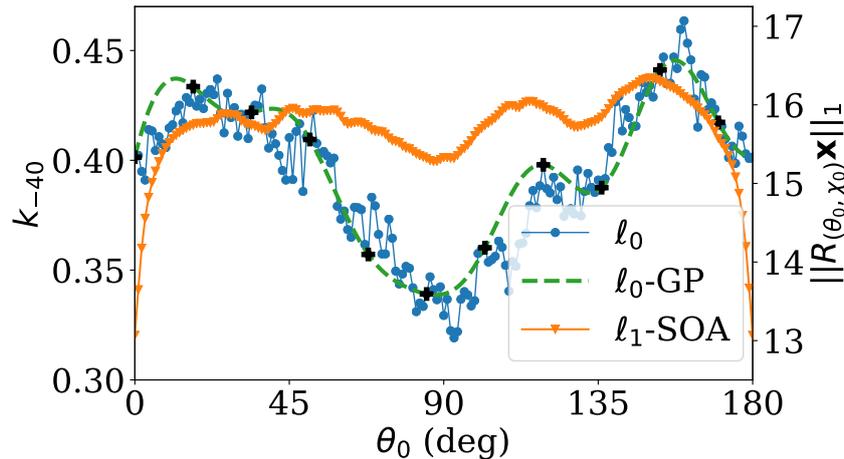

Figure III.23: Effective sparsity k_{-40} for $\chi_0 = 0°$, containing the minimum of k_{-40}, its GP estimation and the ℓ_1 norm found by the SOA method of the spherical coefficients for the 12 GHz reflectarray measurement. The GP curve is derived from the discrete set of values represented by black markers.

The objective is to interpolate the effective sparsity function $k_T(\mathbf{x}(\theta_0, \chi_0))$ from a reduced number of values, at points $(\theta_0^{(p)}, \chi_0^{(p)})$. The interpolation $\widetilde{k}_T$ is therefore an estimation.

Interpolation using Gaussian processes

A GP is characterized by its expectancy, set to 0 in our case, and its covariance, or kernel function, $\mathbb{V}$. Let us define $\mathbb{V}(\mathbf{a}_1, \mathbf{a}_2) = h(\|\mathbf{a}_1 - \mathbf{a}_2\|) = \exp(-\frac{\|\mathbf{a}_1 - \mathbf{a}_2\|^2}{2l^2})$, where $\|\cdot\|$ is the Euclidean norm and l a positive parameter characterizing the distance at which points influence themselves. This kernel is named square exponential and is known to produce indefinitely differentiable curves [24]. If $\mathbf{a} = (\theta_0, \chi_0)$ and the known values of k_T are located at points $\mathbf{a}^{(p)} = (\theta_0^{(p)}, \chi_0^{(p)}), p \in \{1, \ldots, P\}$, then let $\mathbf{K}$ be the vector gathering the $k_T(\mathbf{a}^{(p)})$ and the following estimation [24] can be made

$$\widetilde{k}_T(\mathbf{x}(\mathbf{a})) = \left[\mathbb{V}(\mathbf{a}, \mathbf{a}^{(1)}) \ \ldots \ \mathbb{V}(\mathbf{a}, \mathbf{a}^{(P)})\right] \mathbf{V}^{-1}\mathbf{K} \tag{III.11}$$

where $\mathbf{V} = (v_{lm})$ is the matrix containing the covariance between the data points $\mathbf{a}^{(i)}$, i.e. $v_{lm} = \mathbb{V}(\mathbf{a}^{(l)}, \mathbf{a}^{(m)})$. Once the values k_T are known at some points, evaluating $\widetilde{k}_T$ can be done by small scale matrix multiplications, enabling the use of many fast optimization techniques.

Research domain and testing grid of the cost function

The initial domain of (θ_0, χ_0) is $[0, 180] \times [0, 360]$ in degrees. Thanks to the symmetries of the SW, this angular region can be reduced to $(\theta_0, \chi_0) \in [0, 180[\times[0, 90[$. First, the case $\theta_0 = 0°$, or $180°$ by symmetry, has to be computed once, because it only induces a phase shift of the coefficients. Secondly, a first known rotation in χ_0 can be applied to ensure that the main beam of the field can be sent to one of the pole or to achieve symmetry with respect to the equatorial plane, ensuring proper minimization of the number of non-zero coefficients. The number of tested points has been chosen empirically and these points are regularly spaced on a testing grid with a step of $17°$, allowing to capture the global behaviour of the effective sparsity. This procedure implies the resolution of 61 BPDN problems to solve and computation of rotation matrices, 6 different χ_0 values for 10 θ_0 values plus one at $\theta_0 = 0°$. Finally, the characteristic length l of the GP is set to $22.5°$. This value is between $17°$ and $17\sqrt{2} \approx 24°$, that are the length of the edge or the diagonal of a cell of the testing grid, respectively

III.5.c Validation on near-field simulations

A waveguide array at 50 GHz antenna is modelled numerically using HFSS. The array is composed of 13 open ended waveguides with $3\,\mathrm{mm} \approx \lambda/2$ spacing. The excitations of the waveguides have the same magnitude but different phases, with an enclosing sphere of radius $a = 25\,\mathrm{mm}$, hence a truncation order $N = 36$ (or $N_c = 2736$ coefficients).

The near and far fields are exported over an equiangular sampling scheme, $\delta\varphi = \delta\theta = 2°$ (where $\delta\varphi$ and $\delta\theta$ are the angular steps in φ and θ respectively) over the full sphere, constituting the reference data set. The reference set has 6152 samples, while the near-field subsample, used for sparse recovery, has only 1876 samples. The measurement coordinate system $(\mathbf{x}, \mathbf{y}, \mathbf{z})$ does, on purpose, not correspond to the symmetry of the array. The

spherical coefficients with and without rotation found by GP interpolation are shown in Fig. III.24.

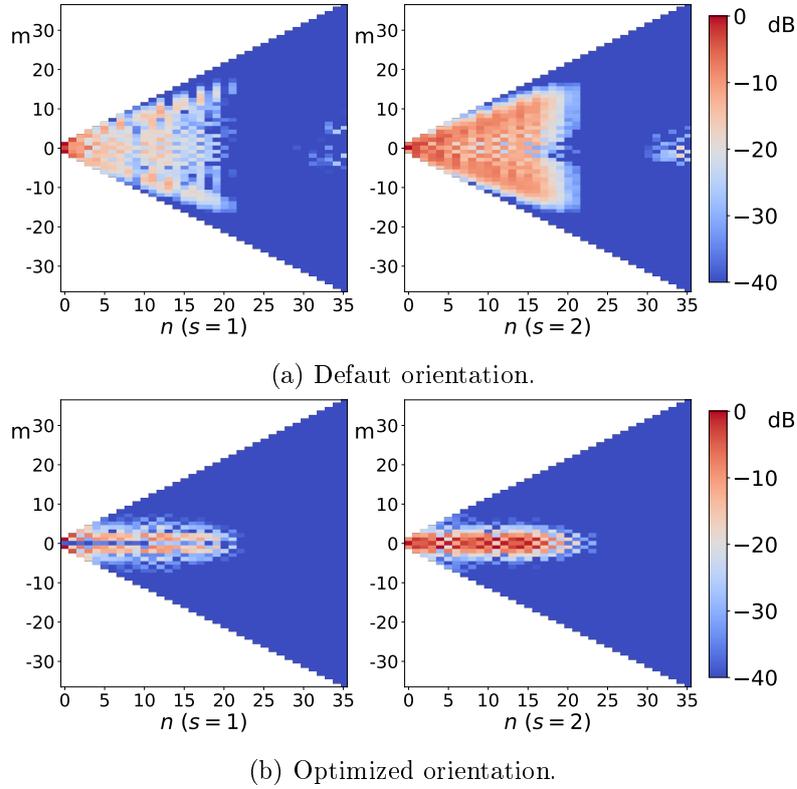(a) Defaut orientation.

(b) Optimized orientation.

Figure III.24: Normalized spherical coefficients of the waveguide array simulated at 50 GHz.

After running the proposed optimization procedure, the estimated rotation angles are $\theta_0 = 45°$ and $\chi_0 = 55°$. We observe at the right part of the spectrum in Fig III.24.a that raw data produces some high frequency modes which are not physically realistic and are due to the too low density sampling rate. The optimized rotation induces a significant reduction of the significant spherical coefficients and consequently the non-physical high frequency modes vanish. The reference far field is illustrated in Fig. III.25 with a specific cutting plane. The optimized pattern better fits the one of reference than the raw pattern. The effective sparsities are $k_T = 33\%$ and 15% for the raw and rotated fields respectively with corresponding EES values of -36.6 dB and -53.4 dB.

III.5.d   Validation on far-field measurements

Let us now validate the procedure using antenna far-field measurements. Three antennas are investigated: a Luneburg lens antenna, a Radiating Cavity Antenna (RCA) and a ReflectArray (RA). The Table III.2 gathers information about the presented cases in this section. For each antenna, a cartography of the pattern and the position of the optical axis $\mathbf{z}'$ of the optimized rotated coordinate system is shown in Fig. III.26. The reconstruction results are reported in Table III.3.
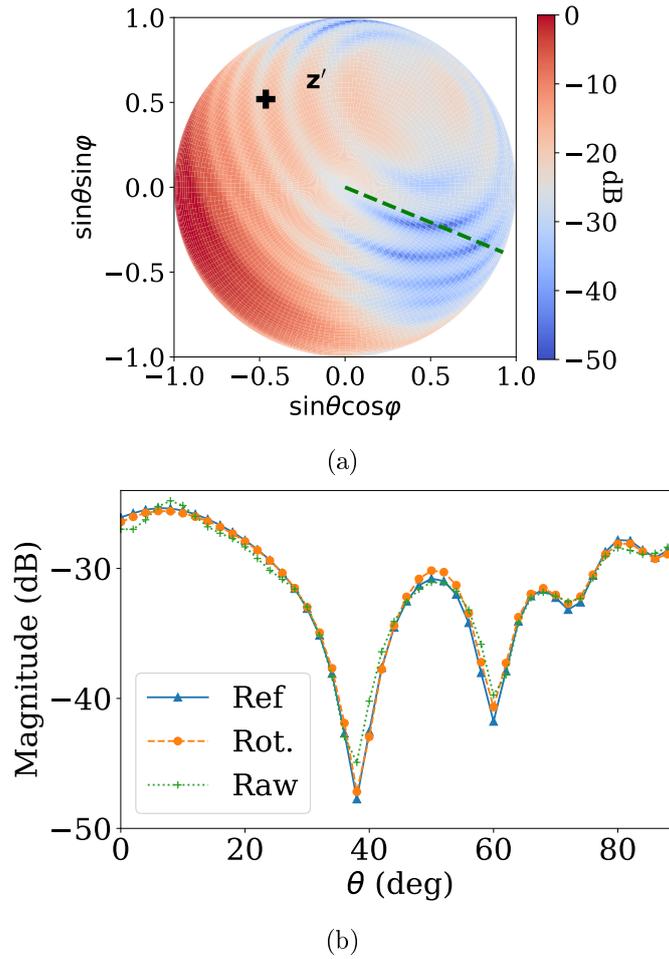
(a)

(b)

Figure III.25: (a) Normalized electric far field radiated by the waveguide array at $50\,\text{GHz}$ ($\mathbf{z}'$ chosen by GP) and (b) the cutplane represented by the green doted line in.

Table III.2: Characteristics of the investigated antenna measurements:

Antenna	Size $a(\lambda)$	Coef. N_c	Meas. set	Subsample
Lens 12 GHz	6	4606	9746	3702
RCA 6 GHz	2.6	1456	2332	1088
RA 12 GHz	6	4606	10970	2628

Methodology

All measurements have been carried out in the two far-field anechoic chambers of the M^{2}ARS facilities at IETR. Both are equipped with a roll-over-azimuth positioning system where the AUT is placed and a roll axis enables to change the polarization of the probe. The field is acquired step by step with a high density sampling rate following an *igloo* strategy to avoid the oversampling near the poles, providing our reference patterns. As in near-field validations, we select a coarse *igloo* sampling to emulate a fast measurement data set. The resulting interpolated field is derived from the spherical coefficients identified by BPDN and compared with the reference pattern. The GP interpolation is done with the same parameters as in near field.
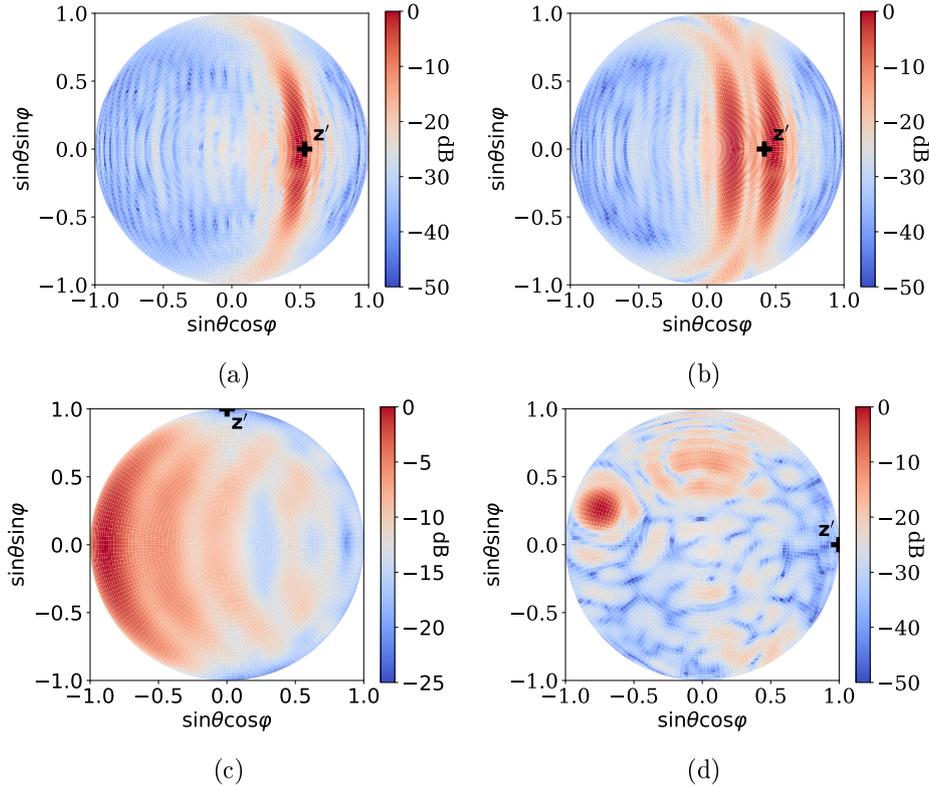
Figure III.26: Normalized electric far-fields radiated by: (a) the single beam Luneburg lens antenna at $12\,\mathrm{GHz}$, (b) the dual beam version, (c) the radiating cavity antenna at $6\,\mathrm{GHz}$ and (d) the reflectarray at $12\,\mathrm{GHz}$. Cross markers $\mathbf{z}'$ are the position of the z-axis after the rotation optimized by Gaussian processes.

Luneburg Lens Antenna at $12\,\mathrm{GHz}$

The flat Luneburg lens antenna is fed by several waveguides [25] and measured over the full sphere. We investigate two configurations: one excited waveguide generating one beam and two excited waveguides radiating two beams. The resulting reference far fields are shown in Fig. III.26a and III.26b.

Lens with single beam The 3D far-field pattern is displayed in Fig. III.26a. We note that the procedure chooses to orientate the z'-axis at the maximum of the field. Spherical coefficients are displayed in Fig. III.27b, we clearly observe less significant coefficients for the rotated field expansion with the proposed approach than the defaut orientation. The result of the SOA method is different. The rotation is done such that a symmetry with respect to the equator of the radiation pattern is achieved, explaining the peculiar spectrum in Fig. III.27a.

Lens with dual beam We generate this case from two single beam measurements. The radiation pattern is shown in Fig. III.26b. The two beams nearly have the same magnitude, and the z'-axis is not located at a maximum magnitude point this time. However, the SOA method returns the same result as the single beam case for the same reason involving the symmetry around the equator.
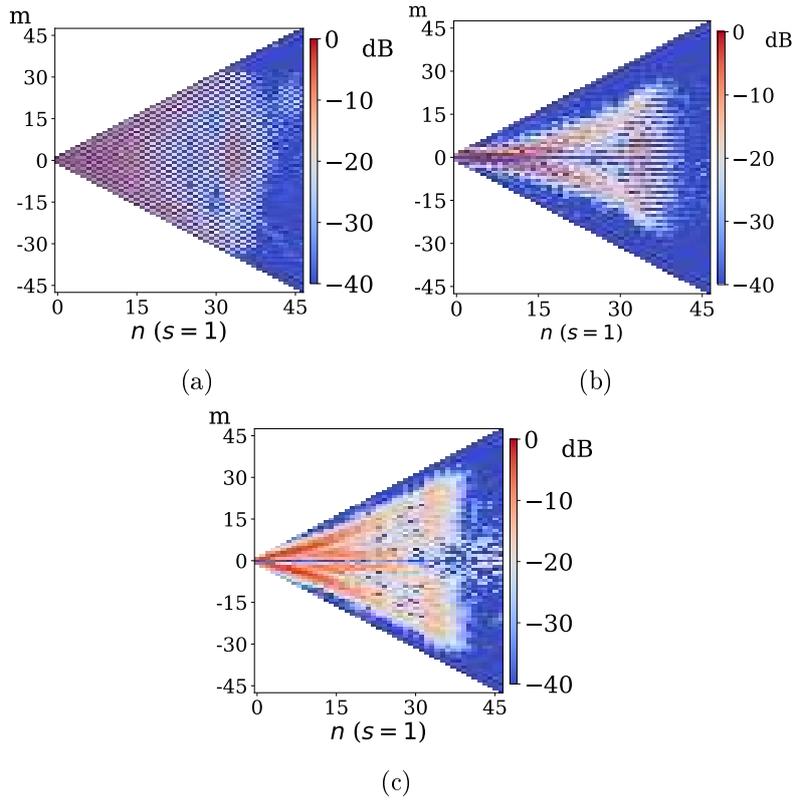
(a)

(b)

(c)

Figure III.27: Normalized spherical coefficients for $s = 1$ of the Luneburg Lens antenna with single beam for the angles found by (a) the SOA method, (b) the proposed approach and (c) default position.

Radiating Cavity Antenna at $6\,\mathrm{GHz}$

The AUT is measured over the full sphere and is designed for Car 2 X (C2X) communications. The reference electric far field is illustrated in Fig. III.26c. This antenna has a small dynamic range, as the measured magnitudes of the electric far field vary from 0 to $-25\,\mathrm{dB}$. The best rotation angles determined by GP, indicated by the cross marker in Fig. III.26c, are the same as the SOA method. After performing this rotation, the number of significant coefficients is halved, as shown in Table III.3.

Reflectarray at $12\,\mathrm{GHz}$

The field of the reflectarray is illustrated in Fig. III.26d. It has a very directive pattern with a tilted beam and the measurement is carried out over an hemisphere. Because of this, the optimization has led to an orientation axis on the equator so the pattern complexity mostly concerns by the φ coordinate.

III.5.e Discussion

Reconstruction accuracy

In all cases, the sparsity of the spherical coefficients is greater or equal than the one of the SOA method. This enhanced sparsity leads to an improvement of the field reconstruction as illustrated by the values of EES in Table III.3. The choice of rotation angles is not trivial

for most cases and cannot be easily predicted in advance, as shown by the $\mathbf{z}'$ markers in the far-field mappings in Fig. III.26.

Impact of the mode distribution

The rotation of the radiated field by the single beam lens at $12\,\text{GHz}$ in Fig. III.26a by $(\varphi_0, \theta_0, \chi_0) = (0, 90, 90)$ in degrees places the main beam orthogonal to the equator. In such configuration, the field is symmetric with respect to the equator and the spherical spectrum is concentrated in the modes $\mathbf{F}_{smn}$ such that $m + n$ is even. Moreover, the sparsity is greatly promoted, explaining the specific spectrum shown in Fig. III.27a. This sparsity increase is achieved at a cost of pushing some modes to higher order ones (further from the line $m = 0$), which are harder to identify with undersampled sets. This case will lead to a sudden variation of the effective sparsity, which is noticeable using our approach. For the RCA case, both methods yield a symmetry with respect to the equator. However, due to the small directivity of the pattern, shown in Fig. III.26c, there is no creation of high order modes as in the previous case.

Considering the reflectarray case, the SOA method fails to detect the rotation angles leading to the sparsest expansion. This can be explained by the relatively low number of samples with respect to the number of unknowns since this method optimizes the rotation using the spherical coefficients found along the default orientation.

Computation time

The computation time is difficult to estimate for the SOA method. Indeed, several initialization points must be tested to ensure a proper optimization, it requires the computation of multiple rotation matrix per iteration, being at least as costly as solving the BPDN with SPGL1. The convergence speeds highly depends on the proper tuning of several parameters, which is no trivial matter. The proposed approach takes less than 3 minutes of computation with an Intel i7-8700 and 16 GB RAM for all investigated examples.

Minimization accuracy

The angular distance between our procedure and a brute force approach (successive refinements of a dense testing grid around the expected minima up to 0.2°) of the optimized rotation angles is lower than 2.5° for all the presented measurements. The corresponding effective sparsities k_{-40} and EES values show differences of 2 % and 0.14 dB in the worst case.

Table III.3: EES Values, Corresponding Effective Sparsities k_{-40}:

	k_{-40} (%)			EES (dB)		
Antenna	Raw	SOA	GP	Raw	SOA	GP
Lens (single)	62	43	41	-46.9	-50.0	-51.2
Lens (double)	58	37	37	-43.6	-48.3	-49.3
RCA	33	15	15	-37.2	-39.0	-39.1
RA	40	40	29	-48.0	-48.0	-50.9

III.6   Antenna positioning procedure

The combination of the antenna position and orientation search methods, in this order, leads to a full positioning optimization algorithm. This complete procedure is demonstrated using the measurement of a horn at 10 GHz into the MVG multi-probe system StarLab [26]. The horn has been measured at two different positions, illustrated in Fig. III.28: the nominal one (the horn is centered at best for performing the measurement), the shifted one (the horn is translated by a vector $(3\lambda, 0, 3\lambda)$ with respect to the nominal position).

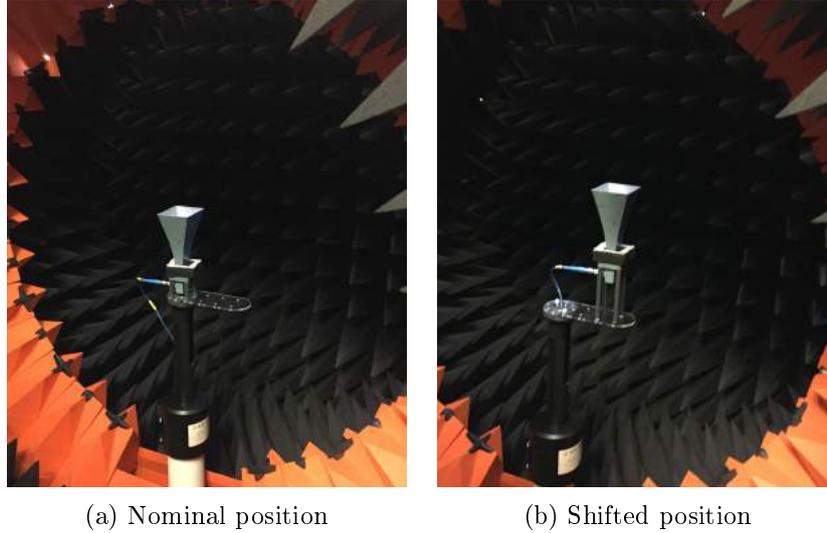(a) Nominal position   (b) Shifted position

Figure III.28: The horn at 10 GHz in the MVG StarLab.

The field samples used for optimization are derived from the spherical coefficients returned by the MVG software, which are shown in Fig. III.29. The truncation order of the SW is set to $N = 56$, using the minimal sphere for the shifted horn, or equivalently 6496 coefficients. The field samples are derived in the far field over an igloo sampling on the full sphere from the spherical coefficients. This sample set has a size of 4036 (or 2018 sampling positions times 2 polarizations). This choice leads to a quite significant under-determinated linear system of equations for the shifted horn, emulating a fast measurement procedure.

(a) Nominal position   (b) Shifted position
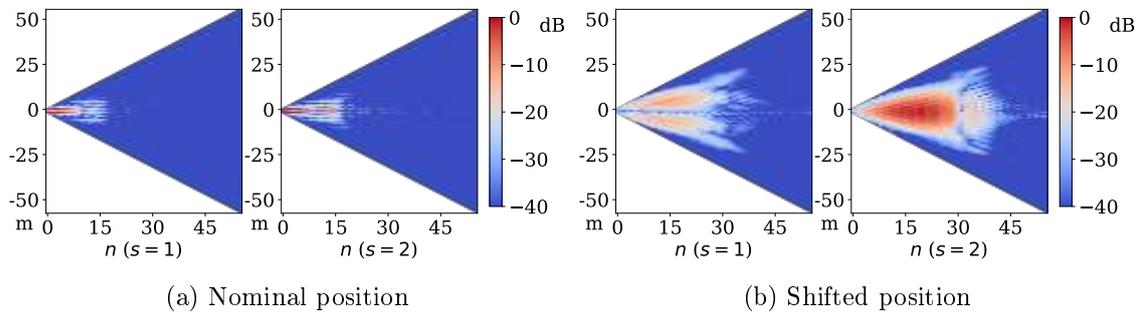
Figure III.29: Normalized spherical coefficients of the horn at 10 GHz returned by the MVG software.

The positioning of the horn is optimized in the far field. The spherical coefficients retrieved from the fast measurement sample are shown in Fig. III.30. The fast sampling

induces identification problem over the high degree part of the spectrum. These effects are completely negated by the optimization process, as shown by the spherical coefficients in Fig. III.30.c. The obtained spectrum is even more compact than the one in its nominal position in the measurement system, in Fig. III.29.a. In this case, it leads to orientation angles $(\theta_0, \chi_0) = (-90, 90)°$. The full process allows a significant reduction of the significant spherical coefficients: from 37 % to 4 %.
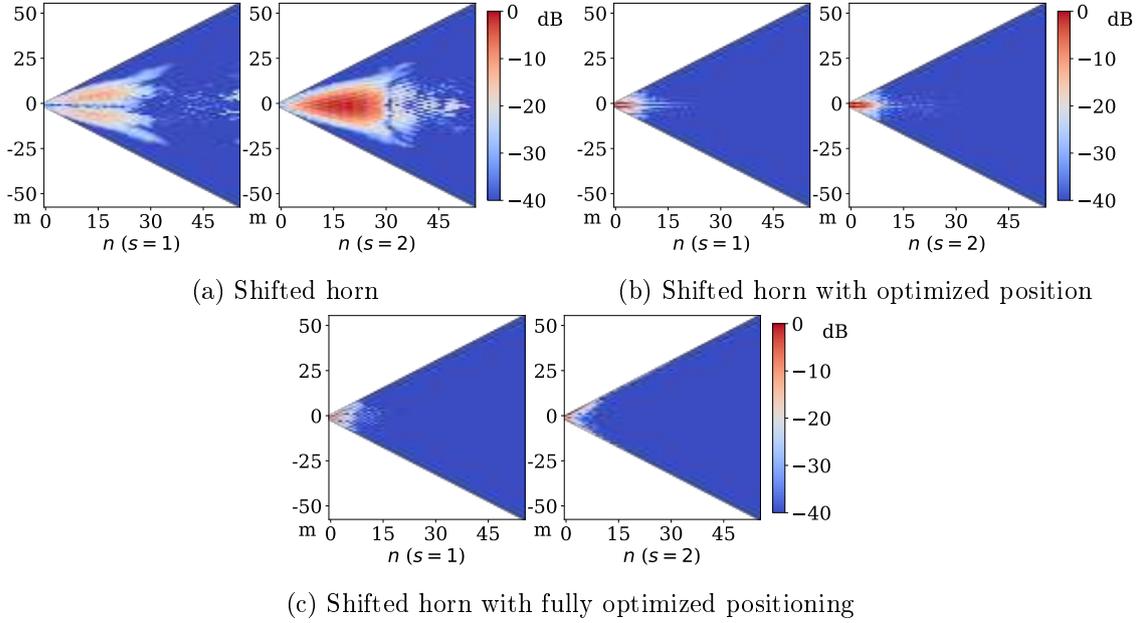

(a) Shifted horn   (b) Shifted horn with optimized position

(c) Shifted horn with fully optimized positioning

Figure III.30: Normalized spherical coefficients of the horn at 10 GHz identified using the fast measurement field sample.

(a) Shifted horn   (b) Shifted horn with optimized position
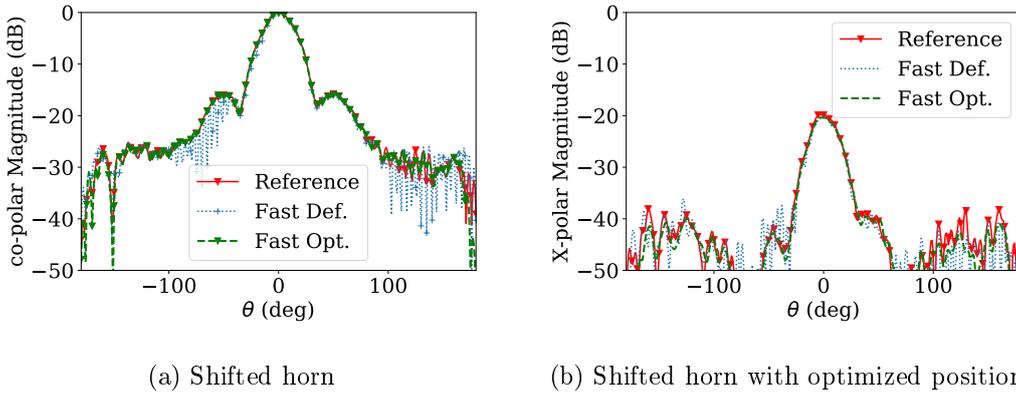
Figure III.31: Normalized reconstructed field magnitudes of the horn at 10 GHz at the shifted position.

The reconstruction results over the main cutting plane $\varphi = 0°$ are shown in Fig. III.31 for the normalized magnitude and III.32 for the phase. As illustrated, the agreement with the reference, the field reconstructed by the spherical coefficients returned by the MVG software, is greatly improved after the positioning optimization. The phase is also smoother after the optimization of the positioning. This means that the optimization of the position if connected to the estimation of the radiation center, as hinted by [27].
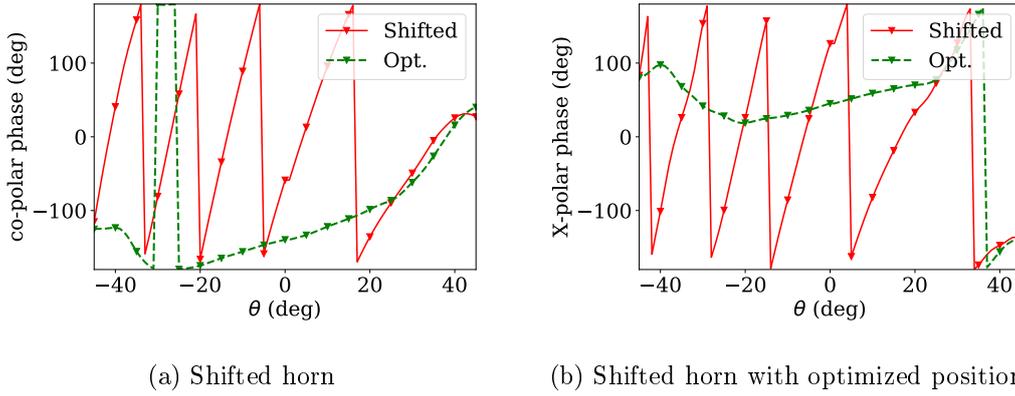
(a) Shifted horn   (b) Shifted horn with optimized position

Figure III.32: Normalized reconstructed field phases of the horn at 10 GHz at the shifted position.

III.7 Conclusion

A procedure that processes radiation pattern measurements so as to find the *best* position of the AUT has been proposed. The underlying idea is to exploit as much as possible the valuable information encompassed in the SW spectrum of the antenna. By properly translating the antenna with respect to the measurement coordinate system, it is possible to concentrate the power of its spectrum to low frequency content. For that purpose, a metric based on the n-spectrum has been developed and integrated to an efficient optimization strategy. The proposed approach induces not only lower truncation orders for the SW series but also better 3D radiation pattern reconstructions. It also diminishes the impact of an eventually bad AUT positioning in terms of power distribution among the spectrum.

An efficient procedure using rotations of the measured antenna patterns for generating a sparser expansion of the field has also been developed. This post-processing method is valid for spherical near and far-field antenna characterization with low sampling rates. It does not require extra measurement nor modification It allows to exploit at best the information contained in a given undersampled field dataset. In addition, the proposed approach is applicable to any type of spherical sampling strategy.

Both antenna position and rotation methods have been validated using numerical and experimental data in near and far field. The joint optimization of the antenna position and rotation provides a complete antenna positioning procedure that has been experimentally validated using a commercial antenna measurement system, the MVG StarLab multi-probe system.

Bibliography

[1] F. Jensen and A. Frandsen. On the number of modes in spherical wave expansions. In *AMTA 2004*, 10.

[2] F. D'Agostino, F. Ferrara, C. Gennarelli, R. Guerriero, and M. Migliozzi. Reconstruction of the far field radiated by an offset mounted volumetric aut from non-redundant spherical spiral near-field measurements. *IET Microwaves, Antennas Propagation*, 14(14):1711–1718, 2020.

[3] L. J. Foged, F. Saccardi, F. Mioc, and P. O. Iversen. Spherical near field offset measurements using downsampled acquisition and advanced nf/ff transformation algorithm. In *2016 10th European Conference on Antennas and Propagation (EuCAP)*, pages 1–3, 2016.

[4] F. Rodriguez-Varela, B. Galocha-Iraguen, and M. Sierra-Castañer. Fast spherical near-field to far-field transformation for offset-mounted antenna measurements. *IEEE Antennas and Wireless Propagation Letters*, 2020.

[5] R. Cornelius and D. Heberling. Spherical wave expansion with arbitrary origin for near-field antenna measurements. *IEEE Trans. on Antennas and Propag.*, 65(8):4385–4388, Aug 2017.

[6] D. Loschenbrand and C. Mecklenbrauker. Fast antenna characterization via a sparse spherical multipole expansion. Aachen, 2016. 4th International Workshop on Compressed Sensing Theory and its Applications to Radar, Sonar and Remote.

[7] D. L. Donoho and J. Tanner. Precise undersampling theorems. *Proceedings of the IEEE*, 98(6):913–924, June 2010.

[8] C. Culotta-Lopez, D. Heberling, A. Bangun, A. Behboodi, and R. Mathar. A compressed sampling for spherical near-field measurements. In *AMTA 2018*, Williamsburg Virginia, USA, November 2018.

[9] B. Fuchs, L. Le Coq, S. Rondineau, and M.D. Migliore. Fast antenna far field characterization via sparse spherical harmonic expansion. *IEEE Trans. on Antennas and Propag.*, 65(10):5503–5510, Oct. 2017.

[10] B. Hofmann, O. Neitz, and T. Eibert. On the minimum number of samples for sparse recovery in spherical antenna near-field measurements. *IEEE Trans. on Antennas and Propag.*, 67(12):7597–7610, 2019.

[11] N. Mézières, B. Fuchs, L. Le Coq, J.-M. Lerat, R. Contreres, and G. Le Fur. On the application of sparse spherical harmonic expansion for fast antenna far field measurements. *IEEE Antennas and Wireless Propagation Letters*, 2020.

[12] C. Culotta-Lopez, K. Wu, and D. Heberling. Radiation center estimation from near-field data using a direct and an iterative approach. In *AMTA 2017*, pages 1–6, Oct 2017.

[13] J. Hald, J.E. Hansen, F. Jensen, and F.H. Larsen. *Spherical Near Field Antenna Measurements*. Peter Peregrinus, 1988.

[14] A. R. EDMONDS. *Angular Momentum in Quantum Mechanics*. Princeton University Press, 1985.

[15] C. A. Balanis. *Antenna Theory: Analysis and Design*. Wiley-Interscience, 2005.

[16] S. McBride, D. Tammen, and W. Hess. Best-fit 3d phase-center determination and adjusment. In *AMTA 2013*. NSI-MI Technologies.

[17] HFSS. Ansys. Available at https://www.ansys.com/products/electronics/ansys-hfss.

[18] Cst studio suite 2020. Technical report, Dassault Systèmes. Available at https://www.3ds.com/fr/produits-et-services/simulia/produits/cst-studio-suite/.

[19] R. Fragnier, L. Feat, R. Contreres, B. Palacin, K. Elis, A. Bellion, and G. L. Fur. Collocated compact uhf and l-band antenna for nanosatellite argos program. In *2019 13th European Conference on Antennas and Propagation (EuCAP)*, 2019.

[20] A. Dorlé, R. Gillard, E. Menargues, M. v. der Vorst, E. de Rijk, P. Martín-Iglesias, and M. García-Vigueras. Sidelobe level reduction in ridged leaky waveguide through stereolithography. In *2019 13th European Conference on Antennas and Propagation (EuCAP)*, pages 1–5, 2019.

[21] N. Mézières, B. Fuchs, L. Le Coq, J.M. Lerat, R. Contreres, and G. Le Fur. Fast antenna characterization improvement by pattern rotation. *IEEE Trans. on Antennas and Propag.*, 69(5):2952–2957, 2021.

[22] B. Aqlan, M. Himdi, L. Le Coq, and H. Vettikalladi. Sub-thz circularly polarized horn antenna using wire electrical discharge machining for 6g wireless communications. *IEEE Access*, 8:117245–117252, 2020.

[23] J. Fridén and G. Kristensson. Calculation of antenna radiation center using angular momentum. *IEEE Trans. on Antennas and Propag.*, 61(12):5923–5930, 2013.

[24] C. Rasmussen and C. K. I. Williams. *Gaussian Processes for Machine Learning (Adaptive Computation and Machine Learning)*. The MIT Press, 2005.

[25] C.D. Diallo. *Study and Design of new Multibeam Antenna Architectures in Ku and Ka Bands for Broadband Satellite Communication Applications*. PhD thesis, University of Rennes 1, 2016.

[26] Starlab 650MHz-18GHz. MVG, 2020. Available at https://www.mvg-world.com/fr/products/antenna-measurement/multi-probe-systems/starlab.

[27] C. Culotta-Lopez, K. Wu, and D. Heberling. Radiation center estimation from near-field data using a direct and an iterative approach. In *AMTA 2017*, pages 1–6, 2017.

Chapter IV

Antenna characterization via reduced-order model

IV.1 Introduction

IV.1.a Motivations

The fields radiated by antennas of finite sizes can be expanded using truncated series [1, 2]. The choice of the basis functions to perform this expansion depends on available *a priori* information about the antenna (e.g. shape, maximum electrical length), the measurement surface (planar, spherical, cylindrical) and has an impact on the number of field samples required for its characterization. The expansion into Spherical Waves (SW) is a widely spread choice in the antenna measurement community and its exploitation has been addressed in Chapters II and III. The number of field samples to properly expand the radiation of antennas into SW functions is tied to the radius of the minimal sphere enclosing the sources. However, most antennas can be better described by other shapes than a sphere, such as boxes/parallelepipeds or cylinders. The use of shapes tailored to the AUT geometry combined with the numerical construction of appropriated basis functions should lead to a reduction of the number of field samples required to represent the antenna radiation pattern.

IV.1.b State of the art

The use of non-spherical surfaces to expand the field radiated by antennas and thereby reduce the number of required field samples has been proposed and successfully validated by Prof. Bucci *et al.* [2–5]. These basis functions better fit the true shape of the AUT by enclosing it in convex surfaces with a symmetry of revolution. More importantly and despite the geometrical limitations imposed by the use of analytical basis functions, this fundamental and pioneer work ensures the minimal number of samples to reconstruct the radiated field. Nevertheless, the truncation error of such a field expansion is not clearly controlled even if an oversampling factor is added to mitigate this problem.

Instead of using analytical basis functions, recent works combine strong *a priori* knowledge and even numerical simulations of the AUT in order to expedite its characterization. Full-wave electromagnetic simulations of the structure can be used to build either a compressed [6] or an overcomplete [7] representation of the radiated fields, enabling the reconstruction of the AUT radiation pattern from a small number of field samples. When

the prior knowledge about the AUT is very strong, both strategies are very efficient and lead to fast antenna testing. The illustration of the fast antenna characterization of a reflector antenna presented in [6] is given in Fig. IV.1. Simulations of a reflector antenna have been performed for various positions and orientations of the feed/reflector, leading to the construction of a basis enabling a reduced number of samples.
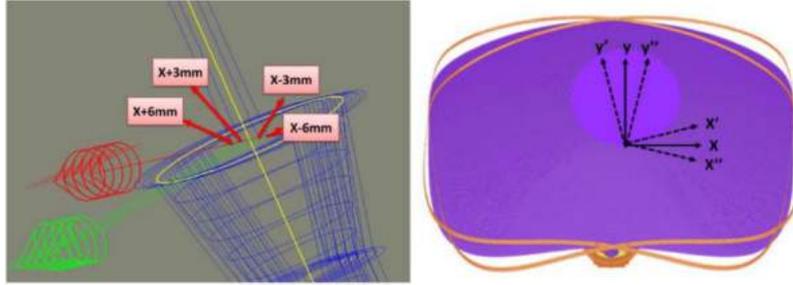
(a) Perturbations on the feed and reflector positions.
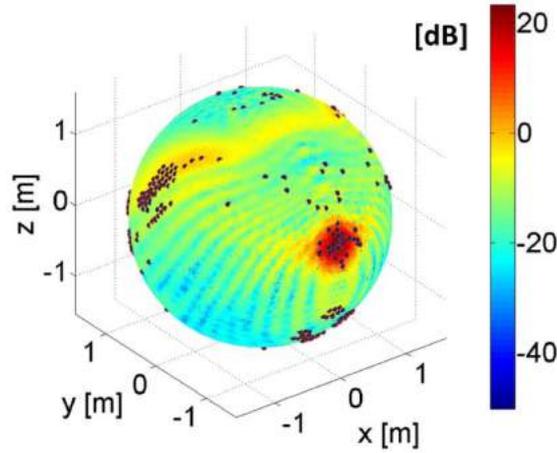
(b) Reduced spherical sampling (red dots).

Figure IV.1: Fast antenna characterization using simulations of the AUT [6].

Finally, the construction and use of reduced-order models to speed up antenna characterization is relatively new. Initially proposed to efficiently characterize the radar cross section of targets [8], this approach has been adapted in [9] to bring down the number of samples for the characterization of antennas. The construction of the reduced order model requires to know the AUT outer dimensions and the measurement surface geometry. This reduced-order model can be derived from the radiation matrix, which is usually rather used to back-propagate the field for antenna diagnostic [10–12] or spatial filtering purposes [13].

IV.1.c Contributions

This work extends the preliminary investigations on the use of reduced order models for fast antenna characterization [9], enabling the derivation of a minimum far-field sampling criterion. It has been carried out in collaboration with Prof. M. Mattes from the DTU. The rigorous construction of the radiation matrix that maps the equivalent currents on a meshed surface surrounding the AUT to its radiated field is described. The approximation of this matrix up to the measurement accuracy is achieved by truncating its singular value decomposition accordingly. This methodology enables to build numerically a compressed

basis that is customized to our antenna characterization problem. The dimension of this basis and consequently the number of field samples is shown to be determined by the area of the equivalent current surface over the squared wavelength. This result is in agreement and somehow generalizes the fundamental works on the minimum non-redundant sampling [5]. Various numerical and experimental examples of the characterization of AUT validate the proposed reduced-order model approach.

IV.2 Radiation matrix for antenna characterization

The construction and discretization of the radiation operator that maps the equivalent currents on the surface enclosing the AUT to the radiated field are addressed in this section.

IV.2.a Huygens' equivalence principle

In electromagnetics, the fields $(\mathbf{E}, \mathbf{H})$ radiated by a set of finite sources $(\mathbf{J}, \mathbf{M})$ can be described by equivalent surface electric and magnetic current distributions that represent the tangential magnetic and electric fields, respectively [14]. This equivalence principle, also known as Huygens' principle, states that the field emitted from the AUT enclosed by a surface Σ is also radiated by equivalent surface currents $(\mathbf{J}_{eq}, \mathbf{M}_{eq})$ over Σ, as shown in Fig. IV.2.
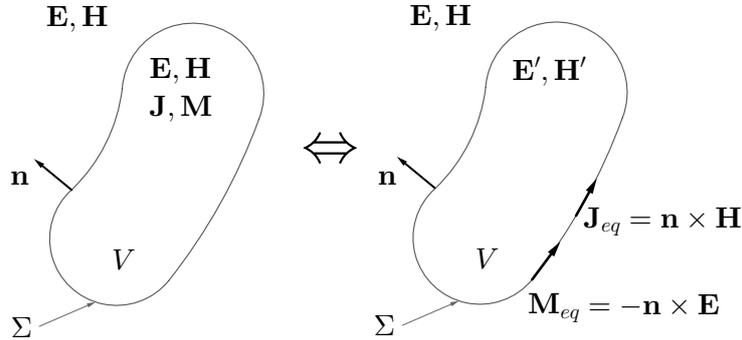

Figure IV.2: Surface equivalence principle: the original problem (left) can be replaced by an equivalent one (right). The electromagnetic field $(\mathbf{E}, \mathbf{H})$ outside a volume V enclosed by a surface Σ containing all the sources is radiated by equivalent current distributions $\mathbf{J}_{eq} = \mathbf{n} \times \mathbf{H}, \mathbf{M}_{eq} = \mathbf{E} \times \mathbf{n}$ over Σ, the vector $\mathbf{n}$ being its exterior normal vector.

There are different variants of the surface equivalence principle depending on the constraints imposed on the internal fields $\mathbf{E}'$ and $\mathbf{H}'$ of the equivalent model, as shown in Fig. IV.2. The Love's formulation, also known as zero internal fields constraint, for which $\mathbf{E}' \equiv 0 \equiv \mathbf{H}'$, has been shown to provide realistic current distributions [11, 15], which is extremely relevant for diagnostic purposes. Besides, note that the use of only one type of equivalent current ($\mathbf{J}_{eq}$ or $\mathbf{M}_{eq}$) suffices provided that the volume V is filled with either a perfect magnetic or electric conductor, respectively.

The goal of this chapter is to interpolate at best the electric far field radiated by the AUT enclosed by Σ. Therefore, we leave the internal fields $\mathbf{E}'$ and $\mathbf{H}'$ unconstrained and use both types of equivalent currents, as suggested in [13].

IV.2.b   Boundary integral equation

The electric field radiated by the equivalent surface currents $(\mathbf{J}_{eq}, \mathbf{M}_{eq})$ on Σ into a source-free region, characterized by its permeability μ and permittivity ε and employing the Lorenz gauge, is given by

$$
\begin{aligned}
\mathbf{E}(\mathbf{r}) = \ & j\omega\mu \int_{\Sigma} g(\mathbf{r}, \mathbf{r}')\mathbf{J}_{eq}(\mathbf{r}')d\sigma' \\
& - \frac{1}{j\omega\varepsilon} \int_{\Sigma} \mathbf{grad_r} g(\mathbf{r}, \mathbf{r}')\mathrm{div}\,\mathbf{J}_{eq}(\mathbf{r}')d\sigma' \\
& - \int_{\Sigma} \mathbf{rot_r}\big(g(\mathbf{r}, \mathbf{r}')\mathbf{M}_{eq}(\mathbf{r}')\big)d\sigma'
\end{aligned}
\tag{IV.1}
$$

where ω is the angular frequency and g the scalar free-space Green function, given by $g(\mathbf{r}, \mathbf{r}') = \frac{e^{-jk|\mathbf{r}-\mathbf{r}'|}}{4\pi|\mathbf{r}-\mathbf{r}'|}$. The vector $\mathbf{r}$ is the observation point and $\mathbf{r}'$ is the one used for the integration over Σ, sometimes called the source vector. The positive time convention $e^{j\omega t}$ has been used. The notations $\mathbf{grad_r}$ and $\mathbf{rot_r}$ mean that these operators are applied with respect to the observation position $\mathbf{r}$ only. The equation IV.1 is valid for all observation points $\mathbf{r}$ outside the volume V delimited by Σ.

IV.2.c   Boundary element method

The goal is to determine the equivalent current distributions $(\mathbf{J}_{eq}, \mathbf{M}_{eq})$ that are tangential to the surface Σ. These currents radiate the same field as the sources $(\mathbf{J}, \mathbf{M})$ contained in the volume V. We assume that these surface currents can be expanded into a set of known basis functions $\mathbf{f}_k, k = 1, \ldots, K$ defined over Σ:

$$
\begin{aligned}
\mathbf{J}_{eq}(\mathbf{r}') &= \sum_{k=1}^{K} \mathrm{j}_k \mathbf{f}_k(\mathbf{r}'), \\
\mathbf{M}_{eq}(\mathbf{r}') &= \eta \sum_{k=1}^{K} \mathrm{m}_k \mathbf{f}_k(\mathbf{r}').
\end{aligned}
\tag{IV.2}
$$

where j_k and m_k are the complex coefficients to be determined. Note that the equivalent magnetic current is multiplied by the wave impedance η so that both currents $(\mathbf{J}_{eq}, \mathbf{M}_{eq})$ have the same order of magnitude, as often advocated [11].

The current expansions (IV.2) enable to cast the surface integrals (IV.1) into a weighted sum of integrals of the known basis functions. Thus, the contribution of the basis function $\mathbf{f}_k$ to the radiated field, denoted $\mathbf{E}_k$, is given by:

$$
\begin{aligned}
\mathbf{E}_k(\mathbf{r}) = \ & \mathrm{j}_k \left[j\omega\mu \int_{\Sigma} g(\mathbf{r}, \mathbf{r}')\mathbf{f}_k(\mathbf{r}')d\sigma' \right. \\
& \left. - \frac{1}{j\omega\varepsilon} \int_{\Sigma} \mathbf{grad_r} g(\mathbf{r}, \mathbf{r}')\mathrm{div}\,\mathbf{f}_k(\mathbf{r}')d\sigma' \right] \\
& - \eta\mathrm{m}_k \int_{\Sigma} \mathbf{rot_r}\big(g(\mathbf{r}, \mathbf{r}')\mathbf{f}_k(\mathbf{r}')\big)d\sigma'.
\end{aligned}
\tag{IV.3}
$$

By doing so, the original integral equation (IV.1) is approximated by an easier to solve coefficient identification problem, where the unknowns are the weights j_k and m_k.

IV.2.d Radiation matrix construction

The boundary element method can be implemented in various manners. Our choices regarding the basis functions $\mathbf{f}_k$, the numerical integration rule and the matrix construction are now given.

Linear square elements

The equivalent surface Σ has first been approximated by square cells. The basis functions are then defined by a couple of adjacent square cells. In each cell, the current flows in the two directions determined by each couple of parallel edges, as displayed in Fig. IV.3.
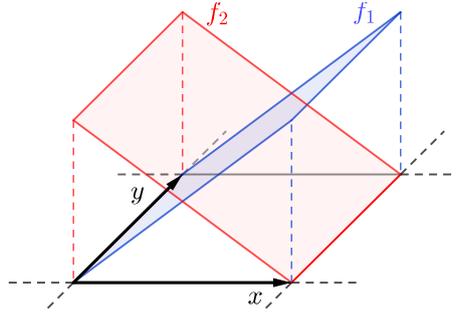

Figure IV.3: Illustration of two basis functions $\mathbf{f}_1$ and $\mathbf{f}_2$ in one direction and one square cell.

Triangular cells and RWG basis functions

The equivalent surface Σ can also be approximated by triangles. This choice provides a greater flexibility to approximate a given surface than the use of square cells as triangular ones indeed enable to better fit curved surfaces (such as spheres or cylinders) than square cells. The Rao-Wilton-Glisson (RWG) [16] basis functions are a widely spread choice for its ease of computation while ensuring continuous normal fluxes across the common edge of two adjacent triangles. Each couple of adjacent triangles, sharing an edge, defines a basis function, as illustrated in Fig. IV.4, given by

$$\mathbf{f}(\mathbf{r}) = \begin{cases} \frac{\ell}{2A^+}\mathbf{r}^+ & \text{if } \mathbf{r} \in T^+ \\ -\frac{\ell}{2A^-}\mathbf{r}^- & \text{if } \mathbf{r} \in T^- \\ 0 & \text{otherwise} \end{cases} \tag{IV.4}$$

where $A^\pm$ are the areas of the triangles $T^\pm$, respectively, and $\mathbf{r}^\pm$ the position vectors from the vertices of each triangle that are opposite to the common edge. Note that three elements are required per triangle cell instead of four in the case of square cells.

Numerical integration

Each integral term in (IV.3) is approximated for a given observation position $\mathbf{r}$ using the Gauss-Legendre quadrature rule. The 9-point version of the quadrature rule is used as given in [17], either for triangles when using RWG functions or for square when using square cells. These quadratures rules are illustrated in Fig, IV.5. In our antenna measurement context,
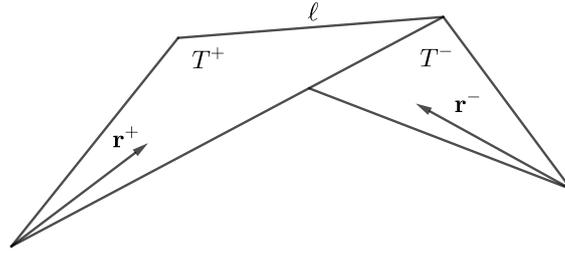
Figure IV.4: Illustration of the support of a RWG basis function: ℓ is the length of the common edge, $T^{\pm}$ denote the two triangles and $\mathbf{r}^{\pm}$ the position vectors from the vertices opposite to the common edge. A positive current is chosen to flow from T^+ to T^-.

the observation point $\mathbf{r}$ is always far enough from the equivalent surface Σ and thus from $\mathbf{r}'$. Consequently, each term of (IV.3) is well-defined as singularities are avoided. Hence, the integrands are smooth enough for the Gauss-Legendre quadrature to be sufficient for an accurate approximation of the integrals.
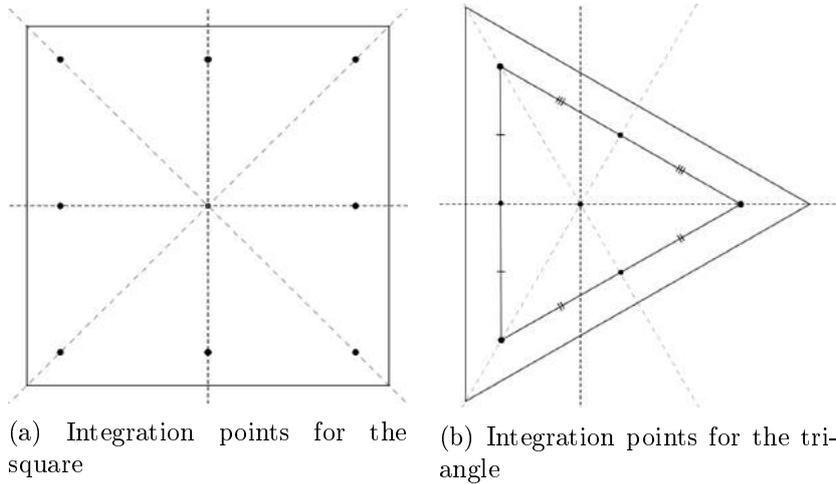

(a) Integration points for the square

(b) Integration points for the triangle

Figure IV.5: Gauss-Legendre quadrature rules for the square and the equilateral triangle with 9 points.

The integrals of a given function f over these domains are then approximated by a sum of weighted evaluations of f at the points of the quadrature [17], as follows

$$\int_S f(x,y)dxdy \approx \sum_{l=1}^{9} \omega_l f(x_l) \tag{IV.5}$$

where S is a cell of the mesh, either a square or a triangle, x_l are the points displayed in Fig. IV.5 and ω_l are the corresponding weights of the Gauss-Legendre quadrature. For the square, they are simply defined as $\omega_l = 16/81$.

Matrix formulation

The equation (IV.3) is valid for any observation point $\mathbf{r}$ in the external region (outside V). Let us consider a set $\mathbf{r}_m$ of M observation points. The equation (IV.1) can be approximated

and formulated in Cartesian coordinates as follows

$$\begin{bmatrix} \mathbf{E}_x \\ \mathbf{E}_y \\ \mathbf{E}_z \end{bmatrix} = \begin{bmatrix} \mathbf{A}_{J,x} & \eta\mathbf{A}_{M,x} \\ \mathbf{A}_{J,y} & \eta\mathbf{A}_{M,y} \\ \mathbf{A}_{J,z} & \eta\mathbf{A}_{M,z} \end{bmatrix} \begin{bmatrix} \mathbf{j} \\ \mathbf{m} \end{bmatrix} \tag{IV.6}$$

where $\mathbf{E}_x$ contains the x-component of $\mathbf{E}$ at the observation positions $\mathbf{r}_m$, $\mathbf{A}_{J,x}$ the x-component of the electric current distribution in the equation (IV.3) for each basis functions $\mathbf{f}_k$, $\mathbf{A}_{M,x}$ is the same for the magnetic current distribution. The other components y and z are defined similarly. Finally, the vectors $\mathbf{j}$ and $\mathbf{m}$ gather all the coefficients of the equivalent currents, j_k and m_k, to be determined. Systems of equations similar to (IV.6) can be easily derived when other vector field representations are used.

In the sequel, the system (IV.6) is denoted by $\mathbf{y} = \mathbf{A}\mathbf{x}$, where the vector $\mathbf{y}$ contains the measured field, $\mathbf{A}$ is the discretized radiation operator and $\mathbf{x}$ the equivalent currents.

IV.2.e   Numerical examples

A few examples of reconstructions of equivalent currents are shown to illustrate and validate the code developed during the thesis. These numerical examples use the theoretical expressions available for canonical antennas from [18]. Additional tests have been carried out to further validate the code, they are not shown for conciseness reasons.

Electric infinitesimal dipole at 6 GHz

Let us consider an electric infinitesimal dipole on the z-direction. The currents distributions are derived from the formulas $\mathbf{J}_{eq} = \mathbf{n} \times \mathbf{H}, \mathbf{M}_{eq} = \mathbf{E} \times \mathbf{n}$ and projected into the function basis created by a triangular mesh over a sphere. The results are displayed in Fig. IV.6. The directions of the currents are coherent with the theoretical expressions of the fields, validating the function basis implementation.
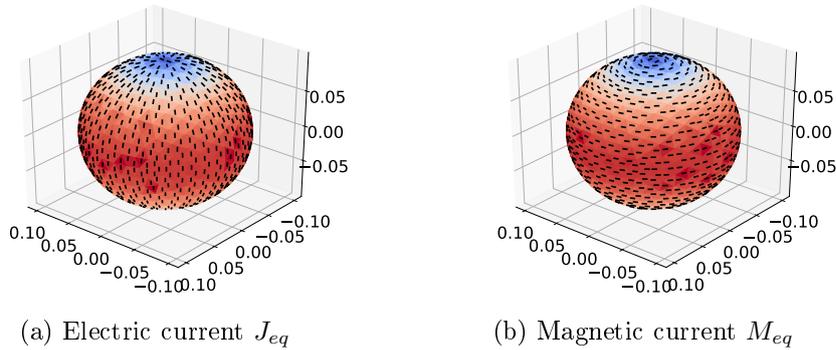

(a) Electric current J_{eq} (b) Magnetic current M_{eq}

Figure IV.6: Magnetic and electric equivalent currents (imaginary part) projected on a mesh over a sphere.

Rectangular radiating aperture (TE$_{10}$ mode) at 30 GHz

Let us now consider a rectangular aperture of size $a \times b$ in a ground plane over (xOy). The comparisons between the ideal current projected on the function basis and the currents retrieved from the theoretical far fields radiated by several apertures are shown in Fig.

IV.7. No matter the shape of the aperture (square, larger width or larger length), the currents are properly retrieved which validates the code.
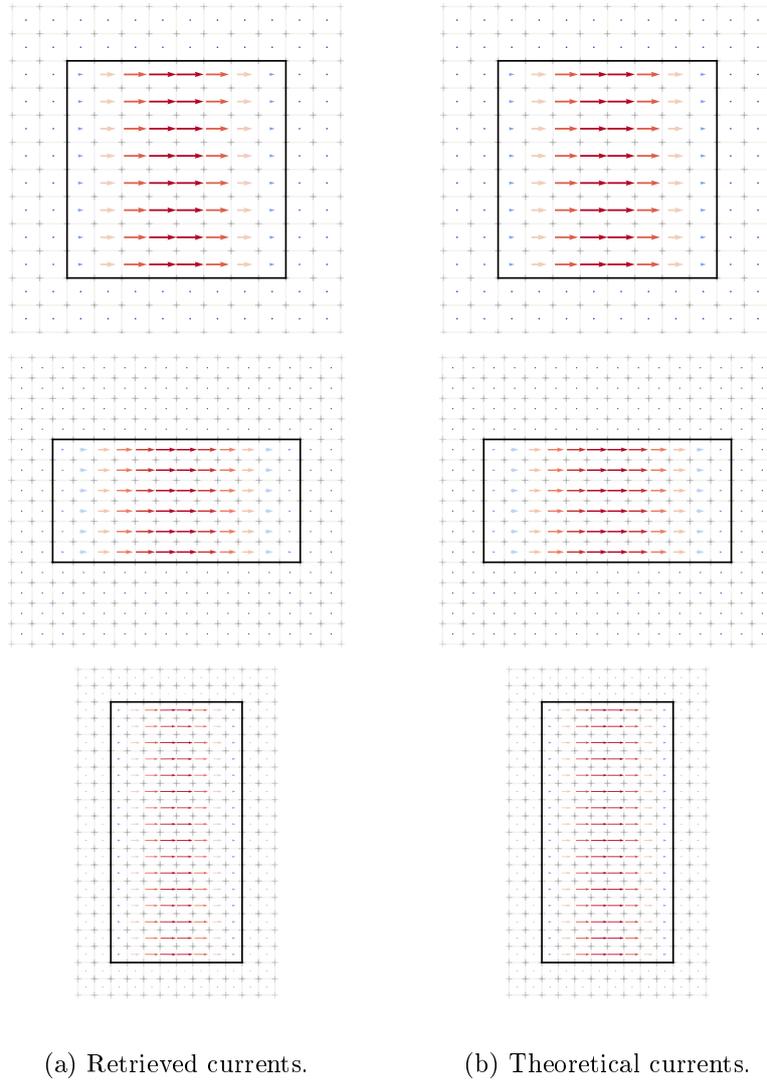

(a) Retrieved currents.   (b) Theoretical currents.

Figure IV.7: Equivalent magnetic currents M_{eq} (real part) normalized with respect to the theoretical ones on the aperture plane. The rectangular aperture is displayed and meshed by squares of side $\lambda/4$.

E-plane horn at 3 GHz

Let us consider an E-plane horn whose aperture is on the plane $z = 0$. The equivalent surface Σ surrounds the horn and the equivalent current distribution on this surface are shown in Fig. IV.8. These currents have been retrieved from far-field samples generated by the theoretical expressions. The aperture of the horn is correctly identified and the orthogonality between the electric and magnetic currents is observed and fits the expected behaviours.
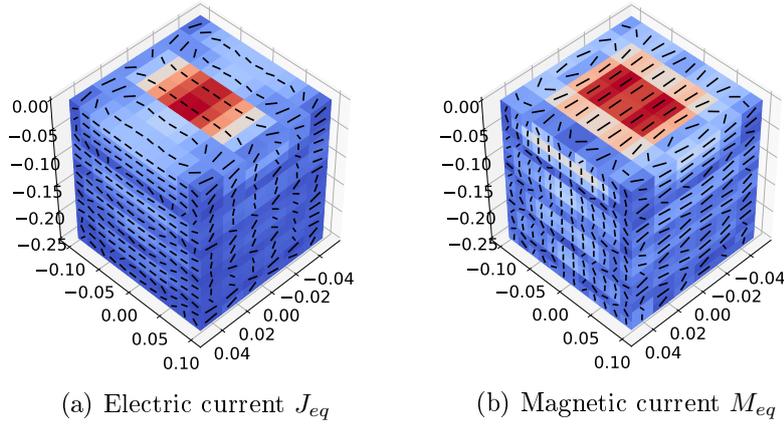
(a) Electric current J_{eq} (b) Magnetic current M_{eq}

Figure IV.8: Electric and magnetic equivalent currents (imaginary part) over a box enclosing a E-plane horn. These currents are computed from the theoretical far field samples.

IV.3 Construction of the reduced-order model

The radiation matrix from equivalent surfaces is built and its validity have been demonstrated using several canonical examples. The construction of the reduced-order model is now addressed.

IV.3.a Truncated singular value decomposition

The radiation matrix $\mathbf{A}$ is, in general, not of full rank. Many sets of currents $\mathbf{x}$ lead to the same radiated field $\mathbf{y}$. Therefore, the matrix $\mathbf{A}$ can be approximated by $\mathbf{A}_\mathrm{T}$, for which only the T largest singular values are kept:

$$\mathbf{A}_\mathrm{T} \approx \mathbf{U}\mathbf{S}_\mathrm{T}\mathbf{V}^H \qquad\qquad (IV.7)$$

where $\mathbf{V}^H$ is the conjugate transpose (also called Hermitian transpose) of $\mathbf{V}$. The columns of $\mathbf{V}$ form an orthonormal basis of the equivalent current distributions over the surface Σ while the columns of $\mathbf{U}$ are the corresponding orthonormal basis of the fields that can be radiated by the AUT. The diagonal matrix $\mathbf{S}_\mathrm{T}$ contains the first T singular values $\sigma_1 \geq \sigma_2 \geq \cdots \geq \sigma_\mathrm{T}$, the lower singular values being set to zero hence the truncation. The field $\mathbf{y}$ radiated by the AUT can thus be approximated from the first T columns of $\mathbf{U}$ as follows

$$\mathbf{y} \approx \mathbf{U}_\mathrm{T}\boldsymbol{\nu} \qquad\qquad (IV.8)$$

where $\boldsymbol{\nu}$ is the new unknown vector of length T. The quality of the approximation (IV.8) is determined by the truncation index T.

IV.3.b Physical interpretation

The SVD of the radiation matrix in (IV.7) produces 3 mathematical objects, each of them has a physical interpretation. The columns of $\mathbf{U}$ can be seen as characteristic radiated modes over the sampling positions for the given equivalent surface. The columns of $\mathbf{V}$ are the coupled characteristic current distributions on the surface. The diagonal coefficients of $\mathbf{S}$, the singular values, quantify the coupling significance between the characteristic

modes on the surface Σ and the radiated field modes. The eight first characteristic current distributions over a box (the eight first columns of $\mathbf{V}$) and their corresponding modes (the eight first columns of $\mathbf{U}$) are shown in Fig. IV.9 as an example. Several remarks can be done regarding these distributions. A smaller index corresponds to slower variations of the current distribution, also, due to the orthogonality of the columns and the numerical construction of the basis, consecutive distributions show peculiar symmetries and current flows relations. Similar observations can be done on the characteristic radiated field modes.
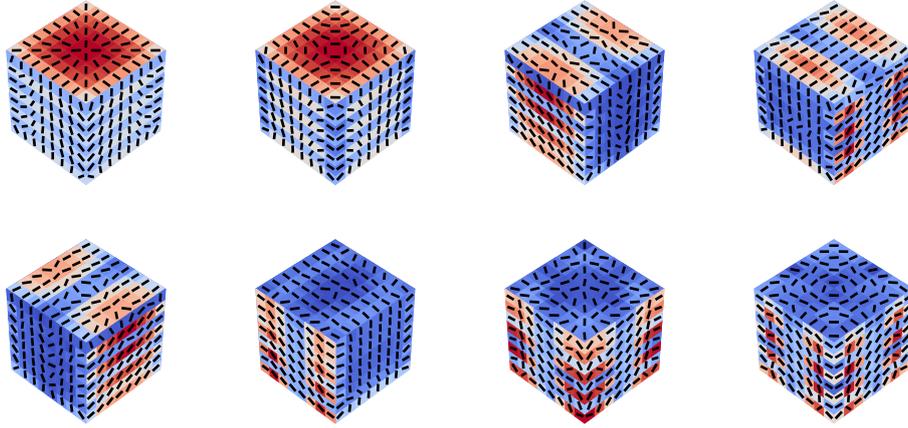
Figure IV.9: Example of the first equivalent characteristic current distributions over a box (real part).

(a) E_θ magnitude

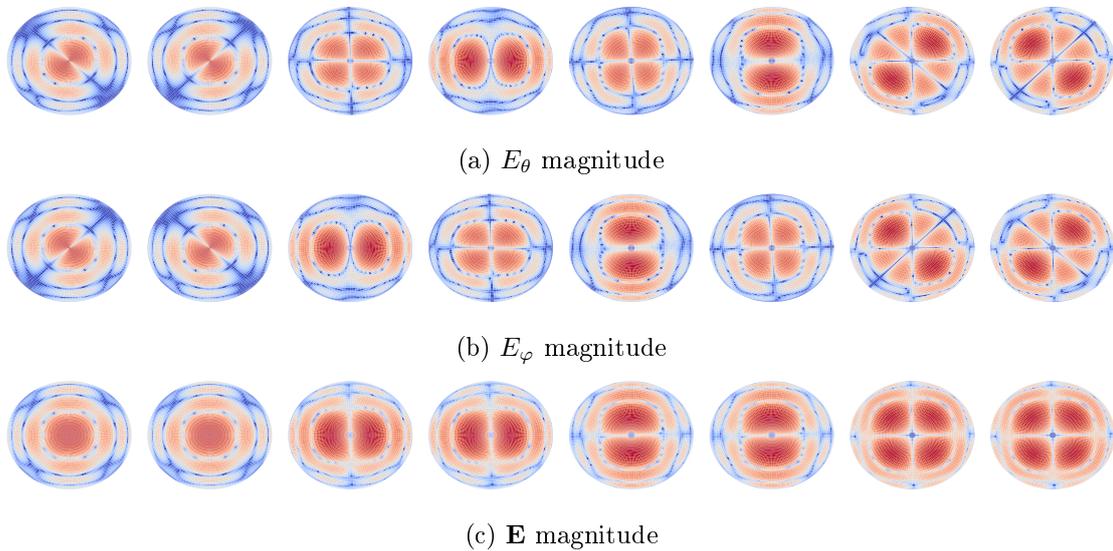(b) E_φ magnitude

(c) $\mathbf{E}$ magnitude

Figure IV.10: Normalized magnitudes of the eight first characteristic radiated field modes, in uv-maps, corresponding to the current distributions in Fig IV.9.

IV.3.c Choice of the truncation index

The choice of the truncation index T, and consequently of the size of the radiated field basis $\mathbf{U}_T$, is crucial to be able to reconstruct properly the radiated field $\mathbf{y}$ [19]. For the antenna characterization problem, this index is connected to the noise floor level of the measurement system.

Let us consider a reference field measurement $\mathbf{y}$ and its estimation $\widetilde{\mathbf{y}}$. For a measurement noise floor of R dB, we consider that $\mathbf{y}$ and $\widetilde{\mathbf{y}}$ are identical when the average difference between each sample of these two fields is smaller than R dB. This can be translated into $\|\mathbf{y} - \widetilde{\mathbf{y}}\| \leq \delta$ with $\delta = \sqrt{M}\|\mathbf{y}\|_\infty 10^{R/20}$, where M is the size of the measurement vector $\mathbf{y}$ or $\widetilde{\mathbf{y}}$.[1]

The radiation matrix $\mathbf{A}$ is well approximated by $\mathbf{A}_T$ provided that the following inequality holds true for all possible sets of equivalent currents $\mathbf{x}$

$$\|\mathbf{Ax} - \mathbf{A}_T\mathbf{x}\| \leq \delta. \tag{IV.9}$$

The left hand side of (IV.9) is bounded by $\|\mathbf{A} - \mathbf{A}_T\|\|x\| = \sigma_{T+1}\|\mathbf{x}\|$ and $\|\mathbf{B}\|$ is equal to the largest singular value of the matrix $\mathbf{B}$. Using the same properties, $\|\mathbf{y}\| = \|\mathbf{Ax}\|$ leads to $\|\mathbf{y}\| \leq \|\mathbf{x}\|\sigma_1$. By noticing that $\|\mathbf{y}\| \leq \sqrt{M}\|\mathbf{y}\|_\infty$, we can write

$$\frac{\sigma_{T+1}}{\sigma_1} \leq 10^{R/20}. \tag{IV.10}$$

Note that the criterion (IV.10) is not strictly equivalent to (IV.9). However, its validity is numerically checked in the next section.

IV.3.d Numerical validation of the truncation index

Methodology

Let us consider the reference radiated field $\mathbf{y}$ and its estimation $\widetilde{\mathbf{y}}$ computed from the truncated radiation matrix $\mathbf{A}_T$, both of size M. The Equivalence Noise Level (ENL) introduced in (I.5) provides a convenient metric to compare these two radiation patterns. The truncation index T is chosen such that $\text{ENL}(\mathbf{y}, \widetilde{\mathbf{y}}) \leq R$ for any field $\mathbf{y}$ radiated by an AUT inside the equivalent current surface Σ.

Validation

The AUT is assumed to be enclosed by a spherical equivalent surface Σ. Any fields radiated by the AUT can then be expanded into SW. As already seen in Chapter II, these SW are denoted $\mathbf{F}_{smn}$ where s is the propagating mode, $s \in \{1, 2\}$, m the order and n the degree, $|m| \leq n$, $1 \leq n$, both being integers. The truncation order of this SW expansion in n is given by [1]

$$N = \lfloor ka \rfloor + n_1 \tag{IV.11}$$

where k is the wavenumber, a the radius of the smallest sphere enclosing the sources, $\lfloor \cdot \rfloor$ is the integer part function and n_1 a positive integer. A safety margin of $n_1 = 10$ is typically chosen but this number can be lowered when expanding the electromagnetic far field.

---

[1] The notation $\| \cdot \|$ denotes the Euclidean norm, also often written $\| \cdot \|_2$ or ℓ_2 norm and $\|\mathbf{y}\|_\infty$ the maximum magnitude among the components of $\mathbf{y}$.

For numerical validation purposes, we consider a spherical equivalent surface Σ of radius $a = 2\lambda$, $\lambda = 0.1$ m and a noise floor $R = -50$ dB. The singular value distribution of the resulting radiation matrix is shown in Fig. IV.11. The truncation index T given by the criterion is also reported and corresponds to the number of SW for $n_1 = 7$, or $N = 19$. The radiation matrix $\mathbf{A}$ is well approximated by $\mathbf{A}_\mathrm{T}$ provided that any SW up to $N = 19$, $\mathbf{F}_{s,19,19}$, can be reconstructed with an ENL below R dB.
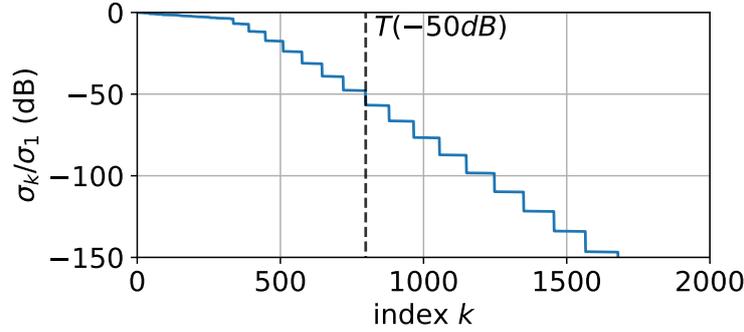

Figure IV.11: Normalized singular value distribution of the far-field radiation matrix of a sphere of radius $2\lambda = 0.2$ m. The truncation index T for $R = -50$ dB corresponds to the number of SW in the expansion for $N = 19$. The step widths correspond to the number of SW for each degree n. A similar pattern can also be found in [13].

The SW of highest degree and order, $\mathbf{F}_{s,19,19}$, is the hardest to reconstruct since it exhibits the fastest variations with respect to both directions θ and φ. The results of the reconstruction of several SW are shown in Fig. IV.12. The truncation index T for a noise floor $R = -50$ dB always leads to an ENL lower than R for all tested SW, validating numerically the proposed criterion (IV.10).
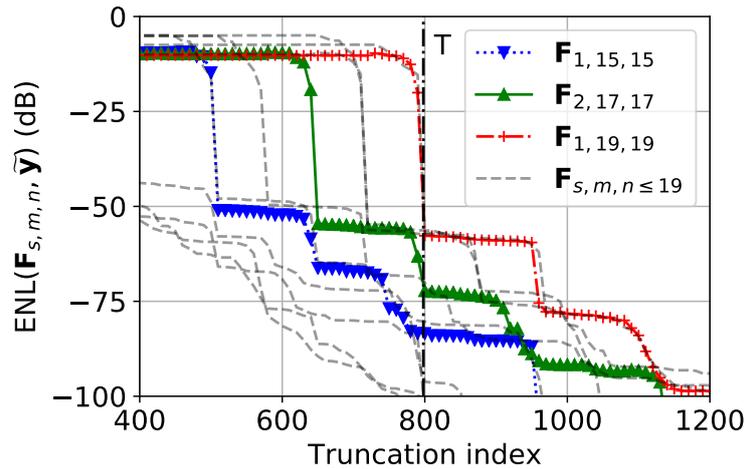

Figure IV.12: ENL between the SW, $\mathbf{F}_{smn}$, and $\widetilde{\mathbf{y}}$, its estimation from the truncated radiation matrix $\mathbf{A}_\mathrm{T}$. The truncation index T $= 798$ ensures a proper reconstruction of all SW up to $N = 19$. Unmarked dashed curves show the reconstruction performances of other SW for degrees $n \leq 19$.

IV.3.e Truncation index and equivalent surface area

The truncation index T of the singular values is determined by the low-pass behaviour of the singular value distribution. Previous analytical works on antenna characterization relying on the radiated field expansion on analytical function basis have determined that the number of coefficients to retrieve is linked to the area of some canonical surface enclosing the sources. More specifically, in the case of spherical near-field measurements as detailed in [1], the truncation order N given in (IV.11) leads to a number of spherical coefficients nearly proportional to $4\pi a^2$, the area of the minimal sphere enclosing the antenna. The work of Prof. Bucci *et al.* [5] provides an explicit relation between the number of so-called degrees-of-freedom of the radiated field for surfaces Σ with some symmetry properties,

$$N_{deg} = \frac{\mathcal{A}(\Sigma)}{(\lambda/2)^2} \qquad\qquad (IV.12)$$

where $\mathcal{A}(\Sigma)$ is the area of Σ.

We have numerically checked that two equivalent surfaces of same area, no matter their shape, indeed exhibit the same low-pass behaviour of their singular value distribution, as illustrated in Fig. IV.13. This implies and confirms that the complexity of the reduced-order model and consequently the number of unknowns in our characterization problem is given by the area of the equivalent surface Σ.
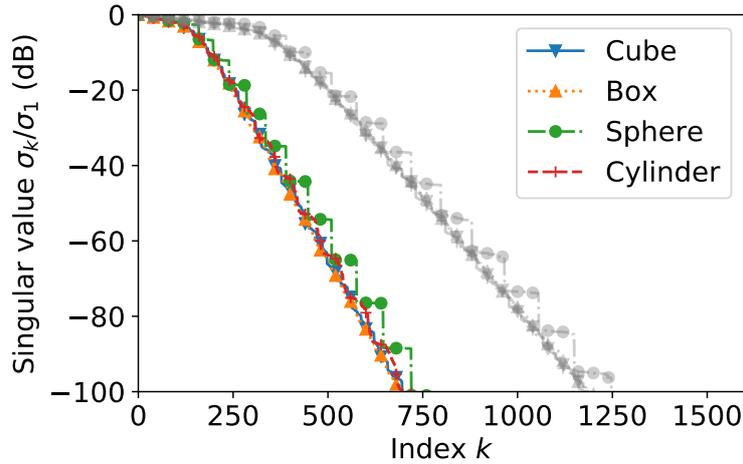
Figure IV.13: Normalized singular value distributions for two sets of equivalent surfaces having the same area. The light grey curves correspond to surfaces whose area is twice larger than the colored ones.

IV.3.f Discussions

Several parameters influence the distribution of the Singular Value (SV) distribution.

Mesh and cells

The SV distribution is influenced by the equivalent current surface mesh size. However, this distribution converges when the mesh cells are small enough. The basis functions

built from triangle or square cells of maximum length $\lambda/3$ have been empirically shown to provide stable results in all investigated antenna characterization scenarios.

Field sample distribution

The field sampling strategy over the measurement surface has a significant impact on the SV distribution. The strategies inducing an oversampling in some regions of the sphere generate a peculiar SV distribution. This behaviour with a sudden significant drop of the SV distribution translates the redundancy coming from the localized oversampling. This typically happens when considering an equiangular far-field sampling. A closed measurement surface, in the topological sense (a compact surface without boundary, like a sphere) also modifies the SVD but the proposed truncation criterion still holds.

The case of the spherical equivalent surface

The singular value distribution exhibit some steps as shown in Fig IV.11 and also reported in [13]. When a E_θ, E_φ description of the field is used, these steps increase the same way as the number of SW having the same degree n grows with respect to n. When the measurement surface is not closed (e.g. planar measurement or over an hemisphere), these steps are smoothed or non-distinguishable, further indicating that they are most likely tied to the spherical geometry. Indeed, it has been observed that using conformal cells or taking smaller cells, i.e. having a better approximation of the sphere, further increase the stair-like behaviour of the SW distribution. Note that this observation has no significant impact on the proposed method.

IV.4 Number of field samples

The steps to derive the minimum number of field samples from the reduced antenna characterization model are described, validated numerically and experimentally.

IV.4.a From the number of spherical waves to the truncation index

The main and remarkable result is that the order T of the reduced antenna characterization model depends only on the area of the surface Σ whatever its shape. Since the number of SW denoted N_{SW} is well known for a given sphere radius, we can derive the following formula:

$$\mathrm{T} = \frac{\mathcal{A}(\Sigma)}{\mathcal{A}(S)} N_{\mathrm{SW}}. \tag{IV.13}$$

where $\mathcal{A}(S)$ is the area of the surface of the minimal sphere and $N_{\mathrm{SW}} = 2(\lfloor ka \rfloor + n_1)(\lfloor ka \rfloor + n_1) + 2$ with n_1 a positive integer, as seen in Chapter II. The order of the antenna characterization model is deduced only from the area of the equivalent surface Σ and the maximum dimension of the AUT. An illustration of this statement is shown in Fig. IV.14 and a comparison between the number of degrees of freedom given by Bucci et al. in [5] in (IV.12) and the order of our model given by (IV.13) of T is provided in Fig. IV.15. We clearly observe very close behaviours between both methods.
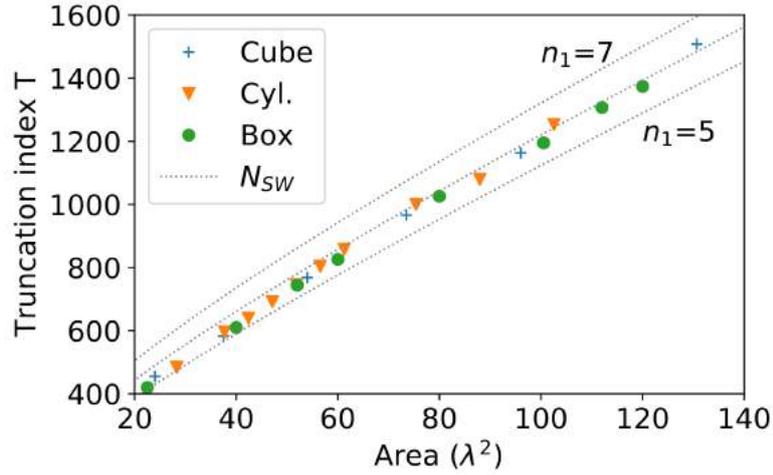
Figure IV.14: Truncation index T (i.e. the number of unknowns) as a function of the area of Σ, the surface enclosing the AUT, for various shapes and a noise floor $R = -50$ dB. Three different margins for the number of SW, N_{SW}, $n_1 = 5, 6, 7$ are shown. Note that a cube of side length 4λ has an area of 96 λ^2.

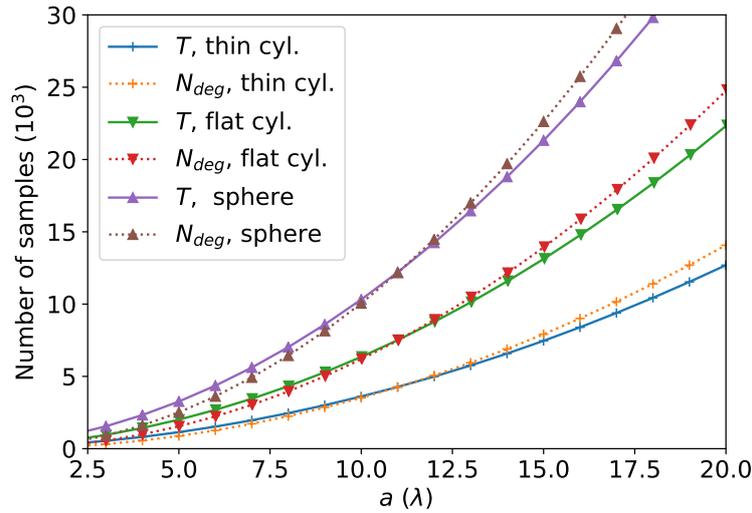

Figure IV.15: Comparison between the number of degrees of freedom in [5] and the order of the reduced model T.

IV.4.b   From the truncation index to the number of samples

The truncation index can be estimated from simple geometrical considerations, see (IV.13). It remains to derive the number of field samples from this truncation index T to complete our antenna characterization problem.

Methodology

The field $\mathbf{y}$ radiated by the AUT can be expressed as follows:

$$\mathbf{y} = \sum_{k=1,\ldots,\mathrm{T}} \boldsymbol{\nu}_k \mathbf{u}_k + \mathbf{n} \tag{IV.14}$$

where the vector $\mathbf{n}$ stands for the part that is unexplained by the reduced order model, i.e. the measurement noise and the truncation error. The norm of $\mathbf{n}$ is lower than R dB when T has been properly set.

Our goal is to determine the unknown vector $\boldsymbol{\nu}$ of length T from a minimum number of field samples. Similarly to our approach with the SW in Section IV.3.d, we aim at reconstructing each of the characteristic modes $\mathbf{u}_k, k = 1, \ldots, \mathrm{T}$ from only M_S sampling points by solving

$$\boldsymbol{\nu}^{(s)} = \arg\min_{\boldsymbol{\nu}} \|\mathbf{y}_k^{(s)} - \mathbf{U}_{\mathrm{T}}^{(s)} \boldsymbol{\nu}\| \tag{IV.15}$$

where $\mathbf{y}_k = \mathbf{u}_k \boldsymbol{\nu} + \mathbf{n}$ for each tested k and the superscript (s) denotes the subsample.

To assess the quality of the reconstruction and thereby the choice of the number of samples M_S, we compute the mean of $\mathrm{ENL}(\mathbf{u}_k, \widetilde{\mathbf{u}}_k)$ for all k where $\widetilde{\mathbf{u}}_k$ is the estimated characteristic mode computed solving (IV.15) from M_s field samples. Similarly to Section IV.3.d, the reconstruction is considered successful when the mean ENL is lower than the noise floor R dB.

Results

A sampling is defined by its size and its distribution. We use the measurement ratio M_S/T, where M_S is the number of field samples. The proposed reduced order model is applied using four sampling strategies and a spherical equivalent current surface Σ of radius 2λ. The samplings are: Fibonacci [20], one of the most uniform distributions on the sphere, the *igloo* sampling [21], close to being uniform while providing an easy scan for positioning systems available at IETR, random sampling, where the points are chosen randomly over the sphere (mean over 20 trials) and equiangular, also called constant angular step sampling, commonly used in spherical near-field measurements [1].

As shown in Fig. IV.16(a), the uniformity of the sampling distribution is crucial to minimize the number of samples as the Fibonacci and *igloo* sampling are clearly the first ones to reach the noise floor, at a measurement ratio around 1.17. This oversampling factor corresponds to the intersection point of the curves with the horizontal line located at the noise floor R. From now on, we only consider the *igloo* sampling in the following as it is the one applied in our anechoic chamber while keeping in mind that Fibonacci behaves similarly.

In addition, this reliable oversampling factor is stable with respect to the measurement noise floor R, as shown by the grey curves in Fig. IV.16(a). Note that both M_s and T logically increase when the noise floor level R is reduced.

The influence of the surface shape Σ on the measurement ratio has also been investigated. The results, shown in Fig. IV.16(b), demonstrate that a measurement ratio of 1.25 is sufficient for all shapes and by extension most antenna geometries.
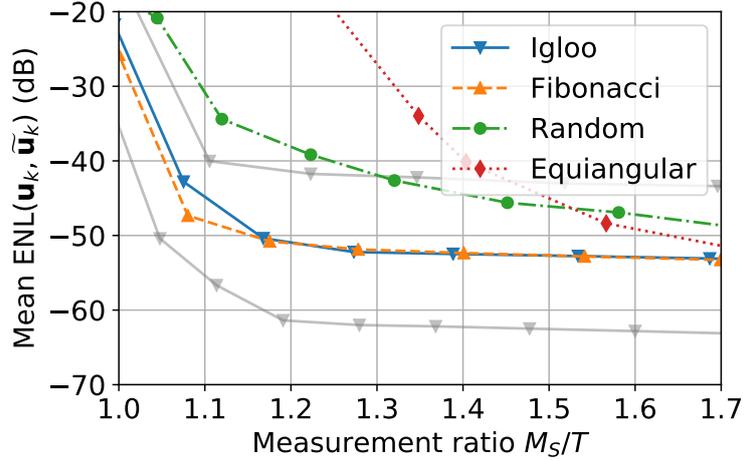
(a)
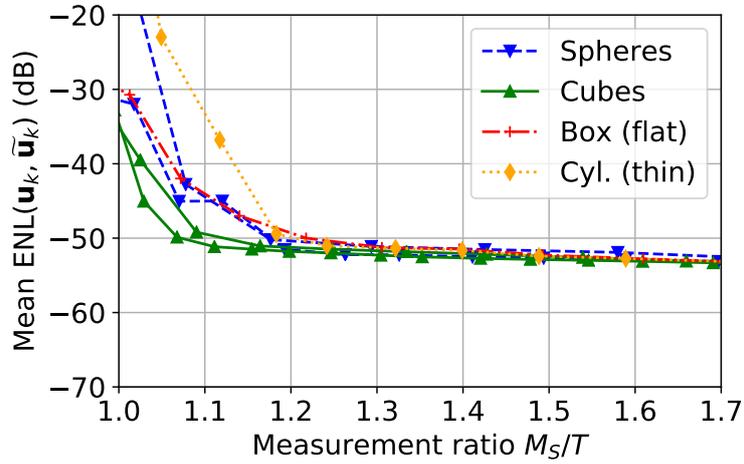
(b)

Figure IV.16: Mean ENL reconstructions of the radiated modes for a noise floor $R = -50$ dB. (a) Comparison between sampling strategies: the grey curves are obtained for $R = -40$ and -60 dB with an *igloo* sampling. (b) Comparison of various shapes using an *igloo* sampling.

Number of field samples

From the previous studies and results, it follows that the number of samples can be safely set to

$$M_S = \chi \text{T} \tag{IV.16}$$

where T can be estimated from (IV.13) and χ is an oversampling factor, as introduced by Bucci *et al.* [5]. According to our results, an oversampling factor of around $\chi = 1.25$ works satisfactorily in all investigated antenna characterization problems (antenna shape and measurement noise floor).

IV.4.c   Experimental validation

The methodology to derive the minimum number of field samples is assessed experimentally with the characterization of two radiating structures of radically different shapes and operating frequencies.

Standard gain horn at X band

The antenna is measured at 10 GHz in the MVG multi-probe system StarLab [22] of IETR-INSA, the measurement configuration is shown in Fig. IV.17. The reference and the measurement field samplings are generated in far field at any position using the spherical coefficients returned by the MVG software.
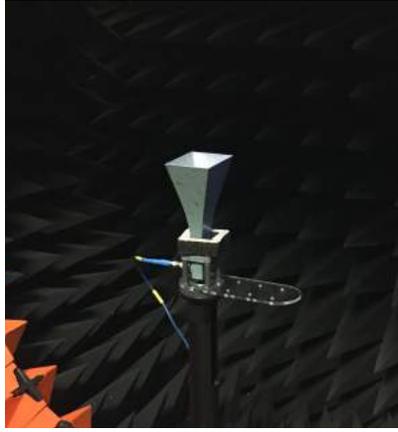

Figure IV.17: Picture of the X band horn in the MVG StarLab system.

Three equivalent current surfaces Σ enclosing the horn are considered: a box, a cylinder and a sphere, placed as shown in Fig. IV.18(a). The corresponding singular values of the radiation matrices are shown in Fig. IV.18(b). The sphere enclosing the AUT has a radius a of 10 cm $\approx 3.3\lambda$. The measurement noise floor is estimated to be equal to $R = -45$ dB. As shown by the singular value distributions, the orders of the model T for the box, the cylinder and the sphere are $1141, 1389$ and 1966 respectively.

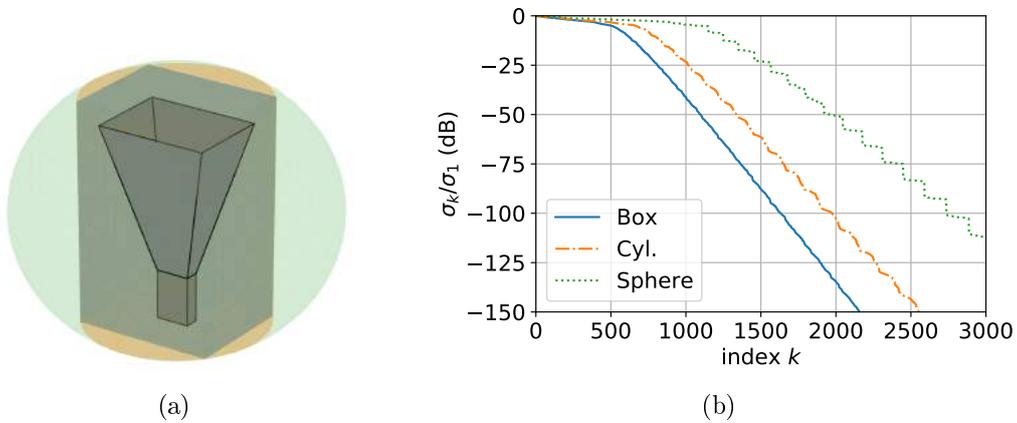(a)   (b)

Figure IV.18: (a) Representation of the three equivalent current surfaces Σ (sphere, cylinder and box) used for the horn characterization. (b) Normalized singular value distribution of the corresponding radiation matrices.

The validity of the proposed minimum number of field samples (IV.16) is shown in Fig. IV.19. The ENL metric between the reference field $\mathbf{y}$ and the one estimated from M_S samples is plotted for the three equivalent current surfaces as a function of M_S. First, the vertical lines, computed from (IV.16), indicate when the aimed reconstruction accuracy should be achieved, ENL $\leq R = -45$ dB. Second, the surface that best fits the AUT (the box in this case) is clearly the one leading to the minimum number of samples.
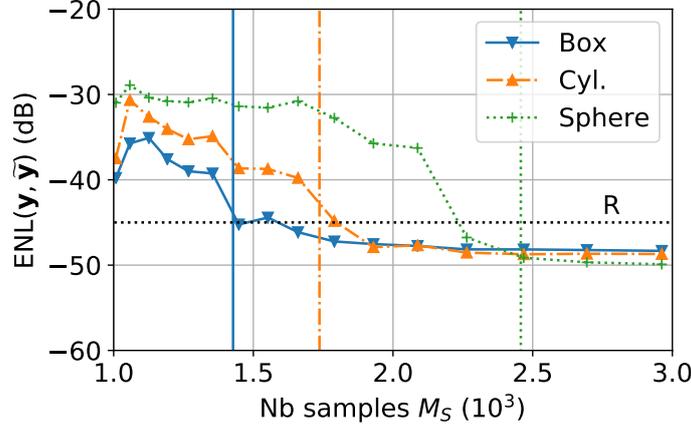

Figure IV.19: ENL reconstruction metric between the reference field $\mathbf{y}$ and its estimation $\widetilde{\mathbf{y}}$ using the reduced order model for a noise floor of $R = -45$ dB for various sample sizes M_S. The vertical lines are the number of samples corresponding to an oversampling of $\chi = 1.25$ for the respective shapes.

The reconstructions of the far field over a cutting plane are shown in Fig. IV.20 in order to further demonstrate the importance of the choice of the surface surrounding the AUT. The minimum number of field samples advocated for the box has been chosen, $M_S = 1448 \approx 1.25 \times 1141$. An excellent agreement between the reference and the reconstruction using the box is achieved whereas the two other surface shapes lead to inaccurate far fields.
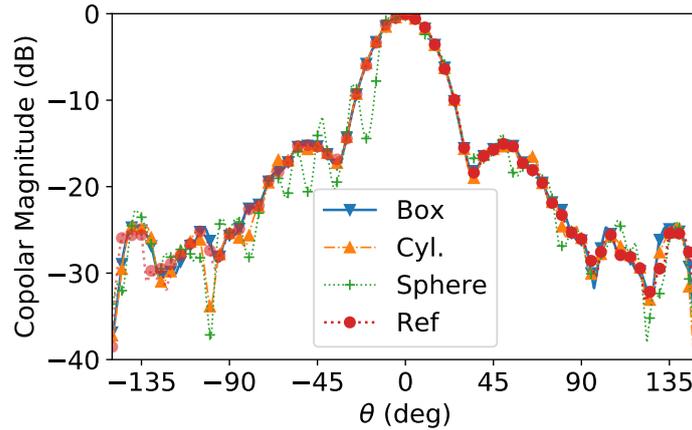

Figure IV.20: Normalized copolar component magnitudes of the X band horn at 10 GHz. The reference comes from the MVG software and others are reconstructions from only $M_s = 1448$ field samples, as advocated for the box surface (blue vertical line of Fig. IV.19).

Pillbox antenna at 230 GHz

Let us consider the pillbox antenna designed by KTH and IETR [23] measured in far field at 230 GHz in the M^{2}ARS facilities at IETR. An image of the prototype is shown in Fig. IV.21. The reference far-field pattern is provided by a high density measured field sampling.
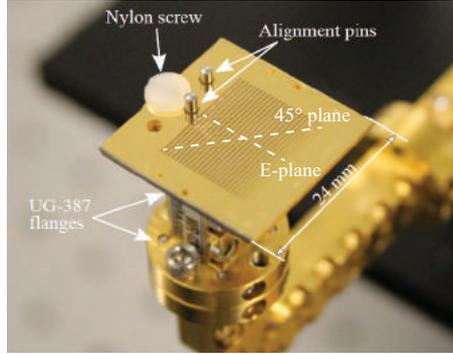
Figure IV.21: Picture of the pillbox antenna designed by KTH and IETR [23]. The frequency bandwidth of operation spans from 220 to 300 GHz.

The considered equivalent surface is a box of dimensions $25 \times 25 \times 4$ mm, i.e. approximately $20\lambda \times 20\lambda \times 3\lambda$. A noise floor of $R = -45$ dB is assumed, leading to T around 4×10^3 coefficients. We show in Fig. IV.22 the ENL metric between the reference field and the reconstruction using the reduced order model as a function of the measurement sampling ratios $M_S/$T, or equivalently of the oversampling factor χ. An oversampling factor $\chi = 1.25$ is close to the optimal number of samples to reach the aimed accuracy, which confirms experimentally our previous studies.

Figure IV.22: ENL reconstruction metric between the reference field and its estimation using the reduced order model as a function of the measurement ratio (or oversampling factor).

To provide a more intuitive illustration of the results, the reconstruction of the field in the main cutting plane is displayed in Fig. IV.23 for several oversampling factors χ.

No significant changes on the reconstruction accuracy between the oversampling $\chi = 1.25$ and 1.4 with respect to the reference are observed 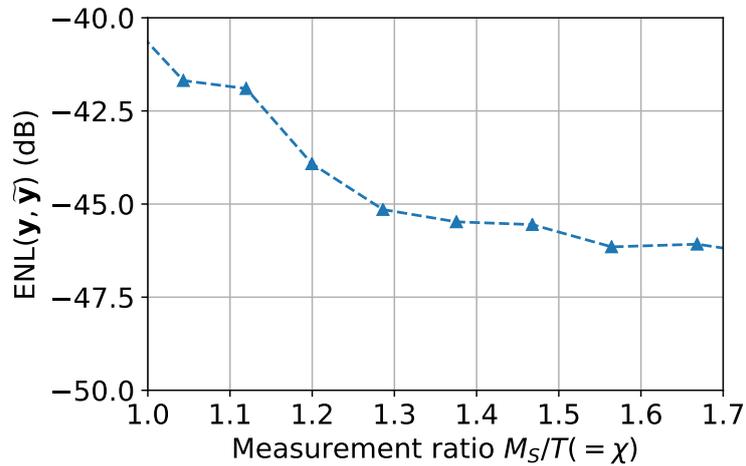while the case $\chi = 1.1$ displays more numerical errors, even close to the main beam. The far-field cartography is available in Fig. II.21.
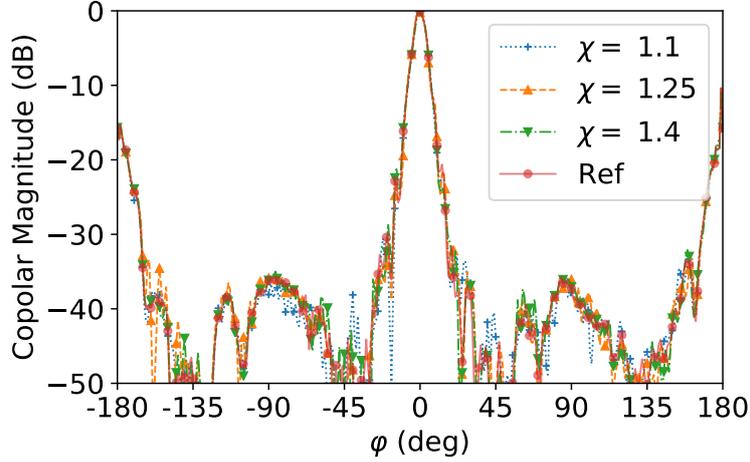
(a) Copolarization
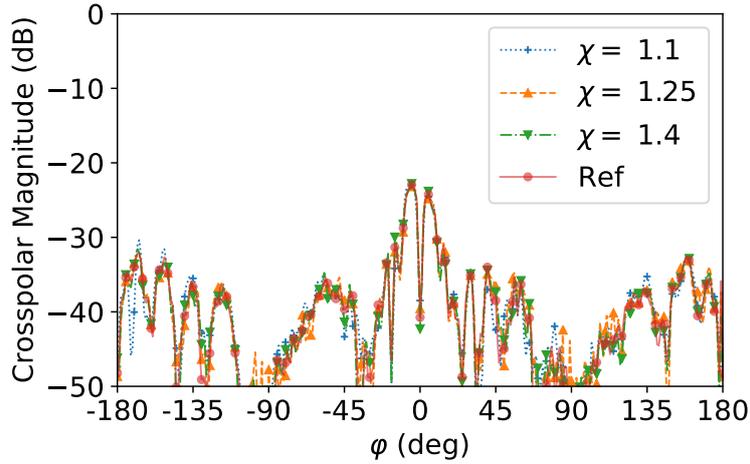
(b) Crosspolarization

Figure IV.23: Normalized reconstruction of the field components in the main cutting plane in φ for several oversampling factors.

IV.4.d   Fast antenna measurements at IETR

The IETR spherical measurement systems have been described and illustrated in Section I.2.c. The estimation of the duration of the field acquisition is detailed in Appendix A.

This duration estimation using SW has been discussed in Chapter II. The present chapter has provided the number of field samples and the field sampling strategy using the Reduced Order Model (ROM) from equivalent currents approach. Consequently, we can perform the same estimation and the results are displayed in Fig. IV.24. It compares the

duration of the field acquisition of an antenna that can be fitted into a cube. Thanks to the tailored constructed reduced basis, this duration can be further reduced with respect to the sparse Spherical Wave Expansion (SWE).

Figure IV.24: Estimated field acquisition durations at IETR using the standard approach and the proposed fast antenna characterization procedures.
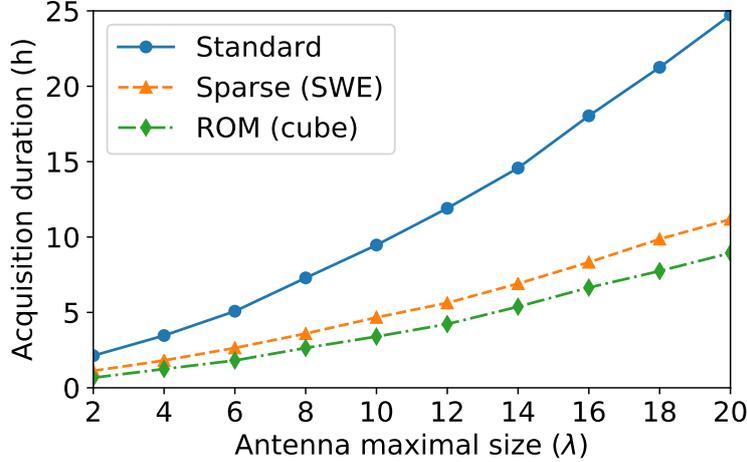

IV.4.e   Summary

The characterization of far-field patterns from a minimum number of samples has been experimentally validated using two very different antenna types, shapes and operating frequencies. Indeed, two significantly different antennas in these aspects have been characterized in two measurement systems; an all-in-one commercial system [22] and an academic laboratory anechoic chamber [24].

Less field samples are required when the convex surface enclosing the AUT is tailored to its shape, which confirms the link between number of samples and area of this surface. Moreover, an oversampling value of $\chi = 1.25$ is shown to be a reasonable choice to find the minimum number of samples as confirmed by these experimental results.

IV.5   Conclusion

The steps to determine the minimum number of field samples to characterize antenna far-field radiation patterns have been detailed. The proposed methodology calls for the construction of the radiation matrix involved in the antenna characterization problem. By appropriately truncating its singular value decomposition, a reduced dictionary of the possible far-fields radiated by the antenna under test is built for a chosen accuracy level. Instead of using all-purpose analytical basis functions exhibiting intrinsic symmetries, the proposed strategy enables to generate numerically a compressed basis tailored to the antenna characterization problem. The practical relevance of the so-customized basis has been thoroughly investigated. The influence of the field sampling strategy, its robustness with respect to noise and equivalent current surface shape surrounding the antenna under test leads to a minimum number of field samples that takes into account practical meas-

urement considerations. This number depends on the area of the surface enclosing the antenna under test. This work confirms, and somehow extends by means of numerical tools, the fundamental and pioneering analytical derivations on the minimum non-redundant sampling by Bucci *et al.* [5]. The proposed method has been applied to characterize the far field of two antennas at 10 and 230 GHz, respectively. These measurements, carried out in two different facilities, validate experimentally the proposed approach and show its potentialities.

Bibliography

[1] J. Hald, J.E. Hansen, F. Jensen, and F.H. Larsen. *Spherical Near Field Antenna Measurements*. Peter Peregrinus, 1988.

[2] O. M. Bucci and G. Franceschetti. On the spatial bandwidth of scattered fields. *IEEE Trans. on Antennas and Propag.*, 35(12):1445–1455, 1989.

[3] O. M. Bucci and G. Franceschetti. On the degrees of freedom of scattered fields. *IEEE Trans. on Antennas and Propag.*, 37(7):918–926, 1989.

[4] O. M. Bucci, C. Gennarelli, and C. Savarese. Optimal interpolation of radiated fields over a sphere. *IEEE Trans. on Antennas and Propag.*, 39(11):1633–1643, 1991.

[5] O. M. Bucci, C. Gennarelli, and C. Savarese. Representation of electromagnetic fields over arbitrary surfaces by a finite and nonredundant number of samples. *IEEE Trans. on Antennas and Propag.*, 46(3):351–359, March 1998.

[6] G. Giordanengo, M. Righero, F. Vipiana, M. Sabbadini, and G. Vecchi. Fast antenna testing with reduced near field sampling. *IEEE Trans. on Antennas and Propag.*, 62(5):2501–2513, May 2014.

[7] M. Salucci, M. D. Migliore, G. Oliveri, and A. Massa. Antenna measurements-by-design for antenna qualification. *IEEE Trans. on Antennas and Propag.*, 66(11):6300–6312, Nov 2018.

[8] B. Stupfel and Y. Morel. Singular value decomposition of the radiation operator—application to model-order and far-field reduction. *IEEE Trans. on Antennas and Propag.*, 56(6):1605–1615, June 2008.

[9] B. Fuchs and A.G. Polimeridis. Reduced-order models for fast antenna characterization. *IEEE Trans. on Antennas and Propag.*, 67(8):5673–5677, Aug. 2019.

[10] Y. Alvarez, F. Las-Heras, B. A. Dominguez-Casas, and C. Garcia. Antenna diagnostics using arbitrary-geometry field acquisition domains. *IEEE Antennas and Wireless Propagation Letters*, 8:375–378, 2009.

[11] J. L. Araque Quijano and G. Vecchi. Improved-accuracy source reconstruction on arbitrary 3-d surfaces. *IEEE Antennas and Wireless Propagation Letters*, 8:1046–1049, 2009.

[12] L. J. Foged, F. Mioc, M. Sabbadini, J. L. A. Quijano, and G. Vecchi. Advanced antenna diagnostics based on equivalent currents. In *Proceedings of the Fourth European Conference on Antennas and Propagation*, pages 1–4, 2010.

[13] J. L. Araque Quijano and G. Vecchi. Field and source equivalence in source reconstruction on 3d surfaces. *Progress In Electromagnetics Research*, 103:67 – 100, 2010.

[14] Roger F. Harrington. *Time-Harmonic Electromagnetic Fields*. IEEE-Press, 2001.

[15] J. L. Araque Quijano, L. Scialacqua, J. Zackrisson, L. J. Foged, M. Sabbadini, and G. Vecchi. Suppression of undesired radiated fields based on equivalent currents reconstruction from measured data. *IEEE Antennas and Wireless Propagation Letters*, 10:314–317, 2011.

[16] S. Rao, D. Wilton, and A. Glisson. Electromagnetic scattering by surfaces of arbitrary shape. *IEEE Trans. on Antennas and Propag.*, 30(3):409–418, 1982.

[17] M. Abramowitz and I. A. Stegun. *Handbook of Mathematical Functions with Formulas, Graphs, and Mathematical Tables.* Dover, New York, 1964.

[18] C. A. Balanis. *Antenna Theory: Analysis and Design.* Wiley-Interscience, 2005.

[19] P. C. Hansen. The L-curve and its use in the numerical treatment of inverse problems. In *Computational Inverse Problems in Electrocardiology.* WIT Press, 2000.

[20] B. Hofmann, O. Neitz, and T. Eibert. On the minimum number of samples for sparse recovery in spherical antenna near-field measurements. *IEEE Trans. on Antennas and Propag.*, 67(12):7597–7610, 2019.

[21] B. Fuchs, L. Le Coq, S. Rondineau, and M.D. Migliore. Fast antenna far field characterization via sparse spherical harmonic expansion. *IEEE Trans. on Antennas and Propag.*, 65(10):5503–5510, Oct. 2017.

[22] Starlab 650MHz-18GHz. MVG, 2020. Available at https://www.mvg-world.com/fr/products/antenna-measurement/multi-probe-systems/starlab.

[23] A. Gomez-Torrent, M. Garcia-Vigueras, L. Le Coq, A. Mahmoud, M. Ettorre, R. Sauleau, and J. Oberhammer. A low-profile and high-gain frequency beam steering subterahertz antenna enabled by silicon micromachining. *IEEE Trans. on Antennas and Propag.*, 68(2):672–682, Aug. 2020.

[24] Plateforme M2ARS. IETR-UR1, 2020. Available at https://www.ietr.fr/plateforme-m2ars-manufacturing-measurement-analysis-radiating-systems.

General conclusion

Summary and outcomes

The main goal of this work has been to develop methods for improving the characterization of antennas and thereby make a more efficient use of measurement facilities. These methods encompass a measurement procedure combined to a dedicated processing in order to accelerate and/or increase the accuracy of the measurement of antenna radiation patterns.

The characterization of antenna radiation patterns can be speeded up by reducing the number of field samples to be measured. For that purpose, two different strategies have been proposed.

The first one relies on the sparse spherical wave expansion of the field radiated by antennas. It only requires the maximum electrical dimension of the antenna under test. An automatic procedure, that combines a coarse field sampling and a sparse recovery algorithm, has been developed and described. By leveraging the sparsity of the spherical wave expansion of the field, this approach enables to significantly reduce by a factor of about 3 the number of field samples as compared to standard (Nyquist based) approaches. Although providing an approximation of the antenna reconstructed radiation patterns, this strategy turns out to be very efficient, as demonstrated both numerically and experimentally in a number of representative radiating structures of various types and operating in diverse frequency bands. Moreover, estimations of the field acquisition duration are provided in order to assess the gain in measurement time. It is shown that the duration of the field acquisition time can be approximately halved in our anechoic chambers between the fast measurement technique and the Nyquist sampling rate approach.

The second approach, to speed up antenna pattern measurements, is based on the construction of a reduced order model corresponding to the antenna characterization problem. This strategy calls for stronger prior knowledge about the antenna under test than the first one, since both the antenna outer dimensions and the measurement surface are required to build the radiation matrix. This matrix links the inputs to the outputs of the system, namely the equivalent currents representing the antenna to the radiated field. By appropriately truncating the singular value decomposition of this matrix, a reduced-order model of the antenna characterization problem is constructed. In other words, the proposed approach generates a compressed numerical basis tailored to the antenna to be characterized. The influence of the field sampling strategy and its robustness with respect to noise has been investigated to demonstrate the efficiency of the approach and provide a realistic minimum number of field samples. This latter confirms and somehow extends the existing analytical derivations on the non-redundant sampling: the number of samples is roughly given by $\mathcal{A}(\Sigma)/\lambda^2$ where $A(\Sigma)$ is the area of the equivalent current surface enclosing the sources. Various numerical and experimental antenna characterizations carried out in di-

verse frequency bands confirm the potentialities and practical relevance of this technique.

In addition and complementarily to these two fast antenna characterization approaches, post-processing procedures have been developed to improve the quality of the antenna pattern reconstruction without resorting to any additional measurement. More specifically, techniques to optimize the positioning of the antenna under test from the spherical wave spectrum of its radiated field, have been developed and described. In a nutshell, the appropriate choice of the antenna position and orientation produces a more compact spherical wave spectrum which eases the radiated field interpolation. These approaches harness the analytical formulas for translation and rotation of the spherical waves. This antenna positioning technique has been validated numerically and experimentally in various representative and frequently encountered scenarios including the case where antennas are mounted on a structure that inevitably contributes to the radiation.

The achievement of this PhD work has required the development, the implementation and validation of several codes as well as the use and adaptation of existing mathematical routines. Thus, electromagnetic modelling methods have been developed such as the spherical wave expansion of the radiated field and a surface integral equation method of moment. Mathematical tools related to spherical waves have been implemented such as the translation and rotation of the spherical waves. Finite element based tools have been used, adapted and implemented such as the surface meshing and the current visualization. Finally, optimization solvers have been exploited and tuned to our needs such as sparse recovery methods, Gaussian processes and gradient descent algorithms. In addition to these mathematical and theoretical developments, experimental validations have been carried out in the measurement facilities of the IETR laboratory in order to validate each step of the proposed antenna characterization procedures.

Perspectives

Following this PhD work, several extensions seem natural and are currently under investigation. Others are considered as promising and could be endeavoured in a near future.

Fast near-field antenna measurements

The work on fast antenna characterization via the construction of a reduced order model has been validated in this PhD thesis on far-field measurements. The near-field validations have been driven on theoretical or simulation dataset. However, in the whole methodology and specifically in the construction of the radiation matrix, there is nothing that restricts the use of the proposed reduced order model approach to the far field. Therefore, this work can be extended to speed up the near-field characterization of antennas. The main foreseen difficulty lies in our opinion in the sampling strategy that depends on the near-field surface scan.

Phaseless antenna characterization with a reduced number of samples

Phaseless antenna characterization has recently attracted a lot of attention for many reasons, including the lower cost of the required hardware and the general increase of operating frequency which makes the accurate phase measurement difficult. Phaseless characterization techniques generally require the measurement of the field intensity on at least two surfaces in order to be able to retrieve the phase while mitigating ambiguity issues. This

(double) measurement would therefore greatly benefit from a reduction of the number of field samples. We believe that combining the fast antenna measurement strategies proposed in this thesis to phaseless antenna measurement approaches previously developed in our laboratory makes sense.

Frequency interpolation

Antenna patterns are usually not characterized at a single frequency but over a given bandwidth. In order to make such antenna characterization as efficient as possible, the electrical axis (i.e. the frequency axis) should be, in addition to the 3D spatial domain, smartly sampled. Since the duration of both continuous and step-by-step field acquisition is impacted by the number of sampled frequencies, reducing the frequency axis sampling appears as a logical step to further speed up the antenna characterization.

Phase center estimation

The optimization of the antenna position with respect to the measurement system, has been driven by the concentration of its SW spectrum towards low degree spherical modes. This procedure leads to smooth out the phase variation of the field in the main beam of the radiated pattern. This let us think that our antenna positioning procedure could be adapted in order to determine the antenna phase center.

Appendices

A   Spherical field acquisition duration estimation at IETR

This appendix explains how the duration of the field acquisition is estimated for the measurements in the anechoic chambers of IETR, especially for CACENDRA, dedicated to the measurement of antennas working in the centimetric wavelength range.

Geometrical description

The measurement system is a roll-over-azimuth one. It allows a scan of the full sphere. The coordinate system associated to the Antenna Under Test (AUT) and rotation axis are illustrated in Fig. V.2. The fields are measured using the Vertical/Horizontal vector description of the field, defined in Fig V.1.
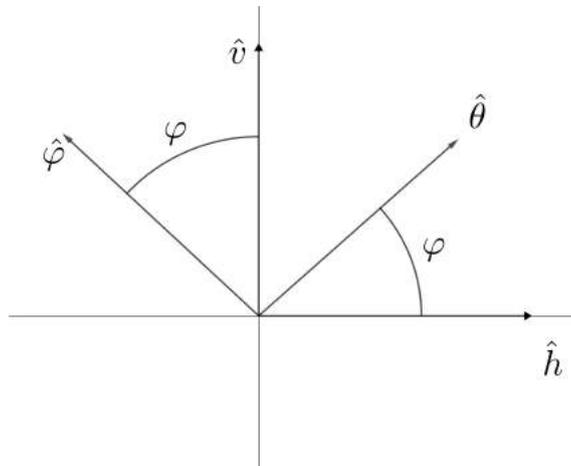
Figure V.1: The transformation between the spherical basis and the third definition of co- and cross-polarization by Ludwig.

Summary of the procedure

The igloo sampling strategy is used at IETR for reasons described in Section I.3.c. AS a reminder, it is defined as $\delta\varphi = \delta\theta/\sin\theta$, so it has a constant azimuth step $\delta\varphi$ per sampled Θ position, which is also sampled with a constant step. Each θ, or latitude cut, is scanned twice, once for each polarization. The scan is done step-by-step, the positioning system stops completely at each sampling position to perform the measurement of the field at the desired frequencies. The result estimation duration are given by: the time required to run through the whole sampling according to the IETR measurement procedure, the change of
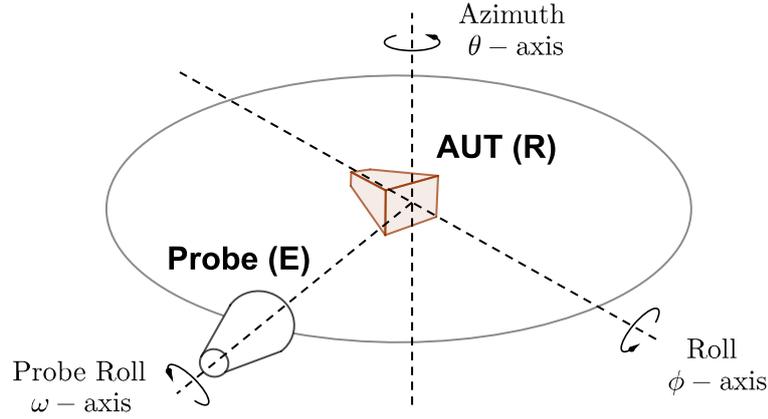
Figure V.2: Roll-over-azimuth positioning system for spherical measurements of IETR-UR1.

polarization and the time spent at each point for the signal acquisition (frequency sweep and data transfer). Finally, the engines always operate sequentially: two engines never act at the same time.

Modelling of the positioning system engines

Each engine movement is described by 2 or 3 phases, considering only non-elastic movements, as shown in Fig. V.3. The engine speed increases linearly according to a certain slope a. If the cruising speed v_{max} is reached, i.e. the angular step is large enough, the speed stays at this maximum value. Finally the rotation speed decreases with the opposite acceleration to the first phase, $-a$. This model is used for both rotation axis of the AUT: azimuth θ and roll φ. Four parameters are thus required to compute the duration of any angular movement for these two axis. For the change of polarization, the duration is constant as the rotation angle is always equal to 90°. Consequently, the parameters of this rotation axis are not required.

Figure V.3: Modelling of the speed variation through time

Let t_α the required time for the rotation engine in the direction α to perform a given angular step $d\alpha$. This elapsed time satisfies:

$$d\alpha = \int_0^{t_\alpha} v(t)dt.$$

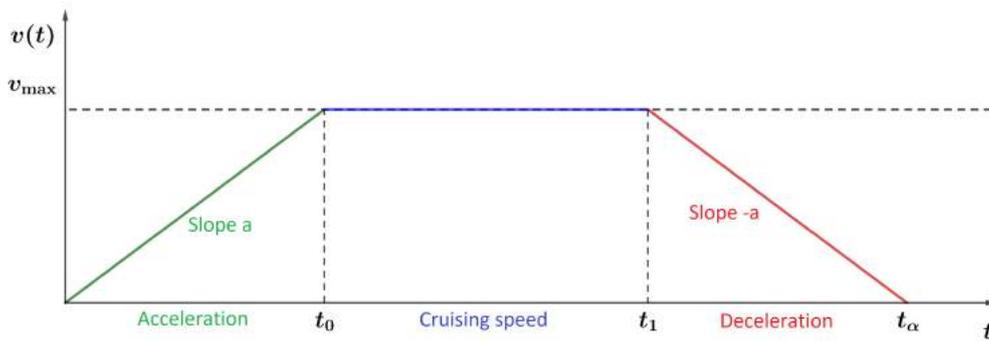In all cases, the function $v(t)$ has an axial symmetry according to $t = \frac{t_\alpha}{2}$, thus:

$$d\alpha = 2 \int_0^{\frac{t_\alpha}{2}} v(t)dt.$$

The speed satisfies $v(t) = \min\{v_{\max}, at\}$ for $t \in \left[0, \frac{t_\alpha}{2}\right]$ where a and $v_{\max}$ are illustrated in Fig. V.3. As already mentioned, there are two cases to consider.

- The cruising speed $v_{\max}$ is not reached: then $v(t) = at$ for $t \in \left[0, \frac{t_\alpha}{2}\right]$. So $d\alpha = a\left(\frac{t_\alpha}{2}\right)^2$ and $t_\alpha = 2\sqrt{\frac{d\alpha}{a}}$. If $\frac{1}{2}at_\alpha > v_{\max}$, the other case is considered.

- The cruising speed $v_{\max}$ is reached: $v(t) = at$ for $t \in [0, t_0]$ where $t_0 = \frac{v_{\max}}{a}$ and $v(t) = v_{\max}$ for $t \in \left[t_0, \frac{t_\alpha}{2}\right]$. Thus $d\alpha = v_{\max}t_\alpha - \frac{v_{\max}^2}{a}$ and finally: $t_\alpha = \left(\frac{d\alpha}{v_{\max}} + \frac{v_{\max}}{a}\right)$.

Let us assume that the AUT is at the position θ_i and at the first desired point in φ. Let M_i the number of sampling points located in this θ-cut and T_i the required time to go through the M_i φ-points. We have:

$$T_i = (M_i - 1)t_{\varphi,i} + M_i t_{\mathrm{stop}}.$$

where $t_{\varphi,i}$ is the time required between two consecutive φ-points of the sampling for the i-th θ cut, t_{stop} the stopping time. The total time T of the whole field acquisition is

$$T = \sum_{i=1}^K (2T_i + 2t_{\mathrm{pol}} + t_\theta) - 2t_{\mathrm{pol}} - t_\theta,$$

where $K = \frac{b_\theta}{\delta\theta} + 1$ is the number of latitude cuts, b_θ is the upper bound of the required θ interval ($b_\theta = \pi/2$ for an hemisphere), t_{pol} is the time for polarization change (90° along the ω rotation axis according to Fig. V.2) and t_θ is the time required for going from θ_i to θ_{i+1}. Note that each θ cut has to be run through twice, hence the factor 2, but we only change θ once per cycle, except for the last one. Similarly, we do not count polarization change at the beginning and at the end, hence the $-2t_{\mathrm{pol}}$. More specifically, for an equiangular sampling, T_i is the same for every i and $T_i = \frac{2\pi}{\delta\varphi}(t_\varphi + t_{\mathrm{stop}}) - t_\varphi$.

Estimation of the parameters

A time-stamped measurement of a Luneburg antenna designed for 12 GHz has been used to deduce the velocity and acceleration of the engines and check the reliability of the estimated duration. All durations reported in this table are for one polarization measurement.

Angle	Angular step (deg)	Number of points	Duration (s)
φ	60	6	62
φ	5	72	335
φ	3	120	498
θ	177	$\emptyset$	44
θ	1	181	763

Table V.1: Measurement time for various cuts in CACENDRA, the centimetric anechoic chamber at IETR.

The sampling follows the *Igloo* sampling strategy with 4873 points over the full sphere (hence 4873×2 data samples because of polarization change). The procedure described at the beginning has been used, with 12 periodical additional measurements at $\theta = 0$ for 72 points in φ to control the thermal drift. The full sphere acquisition took 53,256 s ($\approx$ 14h50), while the hemisphere took 27,025 s ($\approx$ 7h50).

These data allow to estimate the engines parameters and the time required for the field acquisition and the polarization change. We indeed have 7 independent durations for 6 parameters to estimate. They are gathered into the following tables:

Angle	Acceleration (deg/s^2)	Cruising speed (deg/s)
φ	5.2	17.5
θ	1.4	4.3

Table V.2: Estimated engines parameters.

Time considered	Value (s)
Stop at each point t_{stop}	2.5
Polarization change t_{pol}	13

Table V.3: Additional estimated duration.

Conclusion

All quantities needed by our modelling have been determined, they enableto estimate reliably the field acquisition phases for equiangular or *Igloo* sampling techniques in the IETR anechoic chamber CACENDRA.

B   Automatic search algorithm of the BPDN error tolerance parameter

This section gives the algorithm to automatically find the error tolerance parameter of σ when using the sparse recovery problem BPDN. We recall the BPDN problem

$$\min_{\mathbf{x}} \|\mathbf{x}\|_1 \text{ subject to } \|\mathbf{A}\mathbf{x} - \mathbf{y}\|_2 \leq \sigma$$

where σ is the data fitting parameter to be set. This algorithm has been adapted from [1], we note $\mathbf{x}_\sigma$ the solution returned by the BPDN with σ as the data fitting parameter. The curvature computation routine noted C has three parameters P_1, P_2, P_3 which are the points of the underlying curve, the returned number of $C(P_1, P_2, P_3)$ is the curvature estimation at the second point P_2. The parabola method [2] is used to achieve this estimation.

Algorithm 2 Search algorithm of the L-curve corner

Require: $[\sigma_1, \sigma_4]$ the search interval, ε the update tolerance, $\mathbf{A}$ the SW matrix, $\mathbf{y}$ the measurement data vector.

1: **Initialization**
2: $\varphi \leftarrow (1 + \sqrt{5})/2$ (Golden ratio)
3: $x_1 \leftarrow \log_{10}(\sigma_1), x_4 \leftarrow \log_{10}(\sigma_4)$
4: $\sigma_2 \leftarrow 10^{(x_4 + \varphi x_1)/(1+\varphi)}, x_2 \leftarrow \log_{10}(\sigma_2)$
5: $\sigma_3 \leftarrow 10^{x_1 + (x_4 - x_2)}$
6: **for** $i = 1$ to 4 do **do**
7: $\quad$ $P_i = (\|\mathbf{A}\mathbf{x}_{\sigma_i} - \mathbf{y}\|_2, \|\mathbf{x}_{\sigma_i}\|_1)$ Point of the L-curve with σ_i.
8: **while** $\frac{\sigma_4 - \sigma_1}{\sigma_4} > \varepsilon$ **do**
9: $\quad$ $C_2 \leftarrow C(P_1, P_2, P_3)$, Curvature at P_2
10: $\quad$ $C_3 \leftarrow C(P_2, P_3, P_4)$, Curvature at P_3
11: $\quad$ **while** $C_3 < 0$ **do**
12: $\quad\quad$ $\sigma_4 \leftarrow \sigma_3, P_4 \leftarrow P_3$
13: $\quad\quad$ $\sigma_3 \leftarrow \sigma_2, P_3 \leftarrow P_2$
14: $\quad\quad$ $\sigma_2 \leftarrow 10^{(x_4 + \varphi x_1)/(1+\varphi)}$
15: $\quad\quad$ $P_2 = (\|\mathbf{A}\mathbf{x}_{\sigma_2} - \mathbf{y}\|_2, \|\mathbf{x}_{\sigma_2}\|_1)$
16: $\quad\quad$ Computing the curvature C_2 at σ_2, $C_2 \leftarrow C(P_1, P_2, P_3)$
17:
18: $\quad$ **if** $C_2 > C_3$ **then**
19: $\quad\quad$ $\sigma \leftarrow \sigma_2$
20: $\quad\quad$ $\sigma_4 \leftarrow \sigma_3, P_4 \leftarrow P_3$
21: $\quad\quad$ $\sigma_3 \leftarrow \sigma_2, P_3 \leftarrow P_2$
22: $\quad\quad$ $\sigma_2 \leftarrow 10^{(x_4 + \varphi x_1)/(1+\varphi)}$
23: $\quad\quad$ $P_2 = (\|\mathbf{A}\mathbf{x}_{\sigma_2} - \mathbf{y}\|_2, \|\mathbf{x}_{\sigma_2}\|_1)$
24: $\quad$ **else**
25: $\quad\quad$ $\sigma \leftarrow \sigma_3$
26: $\quad\quad$ $\sigma_1 \leftarrow \sigma_2, P_1 \leftarrow P_2$
27: $\quad\quad$ $\sigma_2 \leftarrow \sigma_3, P_2 \leftarrow P_3$
28: $\quad\quad$ $\sigma_3 \leftarrow 10^{x_1 + (x_4 - x_2)}$
29: $\quad\quad$ $P_3 = (\|\mathbf{A}\mathbf{x}_{\sigma_3} - \mathbf{y}\|_2, \|\mathbf{x}_{\sigma_3}\|_1)$
30: **return** σ

C   Computation of the Spherical Waves

A SW expansion code of the radiated field has been developed during the thesis. A naive implementation of the formula in (II.8) and (II.9) leads to three main problems. The factorial terms in the definition of the normalized associated Legendre polynomial in (II.7) induce overflows for high truncation orders N (typically when N goes beyond 80 for the standard complex128 implementation in Python). The term $\frac{1}{\sin\theta}$ has to be considered carefully to avoid a division by 0 at $\theta = 0$ or π. Finally a non-optimized implementation of the SW matrices or transformation coefficients rapidly induces unnecessary large computation times. These considerations led to writing a full code for spherical wave evaluation and transformation.

Normalized associated Legendre polynomials

The associated Legendre Polynomials P_n^m are computed from the following relations

$$P_{n+1}^m(x) = \frac{1}{n-m+1}\left[(2n+1)xP_n^m(x) - (n+m)P_{n-1}^m(x)\right],$$
$$P_{n+1}^{n+1}(x) = -(2n+1)\sqrt{1-x^2}P_n^n(x).$$

Knowing that $P_0^0(x) = 1$ and $P_1^0(x) = x$, one can deduce the value of $P_n^m(x)$ for any $n, m \geq 0$ and $1 \in [0, 1]$. The overflowing problem can be avoided by dividing the former expression by $n + 1$, when computing the values recursively. This results in computing $\frac{1}{m!}P_n^m$ instead, avoiding the overflow problem. The polynomials for which $-n \leq m < 0$ are computed using

$$P_n^{-m}(x) = (-1)^m \frac{(n-m)!}{(n+m)!}P_n^m(x).$$

Now that the associated polynomials are computed, the normalization is performed. Because of $\frac{1}{m!}P_n^m$, the normalization constant is $\sqrt{\frac{2n+1}{2}\frac{(n-m)!}{(n+m)!}}m!$, which can be computed safely recursively since $\sqrt{ab} = \sqrt{a}\sqrt{b}$.

Recurrence relations for SW computation

The expressions involved in the definition of the SW are not directly the normalized associated Legendre polynomials but values derived from them. Fortunately, there expressions can also be computed recursively using our previous code for the evaluation of the Legendre polynomials, they also avoid the problematic factor $\frac{1}{\sin\theta}$. They are for the first terms [3]

$$\frac{m\overline{P}_n^m(\cos\theta)}{\sin\theta} = \begin{cases} 0 & \text{if } m = 0 \\ \frac{1}{2}\cos\theta\left[(n-m+1)(n+m)\overline{P}_n^{m-1}(\cos\theta) + \overline{P}_n^{m+1}(\cos\theta)\right] & \\ \quad + m\sin\theta\overline{P}_n^m(\cos\theta) & \text{if } m > 0 \end{cases}$$

and for the other term

$$\frac{d\overline{P}_n^m(\cos\theta)}{d\theta} = \begin{cases} -\overline{P}_n^1(\cos\theta) & \text{if } m = 0 \\ \frac{1}{2}\left[(n-m+1)(n+m)\overline{P}_n^{m-1}(\cos\theta) - m\sin\theta\overline{P}_n^m(\cos\theta)\right] & \text{if } m > 0 \end{cases}$$

The values for $m < 0$ are simply derived from the relations $\frac{m\overline{P}_n^m(\cos\theta)}{\sin\theta} = -\frac{|m|\overline{P}_n^{|m|}(\cos\theta)}{\sin\theta}$ and $\frac{d\overline{P}_n^m(\cos\theta)}{d\theta} = \frac{d\overline{P}_n^{|m|}(\cos\theta)}{d\theta}$.

Optimization of the SW matrix computation

The implementation of the recurrence relations can be optimized to speed up the computation time but the main point is to go through all the indexes of the SW, s, m, n so to avoid computing the same quantity multiple times. Let us recall that the SW are a product of three independent functions, their computation cost is greatly reduced by appropriately computing each dependency, especially for the equiangular or igloo samplings. Indeed, computing the elevation dependency in θ is costly, but for these types of samplings, there are only a few different θ values with respect to the total number of points. It is also worth pointing out that the SW $\mathbf{F}_{1mn}$ in (II.8) and $\mathbf{F}_{2mn}$ in (II.9) have the same but switched θ dependency between the components in $\hat{\theta}$ and $\hat{\varphi}$ up to a multiplicative factor depending on the distance.

Computation of the SW transformation coefficients

The origin and the orientation of the SW basis can be changed, leading to the transformation formulas for rotation (III.1) and translation (III.2). These transformations can be achieved in practice by a modification of a SW matrix $\mathbf{A}$ by coefficients, namely $D_{\mu m}^n(\chi_0, \theta_0, \varphi_0)$ for the rotation and $C_{\sigma\mu\nu}^{sn(c)}$ for the translation. Computing these coefficients is costly and a naive implementation is not suitable for a practical use of these transformations, leading to numerous coding tricks and tweaks. The interested reader can refer to [4] for computing the translation coefficients and the rotation coefficients have been computed using the Jacobi evaluation routine from the SciPy library [5] since there was no particular problem with it. The translation coefficients have to be handled carefully to avoid overflows for similar reasons as in the Legendre polynomials, the equation involves the ratio of two factorial terms mitigating each others. There are also symmetrical relations available in [3] to avoid unnecessary recursive computations for both coefficient types.

Bibliography

[1] A. Cultrera and L. Callegaro. A simple algorithm to find the l-curve corner in the regularization of inverse problems. *CoRR*, abs/1608.04571, 2016.

[2] H. Kim and J. Rossignac. Parabola-based discrete curvature estimation. In *15th Int. Conf. on Computer Graphics, Visualization and Computer Vision (WSCG)*, Jan. 2006.

[3] J. Hald, J.E. Hansen, F. Jensen, and F.H. Larsen. *Spherical Near Field Antenna Measurements*. Peter Peregrinus, 1988.

[4] J. Bruning and L. Yuen. Multiple scattering of EM waves by spheres part i–multipole expansion and ray-optical solutions. *IEEE Transactions on Antennas and Propagation*, 19(3):378–390, 1971.

[5] Scipy. Technical report, SciPy Developers, 2021. Available at https://www.scipy.org/.

Publication list

Journal publications

1. N. Mézières, B. Fuchs, L. Le Coq, J.M. Lerat, R. Contreres and G. Le Fur. On the Application of Sparse Spherical Harmonic Expansion for Fast Antenna Far Field Measurements. *IEEE Antennas and Wireless Propagation Letters*, 2020.

2. N. Mézières, B. Fuchs, L. Le Coq, J.M. Lerat, R. Contreres and G. Le Fur. Fast Antenna Characterization Improvement by Pattern Rotations. *IEEE Trans. on Antennas and Prop.*, 2020.

3. N. Mézières, B. Fuchs, L. Le Coq, J.M. Lerat, R. Contreres and G. Le Fur. On the Antenna Position to Improve the Radiation Pattern Characterization. *IEEE Trans. on Antennas and Prop.*, 2020.

4. L. Le Coq, N. Mézières, P. Leroy and B. Fuchs. Some Contributions for Antenna 3D Far Field Characterization at Terahertz. *MDPI Sensors*, 2021.

5. N. Mézières, M. Mattes and B. Fuchs. Characterization of antenna far-field pattern from a minimum number of samples. Submitted to *IEEE Trans. on Antennas and Prop.*, 2021.

Conference papers

1. N. Mézières, B. Fuchs, L. Le Coq, J.M. Lerat, R. Contreres and G. Le Fur. Caractérisation Rapide d'Antennes par Utilisation des Harmoniques Sphériques Vectorielles. *JNM Caen*, 2019.

2. N. Mézières, B. Fuchs, L. Le Coq, J.M. Lerat, R. Contreres and G. Le Fur. Application and Improvement of Fast Antenna Testing via Sparse Spherical Harmonic. *AMTA*, 2020.

3. N. Mézières, B. Fuchs, L. Le Coq, J.M. Lerat, R. Contreres and G. Le Fur. On the Antenna Positioning for a Faster and Better Radiation Pattern Characterization. *EUCAP*, 2021.

4. N. Mézières, M. Mattes and B. Fuchs. Reduced-Order Model for Antenna Pattern Characterization from a Minimum Number of Samples. Submitted to *AMTA*, 2021.

Titre : Contributions à la Caractérisation Rapide et Précise d'Antennes

Mots clés : Électromagnétisme, métrologie, antennes, reconstruction parcimonieuse, éléments finis.

Résumé : Cette thèse traite de la caractérisation du diagramme de rayonnement des antennes afin d'améliorer l'utilisation des systèmes de mesure existants.

Deux approches sont proposées en vue d'accélérer la mesure du diagramme de rayonnement des antennes en diminuant le nombre d'échantillons requis.

La première exploite la décomposition parcimonieuse du champ rayonné par les antennes dans la base des ondes sphériques et nécessite seulement la connaissance de la dimension électrique maximale de l'antenne.

La seconde approche utilise les dimensions externes de l'antenne et la surface de mesure afin de construire numériquement une base adaptée au problème de mesure d'antenne.

Pour ces deux techniques, le nombre minimal d'échantillons du champ requis et une estimation du gain en temps de mesure à l'IETR sont donnés, montrant ainsi leur intérêt.

En complément, une stratégie permettant d'optimiser le positionnement de l'antenne en post-traitement au sein de la base de mesure a été proposée afin d'améliorer la qualité du diagramme de rayonnement reconstruit.

Toutes les procédures de mesure et traitements associés ont été validés sur des données numériques et expérimentales provenant d'antennes de types variés, opérant dans diverses bandes de fréquence et mesurées dans plusieurs chambres anéchoïdes, démontrant ainsi leur caractère général.

Title: Contributions to Fast and Accurate Antenna Characterization

Keywords: Electromagnetism, metrology, antennas, sparse recovery, finite elements.

Abstract: This thesis deals with the characterization of antenna radiation patterns to improve the use of existing measurement systems.

Two approaches are proposed in order to speed up the measurement of these radiation patterns, which is achieved by reducing the required number of field samples.

The first one exploits the sparse spherical wave expansion of the field radiated by antennas. It only requires to know the maximum electrical dimension of the antenna.

The second approach exploits the antenna external geometry and the measurement surface shape in order to build numerically an expansion basis tailored to the characterization problem.

For both techniques, the minimal number of required field samples and an estimation of the field acquisition time at the IETR facilities are given, showing their potentialities to speed up the antenna measurements.

Besides, an optimization strategy of the antenna positioning in post-processing is proposed. This procedure improves the quality of the reconstructed antenna radiation pattern from a given measurement.

All the proposed methods have been validated using numerical and experimental datasets from various antenna types, different operating frequency bands and measured in several facilities, demonstrating thereby their versatility and generality.